Finite Volume Approximations for Hyperbolic Conservation Laws Arising in Biological Sciences

A Thesis

submitted in partial fulfillment of the requirements for the award of the degree of

Doctor of Philosophy

in

School of Mathematics

by

Santosh Kumar
(Reg. No. 901311010)

under the guidance of

Dr. Paramjeet Singh

Thapar Institute of Engineering & Technology
Patiala-147004, Punjab, India
July 20, 2018

Candidate Declaration

I hereby declare that this Ph.D. thesis, entitled **"Finite Volume Approximations for Hyperbolic Conservation Laws Arising in Biological Sciences"** in partial fulfillment of the requirement for the award of degree of Doctor of Philosophy submitted in the School of Mathematics of Thapar Institute of Engineering and Techonology, Patiala, is an authentic record of my own research work carried out under the guidance and supervision of Dr. Paramjeet Singh. The websites, books, and articles which I have made use of are acknowledged at the respective place in the text.

The matter presented in this thesis has not been submitted elsewhere for the award of any other degree or diploma from any institution.

Date: _____

Santosh Kumar
Candidate

This is to certify that the above statement made by the candidate is correct to the best of our knowledge.

Date: _____

Dr. Paramjeet Singh
Supervisor

The Ph.D. Viva-Voice examination of **Santosh Kumar**, Research Scholar has been held on _____ .

_____	_____	_____
(Supervisor)	**(External Examiner)**	**(Chairperson of Doctoral Committee)**

To my parents, wife, nieces, nephew and son Adwick who are the pride and joy of life

Abstract

Mathematical models based on partial differential equations have become the main components of quantitative analysis in many areas of biological science, engineering, finance, image processing and many other fields. Hyperbolic conservation laws is an important field of partial differential equations. They play a prominent role in modelling flow and transport process. These equations are of importance to a broad spectrum of discipline such as neuroscience, fluid mechanics, gas dynamics, population dynamics, elasticity chromatography, traffic flow, geophysics, meteorology, electromagnetism, astrophysics, etc.
In this dissertation, we have studied partial differential models for biological science and designed the appropriate numerical schemes to find approximate solutions.

Chapter 1 begins with introduction, motivation and literature review for the research work. A brief overview to the basic theory of hyperbolic conservation law and short introduction of numerical techniques and related results are presented. In addition, the structure of the thesis has been presented at the end of this chapter.
Chapter 2 starts with a brief background of nervous system and related theory. Further, it presents the proposed numerical scheme based on finite volume method, which is used to find the numerical solution of the governing model equation. This chapter also provides the stability of the proposed framework. To evaluate the performance of proposed approach, test examples have been considered.
Chapter 3 presents a population density model based on quadratic-integrate-and-fire neuron. The chapter starts with the overview of quadratic integrate-and-fire neuron model for deriving the governing equation with the help of population density approach. Thereafter, a high-order numerical scheme has been designed to find the approximate solution of model equation. Finally, numerical experiments are taken to demonstrate both the effectiveness and the efficiency of our proposed method. This chapter concludes with performance evaluation of the proposed work.
In Chapter 4, an excitatory and inhibitory population density model based on leaky-integrate-and-fire neuron with potential jumps has been presented. The synaptic connection between neurons is modeled by a potential jump at the receiving of input current. This chapter also presents a high-order numerical

scheme to find the approximate solution of the governing equation. Further, it includes the diffusion approximation, is used to avoid the non-local terms. The efficiency and accuracy of the proposed scheme is tested through numerical experiments.

The Chapter 5 deals with a size-structured neuron model based on the articles [1, 2]. This model consists of a transport equation with age-dependance and spatial structure. Moreover, the governing equation is the renewal equation for demography. The chapter also presents a finite volume approximation for the simulation of transport equation. Theoretical analysis of the proposed framework is also discussed in this study.

In Chapter 6, the nonlinear age-structured population model has been studied. The model consists a real biological situation in which all human beings have a finite maximum age. The model comprises the fertility and mortality factors, which depend on the age, seasonality and external resources in which intrinsic mortality is unbounded. This chapter presents a high-order accurate numerical scheme to approximate the solution of the model equation. To validate the proposed framework, some numerical experiments have been employed in this chapter.

Chapter 7 concludes the dissertation and also shed light on some future direction of the present work.

Keywords: Partial differential equation, Hyperbolic conservation law, Finite volume method, WENO scheme, IMEX strong stability preserving scheme, MUSCL scheme, Leaky integrate-and-fire neuron, Quadratic integrate-and-fire neuron, Population density approach, Age-structured models, Population dynamics.

Acknowledgements

It has been a most wonderful and overwhelming experience to completing this doctoral work. I am grateful for advice, support, encouragement, and friendship of many individuals and of a few organizations who contributed to this dissertation. First and above all, I praise Goddess (Maa Chaturbhuja), the almighty for providing me this opportunity and granting me the capability to proceed successfully.

I have been very privileged to have undoubtedly the most intuitive, smart and supportive advisor anyone could ask for, namely Paramjeet Singh. Ever since I learned from him what an avoided crossing was, I have been stimulated and excited by his constant flow of good ideas. All the discussions and freedom has really shaped my carrier. He has also known when (and how) to give me a little push in the forward direction when I needed it. His constructive criticism and valuable suggestions at every step of my work has not only shaped the present version but also broadened my perspective during the entire course of my study.

I gratefully acknowledge the funding agency, the University Grants Commission of India, for providing financial support to complete my thesis work.

I express my heartiest thanks to Professor G. D. Veerappa Gowda from TIFR Centre for Applicable Mathematics at Bengaluru for his invaluable suggestions. I am thankful to my wonderful teachers like Professor Arvind Kumar Lal (Head, School of Mathematics) for his constant support and encouragement. I am also thankful to all the concerned people in the School for providing the necessary facilities and help during my research work. A very special thank to goes to Dr. Kapil Kumar Sharma, Dr. Amit Kumar, Dr. Raj Nandkeolyar, and Dr. Ram Jiwari for sharing their invaluable knowledge with me and always welcoming my endless ramblings. I would like to express my gratitude to Professor O. P. Pandey (Dean, and Research and Sponsored Projects) his invaluable support.

I would like to thank my friends Harjeet Singh, Varun Joshi, Sharad Tiwari, Sandeep Singh, Gourav Gupta, Sukhvir Singh, for enjoyable tea breaks. I would like to thank Ashok Khunger for his mental support, many personal discussions and shared own experience about the life with me. I would like to express my special thanks of gratitude to my teacher-cum true friend Mr. Baljit Singh (S.G.G.S College, Chandigarh) who always were ready to help me throughout my ups and downs.

A penultimate thanks goes to my wonderful parents. For always being there when I needed them most, and never once complaining about how infrequently I visit, they de-

serve far more credit than I can ever give them. For my parents who raised me with a love of science and supported me in all my pursuits. Thank you. I would like to thank my brother, sister, brother in-law, sister-in-law, nieces (Bhavika and Shivanshi) and nephew (Riyansh) for all their love, support and encouragement.
A special thanks goes to my beloved wife Nisha Kumari and my son Adwick. Her love and unconditional support through my ups and downs remains unrecompensable. You were always around at times I thought that it is impossible to continue, you helped me to keep things in perspective. I greatly value her contribution and deeply appreciate her belief in me. Also I express to thank parents-in-laws for their support and valuable prayers.

Lastly but not the least, I am thankful to all those surrounding me on the beautiful campus of my University at Patiala who treated me with love and respect which I will always remember.

Santosh Kumar

Table of Contests

List of Figures

List of Tables

List of Abbreviations

FDM	Finite Difference Method
FVM	Finite Volume Method
FEM	Finite Element Method
MUSCL	Monotonic Upwind Scheme for Conservation Laws
RK	Runge-Kutta
SSP	Strong Stability Preserving
WENO	Weighted Essentially Non-Oscillatory
PETSc	Portable Extensible Toolkit for Scientific Computation
MOOSE	Multiphysics Object-Oriented Simulation Environment
TVD	Total Variation Diminishing

Chapter 1

Introduction and Related Work

A Mathematical model is the mathematical representation of the real-world system. Mathematical modelling is the technique of constructing a mathematical model of a problem, then using it to analyze and find a solution of the problem. Also, it is an interdisciplinary area in which expertise from different fields share their knowledge to improve existing results, develop better ones or to estimate the behavior of certain phenomena. Moreover, mathematical models based on ordinary differential equations (ODEs) and partial differential equations (PDEs) are ubiquitous these days, since they are arising in many areas such as biology, ecology, evolution, engineering, finance, medicine, physics and other fields. The applications of aforementioned fields are such as neuronal dynamics, age-structured, tumor growth, general relativity, option pricing, fluid mechanics and many more. The complexity of these models means that it is impossible to find the exact solutions of governed PDE equations, even in very simple cases. Hence, the numerical methods play a vital role in finding the approximate solution of such type of PDEs.
Overview of numerical solution. The history of numerical solution of partial differential equation is much more recent than the analytic methods. The numerical solution of differential equations has been a subject of intense activity for the last 60 years or so, primarily due to advances in computer technology and the introduction of numerical computing applications like Fortran, Mathematica, Maple, Matlab, Pyhton, PETSc (Portable Extensible Toolkit for Scientific Computation) and MOOSE (Multiphysics Object-Oriented Simulation Environment), which in turn has led to improvements in numerical methods that are being used. As a result many unsolved problems related to ODEs and PDEs are solved by appropriate numerical methods such as finite difference method (FDM), finite element method (FEM), finite volume method (FVM), spectral method, boundary element, meshless or mesh free methods.

1 Research Motivation

Computational and Mathematical modeling is a very popular approach for inves-

tigating the functionality of the biological system. Recent developments in numerical techniques and computing technology have expanded its scope in the research activity. The motivation behind this dissertation is to understand the behavior of living system and in particular, nervous system and the population dynamics, which underlies mathematical analysis and study of the computer simulation. This job can be served by computational biology The application of computational modeling to living system is significant because, in comparison with other physical systems, where such type of modeling is used, biological systems can be seen explicitly as processors of information. In this manner, computational models for these living system are not just devices for count or forecast but usually explain the functionality of the living system. In particular computational neuroscience, the researchers are generally interested in determining what the various parts of the nervous system do, and how they do it.

Computational neuroscience is the scientific study of the neural system. It is a part of computational biology. Computational models, and in particular quantitative models have become an important tool for research in neuroscience for many decades. In fact, one of the main celebrated achievement in this field is credited to the Hodgkin-Huxley model that describes the generation of action potentials which is based on quantitative approach [5]. In addition, much of what is understood about the functionality of the nervous systems has been informed by mathematical and computational modeling.

Overview of the concept of neuroscience. The brain is like a computer that controls the body's functions as well as the nervous system. It is made of large number of different cells that relays messages to parts of the body. Among these cells, the nerve cells or neurons are the basic processing units, known as electrically excitable cells. In human brain, it has approximately 10^{11} neurons, according to Kandel et al. [6], which is interconnected in a complex manner. More precisely, each neuron is connected to tens of thousands of other neurons, this means there are as many connections in a single cubic centimeter of brain tissue as there are stars in the Milky Way Galaxy.
In the late 19th century Spanish histologist Santiago Ramón y Cajal identified that "the neuron's place as the primary functional unit of the nervous system". He suggested that all neurons are discrete cells, which communicate via circuits and junctions. Moreover, he was the first who gave the detailed information about the structure of the nerve cells, and revealed that all neurons share the same basic structure (see in [7, 8]).
Neuron structure. A typically neuron has four major structural regions: dendrites, cell body (soma), axon, and presynaptic terminals (axon terminals). Each of these regions has a different role (see Fig. 1.1). The cell body also known as soma, is the main component of the neuron that consists of the nucleus with in. It is connected to other cells by

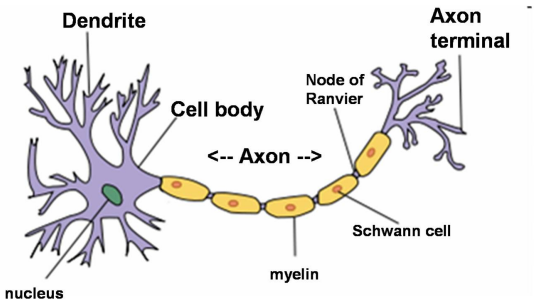

Figure 1.1: Structure of a typical neuron (this image is taken from Wikipedia, [3].)

dendrites which brings information to other neurons. The information communicated by one neuron to the other neurons is transmitted by a long thin structure called the axon. The portion of the axon where it originates from the cell body is known as axon hillock, which is the part of the neuron and it has the greatest density of voltage-dependent sodium channels. Near its ends, axon further divides into branches for communication to other neurons. This structure is known as axon terminal or presynaptic cell which contains the synapses (synapses refer to the interactions or junctions usually found among neurons). There are two different type of synapses: electrical synapses and chemical synapses. The difference is based on how the signal is transmitted from one cell to the next cell. In the electrical synapses, the signal is transmitted through gap junctions (see Fig. 1.2a) from one neuron to other without need of any receptors of the postsynaptic cell. As a result signaling at electrical synapses is more rapid than that which occurs across chemical synapses. On other side, in chemical synapses, the signal is transmitted between two neurons through neurotransmitter (see Fig 1.2b), by the receptors of the postsynaptic cell. When the receptors receive neurotransmitter molecules, the ion channels begin to open. As a consequences, the flow of ions come in or out and changing the local transmembrane potential of the cell. The resulting change in voltage is called a postsynaptic potential. The result of this process can be excitatory in case of depolarizing currents or inhibitory in case of hyperpolarizing currents. The excitatory or inhibitory nature of a synapse depends on the types of ion channel conduct the postsynaptic current displays, which in turn is a function of both the type of receptors and the type of neurotransmitter employed at the synapse. If a signal is transmitted at an excitatory synapse, then the depolarization of the cell can be strong enough so that an action potential can be initiated in the postsynaptic cell. If the depolarization induced by the excitatory postsynaptic potential is not sufficient for an action potential initiation, then the effect of the depolarization will last for some time, and will be progressively attenuated. Therefore, if the neuron receives signals from the same or other neurons, the postsynaptic potentials they provoke will be added. This phenomenon is known as the synaptic integration.

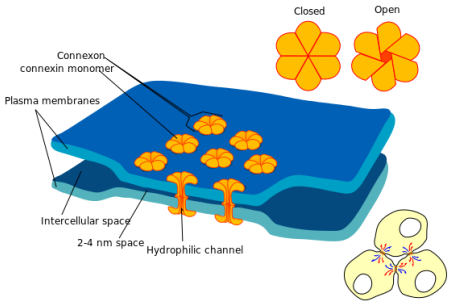

(a) Depiction of a electrical synapse

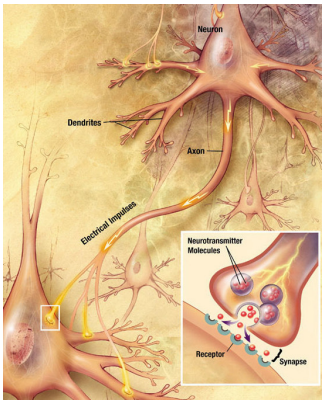

(b) Depiction of a chemical synapse

Figure 1.2: Structure of a synapse, (both images taken from Wikipedia, [3].)

Finally, we can think of neuron as a miniature self-contained information processor. It receives inputs, processes information, and generates outputs. The dendrites is associated with the receiving of inputs, the cell body is associated with the information processing and the process most associated with the output is the axon terminals (see Fig. 1.3). The more details about modeling of neurons and neural networks see herein [9–13].

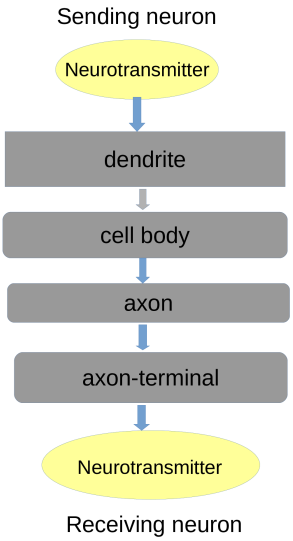

Figure 1.3: Neuron signal direction

2 Literature Review

Integrate-and-fire (IF) neuron is the main component for the description of the neural system. It describes the neuron's membrane potential in terms of the injected current and the synaptic inputs that it receives. More precisely, the membrane potential receives inputs either excitatory or inhibitory from different neurons. These inputs connected with weighted synaptic strength are modeled either as injected current, is known as current synapse models, or as a change in the membrane conductance, is named as, conductance synapse models. These models (Conductance synapse models) depend on the difference between the membrane potential and the reversal potential, and it describe the amplitude of the excitatory and inhibitory inputs. Moreover, IF neuron model is known as a point neuron model in which the dendrites spatial structure of the neuron is neglected.

Leaky integrate-and-fire neuron. The neuron is in fact leaky, since the contribution of all synaptic inputs to the membrane potential of a neuron decay with a membrane time constant. If the membrane potential decay over time is neglected, the model is said to be a perfect integrator. Moreover, when the membrane potential of a neuron arrives a certain fixed stage (threshold level), a spike or action potential is generated, it indicates the *first passage time* of the membrane potential across the threshold. Thereafter, the membrane potential comes back to the resting state and is deactivated for a short time.

History of integrate-and-fire neuron. The integrate-and-fire neuron has a long history. In 1907, Lapicque [14] introduced a neuron model that describes subthreshold electrical features of a single neuron, through its membrane potential, i.e., the membrane potential of the neuron in terms of an electric circuit consisting of a parallel capacitor and resistor that represents the capacitance and leakage resistance of the neuron membrane, respectively (Fig. 1.4). The membrane potential is charged until it arrives a certain level

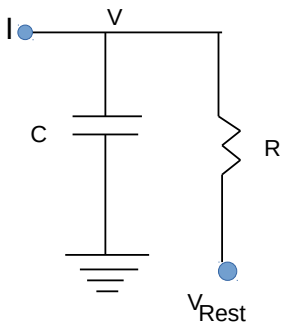

Figure 1.4: The equivalent circuit represents the membrane potential of a neuron in subthreshold level, where V is the membrane potential, C is the membrane capacitance, R represents the membrane resistance, V_{rest} is the resting membrane potential, and I is an injected current.

where the spike appears, and then potential come back into the resting state (Fig. 1.5). The dynamics of the membrane potential is given by

$$C\frac{dV(t)}{dt} = -V + V_{rest},$$

where $V(t)$ is the membrane potential of a neuron at time t, C is the membrane capacitance and V_{rest} is the resting potential. With aid of this model, Lapicque could easily evaluate the spiking (firing) rate of a neuron (Fig. 1.6). This model is further used for many other neuron modeling for many decades.

In 1936, Hill [15], analyzed the Lapicque's model with external injected current in the

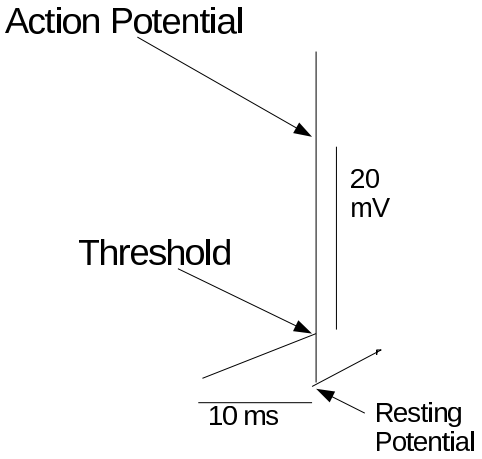

Figure 1.5: The dynamics of the membrane potential of a neuron.

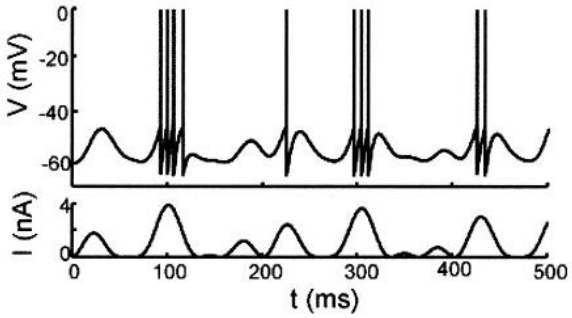

Figure 1.6: An integrate-and-fire model neuron driven by a time varying current. The upper trace is the membrane potential and the bottom trace is the input current. This image taken from [4].

neuron

$$C\frac{dV(t)}{dt} = -V + V_{rest} + I_e(t).$$

Here, I_e denotes an external current directly injected in the neuron. The approach (IF

model) is useful for the separation of time scales between the relatively slow subthreshold integration and extremely rapid spike generation, which is one of the key insights into neuronal behavior. Focusing upon the subthreshold mechanism, it has been proven that the properties of subthreshold membrane be a powerful tool for the study of information processing capabilities of neurons. In 1964, Gerstein and Mandelbrot [16] proposed the stochastic integrate-and-fire neuron model which was formulated as a random walk problem with threshold barrier. The model was further modified by Stein (1965 [17], 1967 [18]) to include the decay of the membrane potential. Subsequently, developments in this model is to use stochastic differential equations with different numerical techniques (Knight 1972 [19], Kryukov 1976 [20], Tuckwell 1977 [21], Wilbur et al. 1982 [22] and Lánskỳ 1984 [23]). Moreover, the aforementioned approaches have also been used to investigate the effect of inhibition and reversal potential in the Stein's model (Tuckwell 1978 [24], Cope et al. 1979 [25], Tuckwell et al. [26], Tuckwell 1979 [27], Wilbur et al. 1983 [28], Hanson et al. 1983 [29], Musila et al. 1994 [30]).

IF model equation. The general form of the membrane potential in IF model is

$$C\frac{dV(t)}{dt} = I_l(V) + I_{syn}(V,t) + I_e(t),$$

where I_l is a leak current and I_{syn} is the synaptic current. There are many variants of this model (IF) in which few of them have been considered in the literature. For instance, the IF model has a leak current: $I_l(V) = -g\ (V - V_{rest})$, where g denotes the leak conductance. Dividing the above equation on both sides by g, and rewrite it as

$$\tau\frac{dV(t)}{dt} = f(V) + I_{syn}(V,t) + I_e(t),$$

where $\tau = \dfrac{C}{g}$, $f(V) = -(V - V_{rest})$ and g has been absorbed in the currents I_{syn} and I_e. The above form of the IF model is known as a leaky integrate-and-fire-neuron model.

Spike-response model. A variation in IF model can be also seen in the form of *spike-response models* (Gerstner 1995 [31], Gerstner 2001 [32], Gerstner et al. 2002 [9]). Basically, spike-response model is the generalization of leaky integrate-and-fire neuron model (LIF) and it describes the generation of action potential in neurons. The motivation behind spike-response model is to overcome the difficulty of finding the exact solution of integrate-and-fire neuron models when the synaptic input is inhomogeneous Poisson stochastic type. The key difference to the classical integrate-and-fire neuron model is that after the spike generation the resting membrane potential is achieved by adding the additional term $\eta(t - \hat{t})$ to the membrane potential, where $\hat{t}$ is the firing time of the last spike of the neuron and η represent the form of action potential. A notational contrast

is that the IF model needs differential equations for the voltage while the spike response model is formulated by integral equation

$$V(t) = \eta(t - \hat{t}) + \int_0^\infty \kappa(t - \hat{t}, s) I(t - s) ds,$$

where κ represent the linear response to an incoming current and $I(t)$ a stimulating current. The next spike generates if the membrane potential of a neuron arrives at a fixed threshold level from below where the time $\hat{t}$ is updated.

Fusi and Mattia in 1999, [33], introduced the linear integrate-and-fire neuron model for the study of the collective behaviors of the neural networks in which the depolarization of the subthreshold membrane potential is constant that is

$$\frac{dV(t)}{dt} = -\beta + I(t),$$

where $\beta > 0$ is a constant decay. In 1986, Ermentrout and Kopell [34], proposed a *quadratic-integrate-and-fire (QIF) neuron model* to examine of the neuron firing. This model describes the neuron canonical form in which neuron firing is determined by Type I bifurcation (Izhikevich 1999 [35]) and it is similar to the *theta neuron model* (Ermentrout 1996 [36], Gutkin et al. 1998 [37], Latham et al. 2000 [38]). A number of authors have used QIF model for the description of the intrinsic properties of neural system (Brunel et al. 2003 [39], Lindner et al. 2003 [40]). Further, Fourcaud-Trocmé et al. introduced the *exponential integrate-and-fire neuron model* in 2005 for the description of the dynamics of the instantaneous firing rate, see herein [41, 42] for details. Later, Brette et al. [43] have used this model for the description of neural activity.

Neuronal Noise. Nowadays, integrate-and-fire models with noise, for a single neuron or network of neurons have become the fascinating field of research. Noise word was introduced in neuroscience many decades ago (Schmitt 1967 [44], DeFelice 1981 [45], Holden 1976 [46]). Neuronal noise means the random fluctuation or variability that occurs in the environment of a single neuron as well as in the firing activity of the neural network. Neurons never respond in the same way under the repeated presentation of a specific input signal. The response variability and its outcomes for neural network function has been under observation for many years. The same scenario occurs in the spontaneous activity, which show different kind of randomness. There are mainly two distinct sources of noise: external and internal. The external source of noise generally refers to the random fluctuation while the internal source indicates the probabilistic nature of the chemicals reactions, which provide the firing activity of neurons [43, 47–50]. In a more specific manner, noise is present everywhere in the nervous system because a

single neuron is receiving a huge amount of synaptic inputs from other neurons, and also due to the randomness occurring in the opening and closing gates of the ion channels [51, 52].

The noisy leaky-integrate-and-fire model (NLIF) is a mathematical model that describes the stochastic properties of neurons [48, 53–63]. The model equation is governed by a Langevin equation and a discontinuous reset mechanism which mimic the generation of the action potential. With the help of Langevin equation one can write the corresponding Fokker-Planck equation, which provides the time evolution of probability density to find the membrane potential of a neuron in a certain voltage value. Moreover, the NLIF model is a simpler version of the Hodgkin-Huxley model [5], which is sufficiently detailed to allow a qualitative comparison with physical data [10]. In spite of its apparent simplicity many questions still remain open regarding its dynamics. There are many authors [60, 62, 64–67], those have contributed in this field.
The concept of probability density function in computational neuroscience has a long history [28, 47, 68] because it has been used in many contexts of neuronal modelling. However, this approach is not appropriate for the simulation of large neural network [57, 62, 69]. In 1996, Knight [70] innovated a population density approach which tackles the simulation of neural network in more effective manner. Later, this approach is reformed in [71–73]. Several other authors have used this approach for analyzing the firing activity of the neural network [48, 56–63]. Nowdays, there are a number of authors [74–77] who have been used this approach for the derivation of model equations based on PDEs.

2.1 Population Dynamics

Population dynamics is the branch of mathematical biology that deals with size, age-structured of a population and other biological factors which affect them. Moreover, it has a long history more than 200 years or more. Fibonacci used his well-known sequence for the growth rate of a rabbit population model. Later, Malthus gave a mathematical model in which he assumed that the populations of human have a constant natural growth rate. His model was further improved by other researchers taking into consideration the various features of populations.
Mathematical population models include age structure, or other structuring of individuals with continuously varying properties, have a long history. The age structured model plays a key role in population dynamics. Lotka et al. and McKendrick [78, 79] set up a foundation for partial differential equations approach to modelling of age structure

in an evolving populations. The stabilization of age-structure with linear fertility and mortality in models at the earlier stages is identified but not accepted [80, 81]. The analysis of these linear models was established later in [82, 83]. In 1974, Gurtin and MacCamy [84] gave a new technology, based on a nonlinear Volterra integral equations approach, which was used to established the existence, uniqueness and convergence of equilibrium solution to Sharpe-Lotka-McKendrick model. A fast growth of research in non-linear models ensued in biological applications as well as theoretical developments. Further, Iannelli [85] introduced a comprehensive treatment of this approach. The increasingly complex mathematical issues included in nonlinearities in age structured models directed to the improvement of new technology. There are many other approaches available in the literature [86–94] that can be used efficiently to solve non-linear age -structured models. Moreover, there are many approaches available in the literature that were used to tackle the nonlinearity in age-structured model equations [90, 91, 93, 95–98].

3 Research Gaps and Objectives

This section is devoted to the research gaps and the objectives for this research.

Research Gaps

- The synaptic input current is absent in the Stein's model [17]. Once the voltage V surpasses the threshold level r, it remains at the value $r + dr$ for all subsequent times. Both the cases need to be studied in the Stein's model.
- Finite volume method is not used for the dynamics of a structured neuron population [99].
- The absence of numerical study for the excitatory and inhibitory neuron population density model based on quadratic-integrate-and-fire neuron.
- The application of population density approach for an excitatory and inhibitory population neuron model with jumps.
- The absence of high-order numerical scheme need to be studied for noise quadratic-integrate-and-fire neuron model.
- The application of population dynamics: an age-structured population model with non-linear mortality rate and fertility rate need to be investigated.

Objectives

- Development of convergent and stable finite volume approximation based on Godunov method for a realistic model problem arising in neuronal variability.
- Construction of a stable and convergent discrete finite volume approximation of higher-order to investigate the behavior of biological neuron model.
- Development and analysis of finite volume approximation for the hyperbolic conservation laws arising in population dynamics.
- Construction of mesh free finite volume approximation so that there should not be any restriction on the size of the delay.

The remaining sections present an overview of some important mathematical concepts that are related to this study.

4 Numerical Methods

Numerical analysis is the branch of mathematics and also computer science that deals with the study of algorithms for approximate solution of the problems of continuous mathematics. Due to the rapid advancements in computer technology, the uses of numerical techniques for solving the realistic mathematical model problems whose analytical solution cannot be found, have been increased. There are a number of numerical methods such as finite difference method, finite element method, finite volume method, spectral method, boundary element method and many more, which provide the best approximate results for an appropriate system of differential equations.

The finite difference method is the easiest method to apply and to solve a differential equation. The basic idea of finite difference method is to replace the derivative appearing in differential equation by an approximate difference formula. The difference formula is derived from Taylor series expansion. Due to the relative ease of implementation and flexibility, the difference method is the first choice method for the numerical solution of the differential equation. However, this method has some disadvantages: the method becomes intricate when solving the differential equation on an irregular domain, the PDEs is non- linear or based on variable coefficient, it is not easy to prove the stability, consistency, and convergence for the difference method. However, this method serves as a basis for other numerical methods (see [100–102]).

The spectral method is another numerical technique to solve the differential equation. This method is only useful when the solution is smooth and the domain is simple. This

method has some drawbacks: it is very complicated to implement, it cannot represent the physical processes in spectral space. Moreover this method is very expansive at high resolution. The interested readers can find more details about this method herein [103–108].

The finite element method. The basic idea of finite element method is the piecewise representation of the solution in terms of specified basis functions, meshing the modeled domain into smaller elements and solution in each element is constructed from the basis functions. This method is very complicated to implement as compared to other numerical methods. Moreover, this method is not suitable for biological problems because it produces less physical significance solution. The detailed study of this method can be found in [109–111].

The boundary element method. Another numerical technique is the boundary element method, which is used to solve those PDEs that can be converted into integral equations. This method attempts to use the given boundary conditions to fit boundary values into the integral equation, rather than values throughout the space defined by the PDE. The interested readers can be see herein [112, 113].

The finite volume method. The finite volume method is another numerical technique to find the solution of parabolic, elliptic and mainly first order hyperbolic PDEs, for example, conservation laws. The basic idea of FVM is to integrate the differential equation over each fixed size control volume or grid cell, then convert the volume integral of divergence terms into the surface integrals that can be evaluated as fluxes at the surface of each fixed volume. This method can also be used on structured or unstructured geometries. Moreover, this method preserves the local conservativity of the numerical fluxes that means the numerical flux is conserved from one cell to its neighbour cell. Before the discussion of this (FVM) method in detail, we first review the concept of hyperbolic conservation law.

4.1 Hyperbolic Conservation Laws

The prototype for first-order hyperbolic partial differential equation is

$$u_t + f(u)_x = 0, (t, x) \in (0, \infty) \times \mathbb{R}, \tag{1.1}$$

where $u(t, x) : \mathbb{R}^+ \times \mathbb{R} \to \mathbb{R}$ is a unknown density of conserved quantity and $f : \mathbb{R} \to \mathbb{R}$ is the flux function. The variable x denotes the space and variable t denotes the time. The above form of hyperbolic PDE is known as *conservation laws*.

Definition 4.1. Suppose the flux function $f : \mathbb{R} \to \mathbb{R}$ be class $C^1(\mathbb{R})$. Then $u = u(t, x)$ is a smooth solution of Eq. (1.1) if it belongs to class C^1 and satisfies Eq. (1.1) pointwise.
Physical Meaning: To understand the physical meaning of Eq. (1.1), we assume that u is a smooth solution of Eq. (1.1), integrate the above equation with respect to x on the closed interval $[a, b]$, ones obtain:

$$\frac{d}{dt}\left(\int_a^b u(t,x)dx\right) = -\int_a^b f_x(u(t,x))dx = f(t,a) - f(t,b).$$

Consequently, we can say that the total amount of u contained inside any interval $[a, b]$, i.e., $\int_a^b u(t,x)dx$, can change only due to the flow, $f(u(t,x))$, of u across the boundary points at $x = a$ and b. In other words, u is neither created nor destroyed. Thus, we can say that u is the conserved quantity on the given interval.
Remark 4.1. If the flux function $f \in C^1$ and u is a smooth solution of Eq. (1.1), then we can apply the chain rule to obtain

$$u_t + f'(u)u_x = 0 \text{ or } u_t + a(u)u_x = 0, \text{ where } a(u) = f'(u). \tag{1.2}$$

Remark 4.2. If u is a smooth solution, then Eqs. (1.1) and (1.2) are equivalent. However, if u has a jump discontinuity then Eq. (1.2) is not well defined because a product of a Dirac measure, u_x, with a discontinuous function, $a(u)$ is involved. Hence, we can say that Eq. (1.2) is meaningful only for class of continuous functions.
Definition 4.2. The Cauchy problem or an initial value problem (IVP) is a first order partial differential equation of the type

$$\begin{cases} u_t + f(u)_x = 0, \ x \in \mathbb{R}, \ t > 0 \\ u(x,0) = u_0(x), \ x \in \mathbb{R}, \end{cases} \tag{1.3}$$

where $u_0(x)$ is the initial condition and $u = u(t, x)$.
Definition 4.3. If $u_0(x)$ and $f(u)$ both are class C^1 functions, then $u(t, x)$ is a global smooth solution of Eq. (1.3), provided it belongs to class C^1 and satisfy Eq. (1.3) pointwise.
Next we present a technique for the solution of the Cauchy problem in space of smooth functions.
Method of Characteristic: The characteristic curve $x(t, x_0)$ associated to the solution $u(t, x)$ of the Cauchy problem (1.3), starting from the point $(0, x_0) = x_0 \in \mathbb{R}$, is the

solution of the following differential equation

$$\frac{dx(t,x_0)}{dt} = a(u(t,x(t,x_0))) = f'(u(t,x(t,x_0))), \quad x(0,x_0) = x_0. \tag{1.4}$$

Solution: $x(t,x_0) = t.f'(u_0(x_0)) + x_0.$ (1.5)

Proposition 4.1. If $u(t,x)$ is a smooth solution of Eq. (1.3) then it is a constant along the characteristics curve $x(t,x_0)$.

Proof. Let $x(t,x_0)$ be a characteristic curve that begins from the point $x_0 \in \mathbb{R}$, and exists at least on a small interval $[0,t_0)$. For any $t \in [0,t_0)$,

$$\begin{aligned} \frac{du(t,x(t,x_0))}{dt} &= u_t(t,x(t)) + u_x(t,x(t)).x'(t) \\ &= u_t(t,x(t)) + u_x(t,x(t).a(u(t,x(t))) = 0. \end{aligned}$$

Thus, u is constant along the characteristic curve $x(t,x_0)$, and taking the value $u_0(x_0)$. Hence, we obtain the solution of (1.5) as $u(t,x_0) = u_0(x_0)$. This is called the method of characteristics.

Method of characteristics gives a way, to build the smooth solution of Eq. (1.3), provided we must extract $x_0 = x_0(t,x)$, from relation (1.5).

We can extract $x_0 = x_0(t,x)$, by using the inverse function theorem (which provides sufficient conditions for a function to be invertible in a neighborhood of a point of the domain and also provides a formula to calculate the derivative of the inverse function) which states that if a function belongs to C^1 class with non zero derivative at a point, then the function is invertible in the neighborhood of a point. With the help of this theorem we can find a smooth function $x_0(x,t) = x - t.f'(u_0(x_0(t,x)))$ such that

$$u(t,x) = u(t, tf'(u_0(x_0)) + x_0) = u_0(x - tf'(u_0(x_0))).$$

Therefore, $u(t,x) = u_0(x_0(t,x))$, is the smooth solution of Eq. (1.3).

$\mathbf{x(t;x_0)} = \mathbf{t.a(u_0(x_0))} + \mathbf{x_0}$= characteristic curve.

Next, we present sufficient conditions for the existence and uniqueness of a global smooth solution for all time, to the Cauchy problem (1.3).

Proposition 4.2. Suppose that the initial solution $u_0 \in C^1(\mathbb{R})$ and $f \in C^2(\mathbb{R})$ such that $f''u_0' > 0$, then the function $u(t,x) = u_0(x_0(t,x))$, is well defined for all domain and is the unique global solution to the Cauchy problem.

Proof. Consider the derivative of function $x(t;x_0)$ with respect to x_0,

$$\frac{\partial x(t;x_0)}{\partial x_0} = tf''(u_0(x_0))u_0'(x_0) + 1 > 0, \forall\, t\ \in \mathbb{R}^+.$$

Hence, the relation (1.5) can be inverted. Moreover, the implicit function theorem, ensures that $[(t,x) \to x_0(t,x)]$ is C^1 function. We now verify $u(t,x) = u_0(x_0(t,x))$ is a solution to the Cauchy problem. Eq. (1.4) gives $x_0(0,x) = x_0$, and $u(0,x) = u_0(x_0(0,x)) = u_0(x_0)$. Thus,

$$\begin{aligned}
\partial_t u + \partial_x(f(u)) &= \partial_t(u_0(x_0(t,x))) + \partial_x(f(u_0(x_0(t,x)))),\\
&= u_0'(x_0)\partial_t(x_0(t,x)) + f'(u_0(x_0))u_0'(x_0)\partial_x(x_0(t,x)),\\
&= u_0'(x_0)\left(\partial_t(x_0(t,x)) + f'(u_0(x_0))\partial_x(x_0(t,x))\right). \qquad (1.6)
\end{aligned}$$

Taking the derivative of Eq. (1.5) with respect to x and t,

$$\begin{aligned}
1 &= (t.f''(u_0)u_0' + 1)\partial_x(x_0(t,x)), \qquad (1.7)\\
-f'(u_0) &= (t.f''(u_0)u_0' + 1)\partial_t(x_0(t,x)). \qquad (1.8)
\end{aligned}$$

From Eqs. (1.6), (1.7) and (1.8), we obtain the required result.

Remark 4.3. If f'' and u_0' have the same sign, the characteristics do not intersect and we can construct a smooth solution $u(t,x)$ for all time $t \geq 0$.
What happens if f'' and u_0' have different sign in an interval $[a,b]$?
In this situation the above proposition is still hold but for small values of t, because $\dfrac{\partial x(t;x_0)}{\partial x_0} = t.g'(x_0) + 1 \sim 1$ if $t \sim 0$. For large value of t, we expect the formation of shock. Next we defined the breaking time and the location where the first shock occurs?

Breaking time. It is well known that when the characteristic curves cross to each other, the corresponding solution becomes multivalued and generates a shock. The time at which this incident occurs for the first time is called the breaking time. In order to find the breaking time, consider two characteristics curve that start from the point x_1 and $x_2 = x_1 + \Delta x$, where Δx is a small positive constant. They will intersect only when,

$x_0 + a(u_0(x_1))t = x_2 + a(u_0(x_2))t \implies t\left[a(u_0(x_1)) - a(u_0(x_2))\right] = -(x_1 - x_2)$,

$$t = -\frac{(x_1 - x_2)}{a(u_0(x_1)) - a(u_0(x_1 + \Delta x))}.$$

Assume $\Delta x \to 0$, then t converge to $-\dfrac{1}{a'(u_0(x))}$.

Now for the breaking time t_s, we need to find the minimum value for t

$$t_s = \min_{x\in\mathbb{R}} \left[-\frac{1}{a'(u_0(x))} \right].$$

Remark 4.4. The solution of Cauchy problem determined by method of characteristic is valid only before the breaking time, i.e. $t < t_s$. After the breaking time we have to insert a shock wave into the multivalued graph in such a way so that conservation law is preserved. Further, we see that the correct insert point is determined by Rankine-Hugoniot jump condition.

Integral/weak solution. The only way to construct a solution after the breaking time is to introduce discontinuity of u, that is called a shock. This can be done through a weak solution, since the derivatives do not exist at a discontinuity in classical sense.

Let us consider a test function $\phi \in C_0^\infty([0,\infty)\times\mathbb{R})$ and multiply Eq.(1.3) by $\phi(t,x)$ and integrate on $[0,\infty)\times\mathbb{R}$,

$$\int_{-\infty}^{\infty}\int_{0}^{\infty} [u_t + f(u)_x]\,\phi(t,x)\,dt\,dx = 0.$$

The main idea is to shift the derivative onto the smooth test function ϕ. For this purpose, we take the integration by parts and obtain,

$$\int_{-\infty}^{\infty}\int_{0}^{\infty} [\phi_t u + \phi_x f(u)]\;dt\,dx + \int_{-\infty}^{\infty} u_0(x)\phi(0,x)\,dx = 0. \tag{1.9}$$

The above integral equation is valid for all smooth test function ϕ. Moreover, we can see that there is no derivative of u.

Converse: We now assume that u is a smooth function and take the integration by parts in the reverse order, we obtain

$$\int_{-\infty}^{\infty}\int_{0}^{\infty} [u_t + f(u)_x]\,\phi(t,x)\,dt\,dx + \int_{-\infty}^{\infty} [u_0(x) - u(0,x)]\,\phi(0,x)\,dx = 0. \tag{1.10}$$

Suppose that the test function $\phi(t,x)$ is zero for $t = 0$, and the arbitrariness of ϕ implies

$$u_t + f(u)_x = 0 \text{ in } \;([0,\infty)\times\mathbb{R}). \tag{1.11}$$

We now assume that ϕ is non zero for $t = 0$, from Eqs. (1.10) and (1.11), we get

$$\int_{-\infty}^{\infty} [u_0(x) - u(0,x)]\,\phi(0,x)\,dx = 0.$$

Again the the arbitrariness of ϕ implies $u(0,x) = u_0(x)$ in $\mathbb{R}$. Hence, u is the solution of (1.3).

Remark 4.5. If u is a smooth function and satisfy Eq. (1.9), then u also satisfy Eq.

(1.3). In contrast, if u is only a bounded function, then u satisfy Eq. (1. 4.9) but does not satisfy Eq. (1.3).

Definition 4.4. *Assume that $u_0 \in L^\infty_{loc}(\mathbb{R})$. A function $u \in L^\infty([0,\infty)\times\mathbb{R})$ is a weak/integral solution of Cauchy problem (1.3) if Eq. (1.9) is satisfied for all test function $\phi \in C^\infty([0,\infty)\times\mathbb{R})$.*

The Rankine-Hugoniot jump condition. The condition gives the shock position at a time t which can be determined by the integral form of Eq. (1.3) on $x_1 < x < x_2$,

$$\frac{d}{dt}\int_{x_1}^{s(t)} u(t,x)dx + \frac{d}{dt}\int_{s(t)}^{x_2} u(t,x)dx = f(u(t,x_1)) - f(u(t,x_2)),$$

$$\int_{x_1}^{s(t)} u_t(t,x)dx + \lim_{x\to s(t)^+} u(t,x)s'(t) + \int_{s(t)}^{x_2} u_t(t,x)dx - \lim_{x\to s(t)^-} u(t,x)s'(t)$$

$$= f(u(t,x_1)) - f(u(t,x_2)),$$

$$-\int_{x_1}^{s(t)} f_x(u(t,x))dx + u(t,s(t)^+)s'(t) - \int_{s(t)}^{x_2} f_x(u(t,x))dx - u(t,s(t)^-)s'(t)$$

$$= f(u(t,x_1)) - f(u(t,x_2)),$$

$$-f(u(t,s(t)^+)) + f(u(t,s(t)^-)) + \left[u(t,s(t)^+) - u(t,s(t)^-)\right]s'(t) = 0.$$

Assume that $u(t,s(t)^+) = u_R,\ u(t,s(t)^-) = u_L$

$$\boxed{\mathbf{s'(t)} = \frac{\mathbf{f(u_L)} - \mathbf{f(u_R)}}{\mathbf{u_L} - \mathbf{u_R}} = \text{Rankine-Hugoniot jump condition.}}$$

Remark 4.6. *The discontinuous solution satisfies the Rankine-Hugoniot jump condition along the curve of discontinuity.*

Theorem 4.1. Let us assume that u belongs to piecewise C^1 class. Then u is a weak solution of Cauchy problem (1.3) if and only if two following conditions are satisfied

- u satisfy Eq. (1.3) in the domains where u belongs to class C^1.
- u satisfies the Rankine-Hugoniot jump condition along the curve of discontinuity s.

The proof of the theorem can be found in [114]. Next we will show that the Cauchy problem (1.3) may admit more than one weak solution.

Non-uniqueness. Let us consider the Burgers equation

$$u_t + \left(\frac{u^2}{2}\right)_x = 0,\ x\in\mathbb{R},\ t>0, \tag{1.12}$$

$$u(0,x) = \begin{cases} 0 & \text{if } x < 0; \\ 1 & \text{if } x > 0. \end{cases}$$

The corresponding characteristics curve are:

$$x(t,x_0) = x_0 + tu_0(x_0) = \begin{cases} x_0 & \text{if } x_0 \leq 0 \\ x_0 + t & \text{if } x_0 \geq 0, \end{cases} \text{ and } x_0 = \begin{cases} x & \text{if } x < 0 \\ x - t & \text{if } x > t. \end{cases}$$

Therefore

$$u(t,x) = \begin{cases} 0 & \text{if } x \leq 0; \\ 1 & \text{if } x \geq t. \end{cases}$$

We notice that the region $S = \{0 < x < t\}$ is not covered by the method of characteristics. We can cover this gap through the rarefaction wave solution

$$u_1(t,x) = \begin{cases} 0 & \text{if } x \leq 0; \\ (f')^{-1}\left(\frac{x}{t}\right) = \left(\frac{x}{t}\right) & \text{if } 0 < x \leq t \\ 1 & \text{if } x \geq t, \end{cases}$$

and the shock wave solution

$$u_2(t,x) = \begin{cases} 0 & \text{if } x < s(t); \\ 1 & \text{if } x > s(t), \end{cases}$$

where $s'(t)$ is the position of a shock at time t determined by the Rankine-Hugoniot jump condition

$$s'(t) = \frac{f'(u_L) - f'(u_R)}{u_L - u_R} = \frac{u_L + u_R}{2} = \frac{1}{2}.$$

Given the initial solution is discontinuous at $x = 0$, therefore the shock curve begins at the point $s(0) = 0$, which is given by $s(t) = \frac{t}{2}$. Since we have two weak solutions corresponding to the problem (1.12), therefore, we need to find a criteria that allows us to pick out "physical relevant solution". Thus, we present different versions of Entropy condition for convex flux function f.

Entropy Condition (version 1): A weak solution $u(t,x)$ is an entropy solution if all the discontinuities satisfy the following property

$$f'(u_l) > s'(t) > f'(u_r). \tag{1.13}$$

The above condition is equivalent to $u_l > u_r$, since f is convex flux function. In our case u_2 does not satisfy the above entropy condition, since $u_l = 0$ $u_r = 1$ $s'(t) = \frac{t}{2} \implies f'(u_l) \not> S'(t) \not> f'(u_r)$. In general, we say that any weak solution is admissible only when

it becomes a shock curve along the curve of discontinuity $s(t)$. In our case u_2 is not a shock curve along the curve of discontinuity $s(t) = t/2$. Hence, we reject this solution and keeping the continuous solution u_1. For general flux functions, Oleinik gave another version of above entropy condition.

Entropy condition (Oleinik [115])(version 2). $u(t,x)$ is the entropy solution if all the discontinuities satisfy the following property

$$\frac{f(u)-f(u_l)}{u-u_l} \geq s \geq \frac{f(u)-f(u_r)}{u-u_r}, \tag{1.14}$$

for all u between u_l and u_r.

Entropy condition (version 3). A weak solution $u(t,x)$ is an entropy solution if there exist a constant E such that

$$u(t,x+z)-u(t,x) < \frac{E}{t}z, \tag{1.15}$$

for all $z > 0,\ t > 0, x \in \mathbb{R}$. This version of entropy condition is useful for numerical methods where the Eq.(1.13) is difficult to apply for numerical solutions.

We now an introduce another approach for the entropy condition, in which we need to define an entropy function that satisfy an additional conservation laws for smooth solutions. Further this conservation laws becomes an inequality for discontinuous solutions.

Definition 4.5. *A convex continuous function $U : \mathbb{R} \to \mathbb{R}$ is said to be an entropy for the Cauchy problem (1.3) if there exist an entropy flux $F : \mathbb{R} \to \mathbb{R}$ such that the following relation*

$$U'(u)f'(u) = F'(u), \tag{1.16}$$

holds. Here u denotes the smooth solution of Cauchy problem and $f(u)$ represents the corresponding flux function.

Remark 4.7. If u is a smooth solution of Cauchy problem (1.3), then it satisfies the following conservation laws

$$\partial_t U(u) + \partial_x F(u) = 0, \tag{1.17}$$

provided the relation (1.16) holds.

Since u is smooth solution of (1.3) then

$$u_t + f(u)_x = 0 \implies U'(u)\,(u_t + f(u)_x) = 0, \text{ since } U(u) \text{ is convex continuous function,}$$

and by (1.16), we have

$$\partial_t U(u) + \partial_x F(U) = 0.$$

However, the above relation (1.17) doesn't hold for the discontinuous solutions, since the Rankine-Hugoniot conditions corresponding to Eq. (1.3) and above Eq. (1.17) are generally not equivalent.

Remark 4.8. To find the entropy functions for the system of nonlinear conservation laws is a much more difficult task. However, for the scalar conservation laws any convex function U is an entropy, which is sufficient for the computation of $F(u) = U'f'$.

The Vanishing viscosity method. It is well known that the entropy condition will provide physically relevant weak solution for Eq.(1.3). To make this point clear, we introduce a viscosity term $\epsilon\Delta u_\epsilon$. As a result, we get the parabolic equation

$$\begin{aligned} &\partial_t(u_\epsilon) + \partial_x f(u_\epsilon) = \epsilon\Delta u_\epsilon \\ &u_\epsilon(0,x) = u_{\epsilon 0}(x), \end{aligned} \tag{1.18}$$

where ϵ is a small positive diffusion coefficient. Next, we want to find the entropy solution u of (1.3). For the sake of entropy solution, we can state the following theorem.

Theorem 4.2. Suppose that the Cauchy problem (1.3) admits an entropy pair (U, F) and let $(u_\epsilon)_\epsilon$ be sequence of classical smooth solution of Eq.(1.18) such that

$$\|u_\epsilon\|_{L^\infty([0,\infty)\times\mathbb{R}} \leq C, \tag{1.19}$$

where C is a positive constant and independent of ϵ.

$$u_\epsilon \to u \text{ as } \epsilon \to 0 \text{ a.e. in } [0,\infty)\times\mathbb{R}. \tag{1.20}$$

Then u is a weak solution of Eq.(1.3) and satisfy the entropy condition

$$\frac{\partial}{\partial t}U(u) + \frac{\partial}{\partial x}F(U) \leq 0, \tag{1.21}$$

in the sense of distribution on $[0,\infty)\times\mathbb{R}$, i.e.

$$\int_{\mathbb{R}_+}\int_{\mathbb{R}} \left(U(u)\partial_t\phi + F(u)\partial_x\phi\right)\, dx\, dt \geq 0,\ \forall\ \phi \in C_0^\infty([0,\infty)\times\mathbb{R}). \tag{1.22}$$

In general these two inequalities (1.21) and (1.22) are equivalent. Let us assume that $U \in C^2$ be an entropy function, and applying $U'(u_\epsilon)$, to Eq.(1.15) we get,

$$\partial_t U(u_\epsilon) + \partial_x F(u_\epsilon) = \epsilon U'(u_\epsilon)\Delta u_\epsilon,$$

Since $\Delta^2 U(u_\epsilon) = \partial_x^2(U(u_\epsilon)) = \partial_x\left(\partial_x(U(u_\epsilon))\right) = \partial_x\left(U'(u_\epsilon)(u_\epsilon)_x\right) = U''(u_\epsilon)(u_\epsilon)_{xx} + U'(u_\epsilon)\Delta u_\epsilon$,

we rewrite the right hand side of above equation and use the convexity of U,

$$\epsilon U'(u_\epsilon)\Delta u_\epsilon = \epsilon \Delta U(u_\epsilon) - \epsilon U''(u_\epsilon)\frac{\partial^2 u_\epsilon}{\partial x^2} \leq \epsilon \Delta U(u_\epsilon).$$

Thus, we have

$$0 \leq \epsilon \Delta U(u_\epsilon) - \partial_t U(u_\epsilon) - \partial_x F(u_\epsilon).$$

Multiplying the above inequality by smooth test function $\phi \in C_0^\infty([0,\infty)\times\mathbb{R})$ and integrate on $[0,\infty)\times\mathbb{R}$, we obtain

$$0 \quad \leq \int_0^\infty \int_{\mathbb{R}} \left(\epsilon U(u_\epsilon)\Delta\phi + U(u_\epsilon)\partial_t\phi + F(u_\epsilon)\partial_x\phi\right)\, dx\, dt + \int_{\mathbb{R}} U(u_{\epsilon 0}(x))\phi(0,x)dx.$$

Let us assume that $(u_\epsilon)_\epsilon$ is a sequence of sufficiently smooth solution of Eq. (1.15) (with $u_\epsilon(0,x) = u_{\epsilon 0}(x) \to u_0(x)$ as $\epsilon \to 0$) which satisfies the conditions (1.16) and (1.17), then we obtain the required result, i.e.

$$\int_0^\infty \int_{\mathbb{R}} \left(U(u)\partial_t\phi + F(u)\partial_x\phi\right)\, dx\, dt + \int_{\mathbb{R}} U(u_0(x))\phi(0,x)dx \geq 0.$$

4.2 Introduction to the Finite Volume Scheme

Consider a scalar transport equation

$$\begin{cases} \partial_t u(t,x) + \partial_x u(t,x) = 0,\ t>0,\ x\in\mathbb{R}, \\ u(0,x) = u_0(x),\ x\in\mathbb{R}. \end{cases} \tag{1.23}$$

The principal of finite volume method for a partial differential equation is to decompose the domain into the small control volumes (grid cells) and integrate the equation over each volumes. Let us assume that the decomposition of the domain, $[0,\infty)\times\mathbb{R}$, is

$$[0,\infty)\times\mathbb{R} = \bigcup_{n\geq 0}\bigcup_{i\in\mathbb{Z}} [n\Delta t,(n+1)\Delta t)\times[i\Delta x,(i+1)\Delta x).$$

We now integrate Eq. (1.23) on one of the small rectangles, say $[n\Delta t, (n+1)\Delta t) \times [i\Delta x, (i+1)\Delta x)$,

$$\int_{i\Delta x}^{(i+1)\Delta x} u((n+1)\Delta t, x)dx - \int_{i\Delta x}^{(i+1)\Delta x} u(n\Delta t, x)dx + \int_{n\Delta t}^{(n+1)\Delta t} u(t, (i+1)\Delta x)dt - \int_{n\Delta t}^{(n+1)\Delta t} u(t, i\Delta x)dt = 0. \quad (1.24)$$

We now assume that the approximate value of u at time $t = n\Delta t$ on the space mesh $[i\Delta x, (i+1)\Delta x)$ is $\bar{u}_i^n$, and the approximate value of u at $i = \Delta x$ on $[n\Delta t, (n+1)\Delta t)$ is $\hat{f}_i^n$ (see, Fig. 1.7).

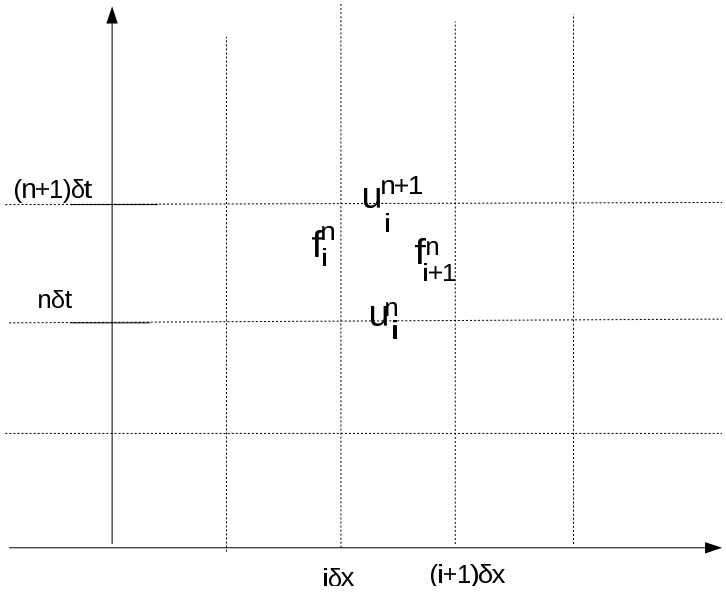

Figure 1.7: Discretization of the domain $[0, \infty) \times (-\infty, \infty)$

Divide the above Eq. (1.24) by Δt, we obtain

$$\forall\, n \geq 0,\ \forall\, i \in \mathbb{Z}:\ \frac{\Delta x}{\Delta t}\left(\bar{u}_i^{n+1} - \bar{u}_i^n\right) + \hat{f}_{i+1}^n - \hat{f}_i^n \approx 0. \quad (1.25)$$

If we represent $\hat{f}_i^n$ in terms of $(\bar{u}_j^n)_{j\in\mathbb{Z}}$, the above Eq. (1.26) would provide a way to find the values of $(\bar{u}_i^{n+1})_{i\in\mathbb{Z}}$, in terms of $(\bar{u}_i^n)_{i\in\mathbb{Z}}$. Further, we obtain all the values $(\bar{u}_i^n)_{n\geq 0,\, i\in\mathbb{Z}}$ from $(\bar{u}_i^0)_{i\in\mathbb{Z}}$. The values $(\bar{u}_i^0)_{i\in\mathbb{Z}}$ are determined by several simple choices, for example

$$\forall i \in \mathbb{Z}: \bar{u}_i^0 = \frac{1}{\Delta x}\int_{i\Delta x}^{(i+1)\Delta x} u_0(x)dx, \quad (1.26)$$

or even, u_0 is smooth function, $\bar{u}_i^0 = u_0(i\Delta x + \frac{\Delta x}{2})$.
Next step is to find the suitable expression for $\hat{f}_i^n$ in terms of $(\bar{u}_j^n)_{j\in\mathbb{Z}}$ such that the numerical solutions $(\bar{u}_i^n)_{i\in\mathbb{Z}}$ are indeed close to exact solution of (1.24) whenever the time and space steps tends to zero.
Centered Scheme. The simple choice is to approximate $\hat{f}_i^n$ at $x = i\Delta x$, by using the mean value of $\bar{u}_{i-1}^n$ and $\bar{u}_i^n$

$$\hat{f}_i^n = \frac{\bar{u}_{i-1}^n + \bar{u}_i^n}{2}. \tag{1.27}$$

Then Eq. (1.25) can be written as

$$\forall\, n \geq 0,\ \forall\, i \in \mathbb{Z}:\ \frac{\Delta x}{\Delta t}\left(\bar{u}_i^{n+1} - \bar{u}_i^n\right) + \frac{\bar{u}_{i+1}^n - \bar{u}_{i-1}^n}{2} = 0. \tag{1.28}$$

The resulting system [(1.26), (1.28)] does not hold the *maximum principle* (the values of the solution of the governed PDE remain the minimum and maximum values of the initial data).
Let us consider the Riemann initial condition and using Eq. (1.27), we have for all j,

$$u_j^0 = \begin{cases} 0, & j < 0, \\ 1, & j \geq 0. \end{cases}$$

The approximate value $u_{-1}^1 = \frac{-\Delta t}{2\Delta x} < 0$ at $t = \Delta t$ is not staying between the minimum and maximum approximate values of the initial data which violates the maximum principle. The results of the centered scheme exhibit the oscillation and it can be seen in the Figs. (1.8) and (1.9).

Upwind scheme. As we already see that the centered scheme is not appropriate for Eq. (1.23), actually it could be predicted by using the physical elucidation of the PDE. For obtaining the conservation laws $\partial_t u + \partial_x(au) = 0$, we first express the conservation of u inside the control volume $[i\Delta x, (i+1)\Delta x)$ as Eq.(1.24), in which $\int_{n\Delta t}^{(n+1)\Delta t} u(t, i\Delta x)dt$ comes as the quantity of u that transported with velocity a via the interface $x = i\Delta x$. If the velocity $a > 0$, this quantity comes from $[(i-1)\Delta x, i\Delta x)$ and goes into $[i\Delta x, (i+1)\Delta x)$. Due to this fact, we would approximate the quantity $\int_{n\Delta t}^{(n+1)\Delta t} u(t, i\Delta x)dt$ by using the value of u that comes from the control volume $[(i-1)\Delta x, i\Delta x)$. Hence we take

$$\hat{f}_i^n = \bar{u}_{i-1}^n,$$

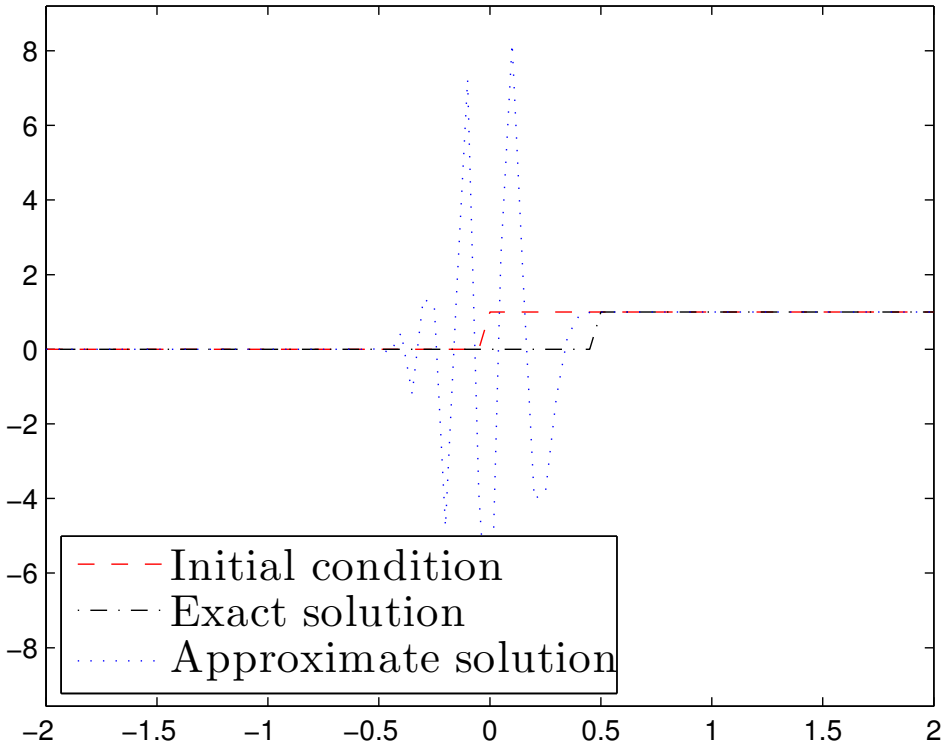

Figure 1.8: Comparison between exact and approximate solution determined by centered scheme, for $\partial_t u + \partial_x u = 0.$ at time $t = 0.5$ with $\Delta t = \Delta x = 0.05$

and then the scheme in (1.25) is written $\forall n \geq 0,\ \forall i \in \mathbb{Z}$,

$$\frac{\Delta x}{\Delta t}(\bar{u}_i^{n+1} - \bar{u}_i^n) + \bar{u}_i^n - \bar{u}_{i-1}^n = 0. \tag{1.29}$$

This scheme is called the upwind scheme (see results in Fig. (1.10)) because it is made up by the upwind (with respect to the velocity a) choice for the computation of flux values. On the contrary to the centered scheme, the upwind scheme hold the Maximum principle.

Proposition 4.3. *Under the condition*

$$a\ \Delta t \leq \Delta x, \tag{1.30}$$

where $a, \Delta t$ and Δx all are non-negative, the solution $(u_i^n)_{n\geq 0,\, i\in\mathbb{Z}}$ of upwind scheme (1.29) satisfy the following properties

$$\inf_{j\in\mathbb{Z}} \bar{u}_j^n \leq \bar{u}_i^{n+1} \leq \sup_{j\in\mathbb{Z}} \bar{u}_j^n,\ \forall j,\ n \geq 0. \tag{1.31}$$

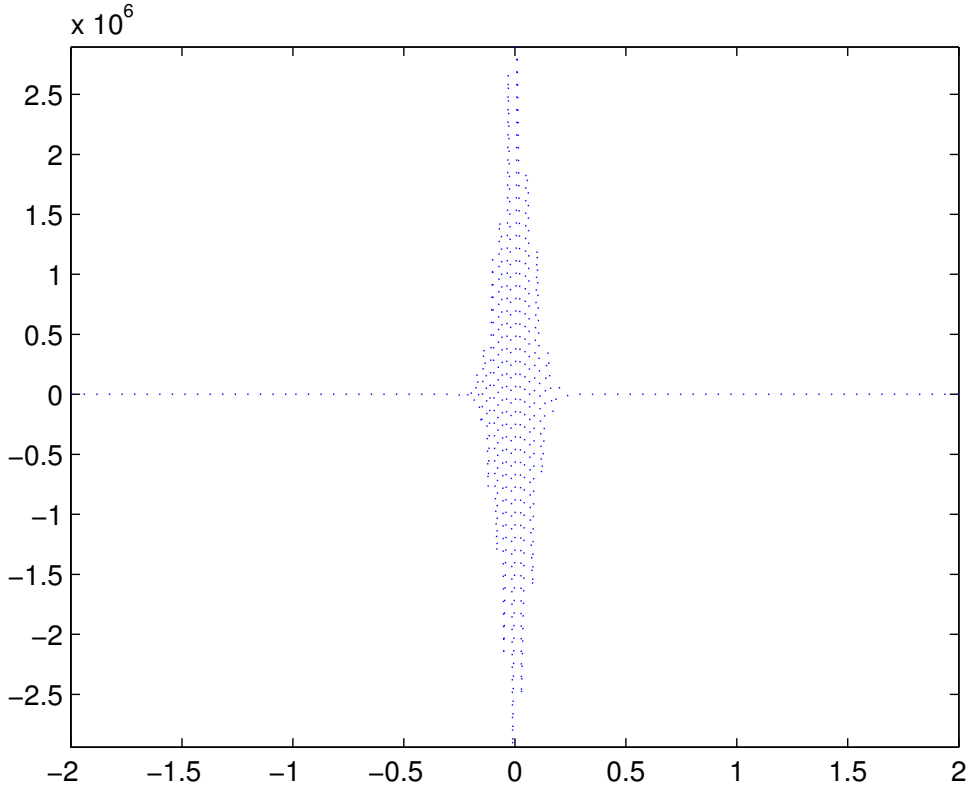

Figure 1.9: Approximate solution determined by centered scheme, for $\partial_t u + \partial_x u = 0.$ at time $t = 0.5$ with $\Delta t = \Delta x = 0.01$

In particular all the values of solution $(u_i^n)_{n\geq 0,\, i\in\mathbb{Z}}$ *stay between the minimum and maximum value of* $\bar{u}_i^0$.

Proof. Rewrite the Eq. (1.29) as follows

$$\bar{u}_i^{n+1} = \left(1 - \frac{a\Delta t}{\Delta x}\right)\bar{u}_i^n + \frac{a\Delta t}{\Delta x}\bar{u}_{i-1}^n.$$

Under the condition (1.30), the coefficients of $\bar{u}_i^n$ and $\bar{u}_{i-1}^n$ are non-negative, and sum is equal to 1. Hence, $\bar{u}_i^{n+1}$ is convex combination of $\bar{u}_i^n$ and $\bar{u}_{i-1}^n$ and therefore it is between these two numbers. Thus the relation (1.31) hold for all j and n, and remaining part of the proposition is deduced by this relation. ■

5 Thesis Organization

The thesis is organized into 7 chapters. A brief outline is given below:

- **Chapter 1: Introduction and Related Work**

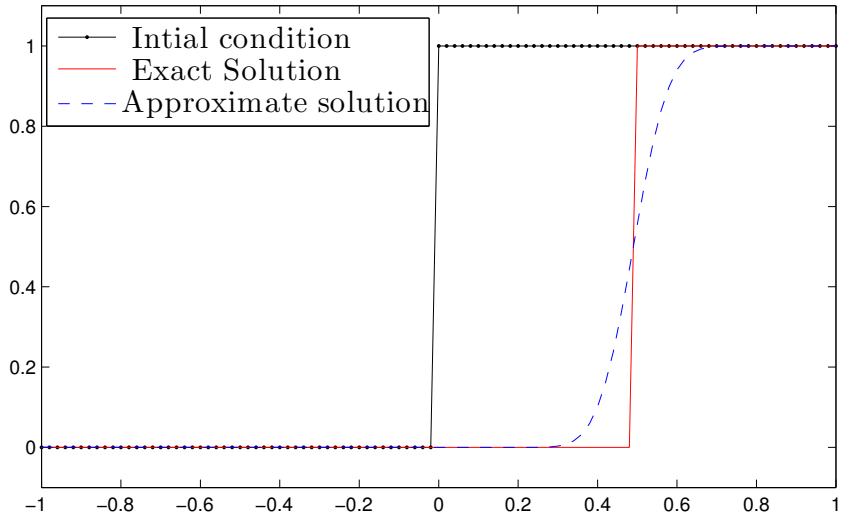

Figure 1.10: Approximate solution determined by upwind scheme, for $\partial_t u + \partial_x u = 0$. with Riemann initial data, at time $t = 0.5$ with $\Delta t = 0.01, \Delta x = 0.02$.

This chapter begins with the overview of mathematical models motivated from computational biology and numerical approximation of solutions and then moves on computational biology. Here it discusses the neurons' structure and its behaviors. Further, it presents the literature survey on computational neuroscience and the population dynamics. This chapter also introduces the theory of the governing equation related to this study. Further, it summarizes the finite volume method that is used in this study.

- **Chapter 2: MUSCL Scheme for Transport Equation Arising in a Neuronal Model**

  This Chapter starts with a brief background of nervous system and their related model. Further, it presents the proposed numerical scheme based on FVM, which is used to find the approximate solution of the governing model equation. The chapter also discusses the stability of the proposed framework. To evaluate the performance of proposed approach, test examples have been considered.

  The paper [116] containing this work has been published in "Computers & Mathematics with Applications", Elsevier, 2015.

- **Chapter 3: A Numerical Treatment of a Population Density Model Based on Quadratic-Integrate-And-Fire Neuron**

  This Chapter introduces a population density model based on quadratic-integrate-and-fire neuron. The Chapter starts with the overview of quadratic integrate-and-fire neuron model for deriving of governing equation with the help of population

density approach. The chapter further also presents high-order numerical scheme to find the approximate solution of model equation. Finally, numerical experiments are taken to demonstrate both the effectiveness and the efficiency of our proposed method. The chapter concludes with performance evaluation of the proposed work. The research of this work has been submitted for review in peer-reviewed journal.

- **Chapter 4: A Numerical Study of the Excitatory and Inhibitory Population Density Model**
  This Chapter presents the excitatory and inhibitory population density model based on leaky-integrate-and-fire neuron with potential jumps. The synaptic connection between neurons is modeled by a potential jump at the receiving of input current. The chapter also presents a high-order numerical scheme to find the approximate solution of the governing equation. Further, it includes the diffusion approximation, is used to avoid the non-local terms. The efficiency and accuracy of the proposed scheme is tested through numerical experiments.
  The research of this work is submitted in refereed international journal.

- **Chapter 5: Numerical Solver of Size Structured Neuron Model**
  This Chapter deals with size structured neuron model based on the articles [1, 2]. This model consists a transport equation with age-dependance and spatial structure. Moreover, the governing equation is the renewal equation for demography. The chapter also introduces a finite volume approximation for the simulation of transport equation. Theoretical analysis of the proposed framework is also discussed in this study.
  The research work in this chapter [117] has been appeared in "Differentials Equations and Dynamical System", Springer, 2017.

- **Chapter 6: IMEX-WENO Finite Volume Approximation for Nonlinear Age-Structured Population Model**
  This Chapter deals with nonlinear age-structured population model. The model consists a real biological situation in which all human beings have a finite maximum age. The model comprises the fertility and mortality factors, which depend on the age, seasonality and external resources in which intrinsic mortality is unbounded. This chapter presents high-order accurate numerical scheme to approximate the solution of the model equation. To validation of the proposed framework, some numerical experiments introduce in this chapter.
  The research work in this chapter has been published in "International Journal of Computer Mathematics", Taylor & Francis, 2018 [118].

- **Chapter 7: Conclusions and Future Scope**

  This chapter concludes the study and discuss on some future directions of present work.

  The relevant references are appended at the end of thesis.

Chapter 2

MUSCL Scheme for Transport Equation Arising in a Neuronal Model [1]

The first chapter discussed the introduction and state-of-the-art numerical methods in the simulation of biological models. We observed from the existing literature that the synaptic input current and high-order numerical scheme is not considered in the Stein's neuronal model. To fill this gap, the synaptic current has been used, and a high-order MUSCL (Monotonic Upwind Scheme for Conservation Laws) Finite Volume Method (FVM) has been proposed. This chapter starts with a brief background of neuron and considers a transport equation with mixed boundary conditions (Dirichlet and Neumann) originating in a neuronal model. This equation contains point-wise delay and advanced argument. Chapter then presents the stability and convergence of the proposed scheme. The importance of this scheme is that it is valid for large as well as for small values of point-wise delay and advance. Some test examples are included to examine the behavior of the solution and to verify the order of convergence. The effect of point-wise delay and advance arguments on the solution is shown graphically.

1 Introduction

The fundamental processing unit of control nervous system is a neuron [119]. In human brain it is approximately 10^{12}. A typical neuron have three main components-dendrites, soma and axon which correspond to input, processing and output functions, respectively. The dendrites is the main input of a neuron, which adds up the output signals in the form of an electrical potential and it diffuses along the tree to the soma. If the total potential at the soma exceeds a certain threshold value, the neuron produces a short electrical spike or action potential, which is then conducted along the axon. The contacts of the axon to the target neuron are either located on the dendrite tree or directly on the soma and these contacts are called synapses. The arrival of an action potential at the synapse induces the

[1] Santosh Kumar and Paramjeet Singh *"Higher-order MUSCL scheme for transport equation originating in a neuronal model"*, Computers & Mathematics With Applications, Elsevier, 70(12): 2838-2853, 2015.

secretion of a neurotransmitter, as a result the membrane potential of targeted neuron changes. Moreover, the incoming impulse at the synapses either increases or decreases the post-synaptic potential and respective synapses are called excitatory or inhibitory.

Mathematical Model

Various types of mathematical models for biological neurons have been developed to represent the biological activities. Many authors used different approaches (statistical, analytical, and numerical) to discuss the activity of a neuron or neural network. In 1965 Stein gave an integrate-and-fire neuron model [17]. He discussed the distribution of neuronal firing intervals, neuronal firing rat e, and strength-duration curves below the threshold level. A number of numerical approaches [120–122] have been developed and applied to this model. In the present study, the neuronal behavior is studied beyond the threshold level. For this reason, we introduce a threshold level r and assume that once the membrane potential of a neuron, V_t, at time t, surpasses r, it remains at the value $r + dr$ for all subsequent time, which is absorbing state in the language of Markov chain, i.e., $p(v, t) = 0, \forall v \geq r$. Here, $p(v, t)$ denote the probability that the membrane potential of a neuron is less than or equal to the given voltage, v, at time t. Then $1 - p(r, t)$ is cumulative probability of neuron firing up to time t. According to Stein [17], the membrane potential of a neuron decay exponentially for subthreshold values, i.e.,

$$\frac{dV_t}{dt} = -V_t/\tau.$$

The above equation is presented without any input current. In this chapter, the effect of synaptic input current in the above model equation is comprised.

$$\frac{dV_t}{dt} = \frac{-V_t + RI(t)}{\tau},$$

where τ is a time membrane constant and $RI(t)$ is the synaptic input current.
The rate of change of function $p(v, t)$ with respect to time is given by ([17, 120]),

$$\begin{aligned} p(v, t + \delta t) - p(v, t) &= [1 - (p_e + p_i)\delta t]\,[p(v + \delta v, t) - p(v, t)] \\ &\quad -p_e \delta t[p(v, t) - p(v - \alpha, t)] + p_i \delta t[p(v + \beta, t) - p(v, t)]. \end{aligned}$$

The first term in the right-hand side of the above equation corresponds to the increase in $p(v, t)$ from the decay of the potential during the time δt in some trials from just greater than v to v or less, providing no impulse occurs. The second term corresponds to the decrease in $p(v, t)$ from excitation of units between $v - \alpha$ and v while the third term corresponds to the increase in $p(v, t)$ from inhibition of units between v and $v + \beta$.

Dividing the above equation by δt, we obtain

$$\begin{aligned}\frac{p(v,t+\delta t)-p(v,t)}{\delta t} &= \frac{[p(v+\delta v,t)-p(v,t)]}{\delta t}-(p_e+p_i)\,[p(v+\delta v,t)-p(v,t)]\\ &\quad -p_e[p(v,t)-p(v-\alpha,t)]+p_i[p(v+\beta,t)-p(v,t)].\end{aligned}$$

Solving the above equation, we get

$$\begin{aligned}\frac{p(v,t+\delta t)-p(v,t)}{\delta t} &= \frac{[p(v+\delta v,t)-p(v,t)]}{\frac{\tau}{-v+R.I(t)}\delta v}-(p_e+p_i)\,[p(v+\delta v,t)-p(v,t)]\\ &\quad -p_e[p(v,t)-p(v-\alpha,t)]+p_i[p(v+\beta,t)-p(v,t)].\end{aligned}$$

Taking the limit as $\delta t \to 0$, we obtain

$$\frac{\partial p}{\partial t}=\frac{\partial p}{\partial v}\frac{1}{\tau}[-v+R.I(t)]-p_e[p(v,t)-p(v-\alpha,t)]+p_i[p(v+\beta,t)-p(v,t)].$$

On simplifying, we obtain

$$\frac{\partial p}{\partial t}-\left[\frac{\partial p}{\partial v}\frac{1}{\tau}(-v+R.I(t))\right]=p_e[p(v-\alpha,t)-p(v,t)]+p_i[p(v+\beta,t)-p(v,t)]. \tag{2.1}$$

$$\begin{aligned}&\frac{\partial p}{\partial t}+\frac{\partial}{\partial v}\left[-\frac{1}{\tau}(-v+R.I(t))p\right]=\frac{1}{\tau}p(v,t)+a(v,t)[p(v-\alpha,t)-p(v,t)]\\ &+b(v,t)[p(v+\beta,t)-p(v,t)],\ -\infty<v\le r.\end{aligned} \tag{2.2}$$

Here, $a(v,t)$ and $b(v,t)$ stand for the frequencies of excitatory and inhibitory impulses, respectively. The initial and boundary conditions are given by

$$\begin{aligned}&p(v,0)=p^0(v)\ge 0,\\ &p(v,t)=0,\ v\in[-\alpha,0],\\ &\frac{\partial p}{\partial t}(r,t)=a(r,t)[p(r,t)-p(r-\alpha,t)],\ p(v,t)=0,\ v\in[r,r+\beta].\end{aligned} \tag{2.3}$$

Equation (2.1) can be written in the standard form as,

$$p_t+f(p)_v=S(p),$$

where $f(p)=\left[-\frac{1}{\tau}(-v+RI(t))p\right]$ is a flux term and $S(p)=\frac{1}{\tau}p(v,t)+a(v,t)[p(v-\alpha,t)-p(v,t)]+b(v,t)[p(v+\beta,t)-p(v,t)]$ is the source term. The governing equation represents a hyperbolic conservation law having source term with the above initial and boundary conditions. Since synaptic current $RI(t)$, depends on the total activity of the network, therefore, $RI(t)=I_0+A\ N(t)$, where I_0 is the amplitude of the membrane potential, A is constant, and $N(t)$ represents the firing activity (firing rate) of the neurons at time t

defined as given in [1, 123],

$$N(t) = \int_{-\infty}^{r} \gamma(v)p(v,t)dv.$$

Here, term $\gamma(v)$ is the modeling coefficient satisfying $\int_{-\infty}^{r} \gamma(v)dv = 1$. The problem given by (2.1)-(2.3) cannot be solved by analytical methods [124–126] because the governing equation contains the difference terms, and the modelling coefficients are not constant. Several other authors modified the resulting model problem and obtained numerical solution with some restrictions, either on the size of the point-wise delay or on coefficients or both [120, 121]. Singh and Sharma [120, 121] used the procedure based on Taylor series approximation which is not suitable for the large size of shift arguments. The aforementioned authors only discussed the case when the neuron arrives up to a threshold level. In this chapter, we discussed the case when the neuron surpasses the threshold level and this situation occur only when the impulse is excitatory type. Thus, it is required to add the boundary condition of above type. We also included the intensity of incoming current in the original problem.

Ordinary differential equations with point-wise delay are well understood by now but there is no comparable theory for partial differential equations having time and space dependent unknowns. Here, we construct higher-order MUSCL finite volume approximation for the resulting Eq. (2.1). This scheme is valid for large size of delay as well as advance argument. The developed scheme is second-order accurate. Moreover, we used fractional step method and implicit factor to tackle the source term. Some authors [127, 128] have made contribution for the numerical solution of hyperbolic conservation law with source term but their procedure is based on explicit scheme. We handled the stability of developed scheme using the semi implicit procedure to preserve the stability and convergence.

In the next section, we discuss some preliminaries and define the notion of solutions. In Section 3, we develop the numerical scheme for governing equation. Stability and convergence analysis are given in Section 4. In Section 5, we report some numerical examples and discuss the behavior of the solution. In the last section we present summary about this chapter.

2 Preliminaries

In this section, we present the hypothesis on flux function f and source term S. We also state some preliminaries and definitions related to hyperbolic conservation law including

source term.

- $f \in C^m(\mathbb{R})$.
- $S(0) = 0, \quad S \in C^m(\mathbb{R})$ is Lipschitz with constant k.
- $S' \leq 0$.

Definition 2.1. *Bounded Variation (BV):* BV consist all those functions whose total variation

$$TV(p) = \sup_{h \neq 0} \int_{\mathbb{R}} \frac{|p(v+h) - p(v)|}{|h|}$$

is bounded.

In the non-homogeneous conservation laws, the characteristic curves is not a straight line along which the solution p is not necessarily a constant.

Let $p(v,t) = G(t)\ p_0$ denote the weak solution of Eqs. (2.1) and (2.3) which satisfy the entropy condition and also assume that

$$\sup_p S'(p) \leq k.$$

Now we recall the following Preposition, see [129].

Proposition 2.1. If the initial data $p_0 \in L^\infty(\mathbb{R}) \cap L^1(\mathbb{R})$, and flux function $f \in C^1(R)$, then the problem (2.1) and (2.3) have a unique entropy solution $p(v,t) = G(t)p_0$, satisfying following properties

(i) $\|G(t)p_0\|_{L^\infty(\mathbb{R})} \leq e^{kt}(\|p_0\|_{L^\infty(\mathbb{R})} + |S(0)t|)$.

(ii) $\|G(t)p_0 - G(t)q_0\|_{L^1(\mathbb{R})} \leq e^{kt}\|p_0 - q_0\|_{L^1(\mathbb{R})}$, provided $q_0 \in L^\infty(\mathbb{R})$.

(iii) $G(t)p_0 \leq G(t)q_0$, provided $p_0(v) \leq q_0(v)$.

With the help of this Proposition (2.4), we can prove the following results.

Taking $k = 0$ and $S(0) = 0$ in (i) and (ii) of Proposition (2.4), we have

$\|G(t)p_0\|_{L^\infty(\mathbb{R})} \leq \|p_0\|_{L^\infty(\mathbb{R})}$,

$\|G(t)p_0 - G(t)q_0\|_{L^1(\mathbb{R})} \leq \|p_0 - q_0\|_{L^1(\mathbb{R})}$.

Again, taking $k = 0$ and $q_0(v) = p_0(v+h)$ in Proposition (2.4), we get

$|G(t)p_0 - G(t)p_0(v+h)| \leq |p_0 - p_0(v+h)|$,

$|G(t)p_0(v+h) - G(t)p_0| \leq |p_0(v+h) - p_0|$,

$$\sup_{h \neq 0} \int_{\mathbb{R}} \frac{|G(t)p_0(v+h) - G(t)p_0|}{|h|} \leq \sup_{h \neq 0} \int_{\mathbb{R}} \frac{|p_0(v+h) - p_0(v)|}{|h|},$$

$$\implies TV(G(t)p_0) \leq TV(p_0).$$

3 The Numerical Scheme

In this section, we present a fractional step method for above Eq. (2.1) in which the problem is divided into two parts corresponding to the different process, and further appropriate numerical method is used to solve each part independently. The idea with the fractional step method is to combine these two approaches by applying the two methods in an alternating manner [130, 131]. Write the Eq. (2.1) as

Problem A : $\quad p_t + f(p)_v = 0.$

Problem B : $\quad p_t = S(p).$

We will solve Problem A by higher-order MUSCL finite volume approximation and Problem B will be solved by forward Euler for the ordinary differential equations. The solution procedure for the proposed scheme can be defined in following steps.
Construct a quadratic polynomial by Taylor's formula

$$\tilde{p}(v) = p(v_j) + (v - v_j)p_v(v_j) + \frac{1}{2}(v - v_j)^2 p_{vv}(v_j) + O(\Delta v^3),\ v \in I_j, \tag{2.4}$$

where $I_j = \left[v_{j-1/2}, v_{j+1/2}\right]$ is the j-th cell. Further $p(v_j) \neq p_j$. We want conservation, therefore ignoring the higher powers of Δv and get

$$\frac{1}{\Delta v}\int_{v_{j-1/2}}^{v_{j+1/2}} p(v)dv = p_j \implies p(v_j) + \frac{\Delta v^2}{24}p_{vv}(v_j) = p_j$$

$\implies p(v_j) = p_j - \dfrac{\Delta v^2}{24}p_{vv}(v_j)$. Thus Eq. (2.4) becomes

$$\tilde{p}(v) = p_j + (v - v_j)p_v(v_j) + \frac{1}{2}\left[(v - v_j)^2 - \frac{\Delta v^2}{12}\right]p_{vv}(v_j) + O(\Delta v^3).$$

Hence one using the quadratic polynomial in cell $(v_{j-1/2}, v_{j+1/2})$, we have

$$\tilde{p_j}(v) = p_j + (v - v_j)\frac{p_{j+1} - p_{j-1}}{2\Delta v} + \frac{3k}{2}\left[(v - v_j)^2 - \frac{\Delta v^2}{12}\right]\frac{(p_{j-1} - 2p_j + p_{j+1})}{\Delta v^2}.$$

Here, we have introduced the parameter k. Chooing $k = \frac{1}{3}$, provide third-order accuracy in the reconstruction. Using this value, we obtain the states at the cell faces at time level n.

$$\begin{aligned}
p^{n+}_{j-1/2} &= \tilde{p}^n_j(v_{j-1/2}),\\
&= p^n_j + (v_{j-1/2} - v_j)\frac{p^n_{j+1} - p^n_{j-1}}{2\Delta v} + \frac{3k}{2}\left[(v_{j-1/2} - v_j)^2 - \frac{\Delta v^2}{12}\right]\frac{(p^n_{j-1} - 2p^n_j + p^n_{j+1})}{\Delta v^2},\\
&= p^n_j - \frac{\Delta v}{2}\frac{(p^n_{j+1} - p^n_{j-1} + p^n_j - p^n_j)}{2\Delta v} + \frac{3k}{2}\left[\frac{\Delta v^2}{4} - \frac{\Delta v^2}{12}\right]\frac{(p^n_{j-1} - p^n_j - p^n_j + p^n_{j+1})}{\Delta v^2},\\
&= p^n_j - \frac{1}{4}(p^n_{j+1} - p^n_j) - \frac{1}{4}(p^n_j - p^n_{j-1}) + \frac{k}{4}(p^n_{j+1} - p^n_j) - \frac{k}{4}(p^n_j - p^n_{j-1}),
\end{aligned}$$

$$\therefore\ p^{n+}_{j-1/2} = p^n_j - \frac{1}{4}\left[(1-k)\Delta p^n_{j+1/2} + (1+k)\Delta p^n_{j-1/2}\right], \tag{2.5}$$

where $\Delta p^n_{j+1/2} = (p^n_{j+1} - p^n_j), \quad \Delta p^n_{j-1/2} = (p^n_j - p^n_{j-1})$.

Now

$$p^{n-}_{j-1/2} = \tilde{p}^n_{j-1}(v_{j-1/2}) = p^n_{j-1} + (v_{j-1/2} - v_{j-1})\frac{(p^n_j - p^n_{j-2})}{2\Delta v}$$
$$+ \frac{3k}{2}\left[(v_{j-1/2} - v_{j-1})^2 - \frac{\Delta v^2}{12}\right]\left(\frac{p^n_{j-2} - 2p^n_{j-1} + p^n_j}{\Delta v^2}\right).$$
$$= p^n_{j-1} + \frac{\Delta v}{2}\frac{(p^n_j - p^n_{j-1} + p^n_{j-1} - p^n_{j-2})}{2\Delta v} + \frac{3k}{2}\left(\frac{\Delta v^2}{4} - \frac{\Delta v^2}{12}\right)\frac{(p^n_{j-2} - p^n_{j-1} - p^n_{j-1} + p^n_j)}{\Delta v^2}.$$

After simplification and re-arranging the above terms, we obtain

$$p^{n-}_{j-1/2} = p^n_{j-1} + \frac{1}{4}\left[(1+k)\Delta p^n_{j-1/2} + (1-k)\Delta p^n_{j-3/2}\right]. \tag{2.6}$$

Similarly, we can compute $p^{n-}_{j+1/2}$ and $p^{n+}_{j+1/2}$, and the values are given by

$$p^{n-}_{j+1/2} = p^n_j + \frac{1}{4}\left[(1+k)\Delta p^n_{j+1/2} + (1-k)\Delta p^n_{j-1/2}\right].$$
$$p^{n+}_{j+1/2} = p^n_{j+1} - \frac{1}{4}\left[(1+k)\Delta p^n_{j+1/2} + (1-k)\Delta p^n_{j+3/2}\right].$$

In order to make the scheme TVD, we limit the reconstructed states $p^{n\ \pm}_{j+1/2}$. Firstly we write

$$p^{n+}_{j-1/2} = p^n_j - \frac{1}{4}\left[(1+k)\frac{\Delta p^n_{j-1/2}}{\Delta p^n_{j+1/2}}\Delta p^n_{j+1/2} + (1-k)\frac{\Delta p^n_{j+1/2}}{\Delta p^n_{j-1/2}}\Delta p^n_{j-1/2}\right].$$
$$p^{n-}_{j-1/2} = p^n_{j-1} + \frac{1}{4}\left[(1+k)\frac{\Delta p^n_{j-1/2}}{\Delta p^n_{j-3/2}}\Delta p^n_{j-3/2} + (1-k)\frac{\Delta p^n_{j-3/2}}{\Delta p^n_{j-1/2}}\Delta p^n_{j-1/2}\right].$$
$$p^{n+}_{j+1/2} = p^n_{j+1} - \frac{1}{4}\left[(1+k)\frac{\Delta p^n_{j+1/2}}{\Delta p^n_{j+3/2}}\Delta p^n_{j+3/2} + (1-k)\frac{\Delta p^n_{j+3/2}}{\Delta p^n_{j+1/2}}\Delta p^n_{j+1/2}\right].$$
$$p^{n-}_{j+1/2} = p^n_j + \frac{1}{4}\left[(1-k)\frac{\Delta p^n_{j-1/2}}{\Delta p^n_{j+1/2}}\Delta p^n_{j+1/2} + (1+k)\frac{\Delta p^n_{j+1/2}}{\Delta p^n_{j-1/2}}\Delta p^n_{j-1/2}\right].$$

We now introduce the parameter

$$Z^n_j = \frac{\Delta p^n_{j+1/2}}{\Delta p^n_{j-1/2}}$$

to measure the local smoothness of the function. We also introduce the limiter function ϕ,

$$p^{n+}_{j-1/2} = p^n_j - \frac{1}{4}\left[(1+k)\phi\left(\frac{1}{Z^n_j}\right)\Delta p^n_{j+1/2} + (1-k)\phi(Z^n_j)\Delta p^n_{j-1/2}\right].$$
$$p^{n-}_{j-1/2} = p^n_{j-1} + \frac{1}{4}\left[(1+k)\phi\left(Z^n_j\right)\Delta p^n_{j-3/2} + (1-k)\phi\left(\frac{1}{Z^n_j}\right)\Delta p^n_{j-1/2}\right].$$
$$p^{n+}_{j+1/2} = p^n_{j+1} - \frac{1}{4}\left[(1+k)\phi\left(\frac{1}{Z^n_{j+1}}\right)\Delta p^n_{j+3/2} + (1-k)\phi(Z^n_{j+1})\Delta p^n_{j+1/2}\right].$$

$$p^{n-}_{j+1/2} = p^n_j + \frac{1}{4}\left[(1-k)\phi\left(\frac{1}{Z^n_j}\right)\Delta p^n_{j+1/2} + (1+k)\phi(Z^n_j)\Delta p^n_{j-1/2}\right].$$

Remark 3.1. In smooth regions we expect $Z^n_j \approx 1$ and we should have $\phi(Z^n_j) \approx Z^n_j$. In particular, we need $\phi(1) = 1$ in order to obtain second-order accuracy in smooth regions.

Remark 3.2. The finite volume scheme with monotone Lipschitz continuous numerical flux

$$p^{n+1}_j = p^n_j - \lambda(F^n_{j+1/2} - F^n_{j-1/2}), \quad F^n_{j+1/2} = F(p^{n\,-}_{j+1/2}, p^{n\,+}_{j+1/2}),$$

where the states $p^{n\,\pm}_{j+1/2}$ are obtained by the k parameter MUSCL scheme, is TVD if

$$0 \le \phi(Z) \le \frac{3-k}{1-k} - (1+c)\frac{1+k}{1-k}, \quad 0 \le \frac{\phi(Z)}{Z} \le 2 + c, \quad c \in \left[-2, 2\frac{(1-k)}{1+k}\right],$$

under the CFL condition

$$\lambda\frac{[2-(2+c)]}{1-k}H_j \le 1, \quad H_j = \max_{u,v}\left|\frac{\partial F}{\partial u}(u, p^+_{j+1/2}) - \frac{\partial F}{\partial v}(v, p^-_{j+1/2})\right|.$$

Here the maximum is taken over all $u \in (p^-_{j-1/2},\ p^-_{j+1/2})$ and all $v \in (p^+_{j-1/2},\ p^+_{j+1/2})$.

Remark 3.3. The limiter function $\phi(Z) = \max(0, \min(Z, d)),\ d \in \left[1, \frac{3-k}{1-k}\right]$ satisfy the above condition. Thus, the numerical approximation for hyperbolic part of Eq. (2.1) is given by

$$p^{n+1}_j = p^n_j - \lambda(F^n_{j+1/2} - F^n_{j-1/2}), \quad F^n_{j+1/2} = F(p^{n\,-}_{j+1/2}, p^{n\,+}_{j+1/2}).$$

The flux $F^n_{j+1/2} = F(p^{n\,-}_{j+1/2}, p^{n\,+}_{j+1/2})$ is approximated by Godunov flux which can be written as

$$F^n_{j+1/2} = \begin{cases} \min\limits_{p^{n\,-}_{j+1/2} \le w \le p^{n\,+}_{j+1/2}} f(w), & \text{if } p^{n\,-}_{j+1/2} \le p^{n\,+}_{j+1/2} \\ \max\limits_{p^{n\,+}_{j+1/2} \le w \le p^{n\,-}_{j+1/2}} f(w), & \text{if } p^{n\,-}_{j+1/2} \ge p^{n\,+}_{j+1/2}. \end{cases}$$

The next step is to discretize the source term. Problem B is solved by the forward Euler method to obtain

$$p^{n+1}_j = p^n_j + \Delta t S(p^n_j),$$

where $S(p^n_j)$ is obtained by a linear interpolation.

$$S(p^n_j) = -\frac{1}{\tau}p^n_j + a^n_j\left[\frac{\alpha}{v_j - v_0}p^n_0 + \frac{v_j - \alpha - v_0}{v_j - v_0}p^n_j - p^n_j\right]$$

$$+ b^n_j\left[\frac{v_j + \beta - v_N}{v_j - v_N}p^n_j + \frac{\beta}{v_N - v_j}p^n_N - p^n_j\right], \forall j = 0, 1, 2, \ldots, N.$$

Here we take $p(v_0 - \alpha, t)$ and $p(v_N + \beta, t)$ equals to zero as $p(v, t) = 0$ outside the domain. Next step is to relate both numerical schemes through splitting method, which is given

as follows

$$\bar{p}_j^n = p_j^n + \Delta t\ S(\bar{p}_j^n). \tag{2.7}$$

$$p_j^{n+1} = \bar{p}_j^n - \frac{\Delta t}{\Delta v}\left[F(\bar{p}_{j+1/2}^{n-}, \bar{p}_{j+1/2}^{n+}) - F(\bar{p}_{j-1/2}^{n-}, \bar{p}_{j-1/2}^{n+})\right]. \tag{2.8}$$

We now compute the boundary conditions by integrating from time level t^n to t^{n+1}, to obtain

$$p_r^{n+1} - p_r^n \approx \Delta t a(r, t^n)[p(r, t^n) - p(r - \alpha, t^n)].$$

The value of $p(r - \alpha, t^n)$ is obtained by linear interpolation, and is given by

$$p(r - \alpha, t^n) = \alpha p_{r-1}^n - (\alpha - 1)p_r^n.$$

Hence, the approximation for the boundary condition is given by

$$P_N^{n+1} = p_N^n + \alpha \Delta t a_N^n [p_N^n - p_{N-1}^n]. \tag{2.9}$$

4 Stability and Convergence

In this section, we study the stability and convergence of the developed scheme for the problem (2.1) and (2.3). The numerical approximation of Eqs. (2.1) and (2.3) is given by

$$\bar{p}_j^n = p_j^n + \Delta t,\ S(\bar{p}_j^n). \tag{2.10}$$

$$p_j^{n+1} = \bar{p}_j^n - \frac{\Delta t}{\Delta v}\left[F(\bar{p}_{j+1/2}^{n-}, \bar{p}_{j+1/2}^{n+}) - F(\bar{p}_{j-1/2}^{n-}, \bar{p}_{j-1/2}^{n+})\right]. \tag{2.11}$$

Proposition 4.1. Under the CFL condition [132],

$$\frac{\Delta t}{\Delta v} \max_{w_1, w_2} \{|H(u, w_1) - H(v, w_1)| + |H(w_2, u) - H(w_2, v)|\} \leq |u - v|\ \forall u, v \in \mathbb{M}, \tag{2.12}$$

where

$$\mathbb{M} = \{g \in L^\infty(R), \|g\|_{L^\infty(R)} \leq \|p^0\|_{L^\infty(R)}\}.$$

The numerical approximation given by Eqs. (2.7) and (2.8) satisfy the following inequality:

(i) $\|p^{n+1}\|_{L^\infty(\mathbb{Z})} \leq e^{\mu T}\|p_0^n\|_{L^\infty(\mathbb{Z})}$,

(ii) $TV(p^{n+1}) \leq e^{\mu T} TV(p^0)$.

Proof.

$$p_j^{n+1} = \bar{p}_j^n - \frac{\Delta t}{\Delta v}\left[F(\bar{p}_{j+1/2}^{n-}, \bar{p}_{j+1/2}^{n+}) - F(\bar{p}_{j-1/2}^{n-}, \bar{p}_{j-1/2}^{n+})\right].$$

$$= \bar{p}_j^n - \frac{\Delta t}{\Delta v}[F(\bar{p}_{j+1/2}^{n-}, \bar{p}_{j+1/2}^{n+}) - F(\bar{p}_{j-1/2}^{n-}, \bar{p}_{j+1/2}^{n\,+}) + F(\bar{p}_{j-1/2}^{n-}, \bar{p}_{j+1/2}^{n\,+}) - F(\bar{p}_{j-1/2}^{n-}, \bar{p}_{j-1/2}^{n+})].$$

Using mean value linearization of the numerical flux, we obtain

$$p_j^{n+1} = \bar{p}_j^n - \frac{\Delta t}{\Delta v}\frac{\partial F}{\partial u}(\tilde{u}, \bar{p}_{j+1/2}^{n+})\left(\bar{p}_{j+1/2}^{n-} - \bar{p}_{j-1/2}^{n-}\right) - \frac{\Delta t}{\Delta v}\frac{\partial F}{\partial v}(\bar{p}_{j-1/2}^{n-}, \tilde{v})\left(\bar{p}_{j+1/2}^{n+} - \bar{p}_{j-1/2}^{n+}\right), \tag{2.13}$$

where

$$\bar{p}_{j-1/2}^{-} < \tilde{u} < \bar{p}_{j+1/2}^{-}, \quad \bar{p}_{j-1/2}^{+} < \tilde{v} < \bar{p}_{j+1/2}^{+}.$$

Now

$$\bar{p}_{j+1/2}^{n-} - \bar{p}_{j-1/2}^{n-} = \left[1 + \frac{1+k}{4}\left(\phi(Z_j^n) - \frac{\phi(Z_{j+1}^n)}{Z_{j+1}^n}\right) + \frac{1-k}{4}\left(\phi\left(\frac{1}{Z_j^n}\right)Z_j^n - \phi\left(\frac{1}{Z_{j-1}^n}\right)\right)\right]$$

$$\times \Delta\bar{p}_{j-1/2}^n, \tag{2.14}$$

$$\bar{p}_{j+1/2}^{n+} - \bar{p}_{j-1/2}^{n+} = \left[1 - \frac{1+k}{4}\left(\phi\left(\frac{1}{Z_{j+1}^n}\right)Z_{j+1}^n - \phi\left(\frac{1}{Z_j^n}\right)\right) - \frac{1-k}{4}\left(\phi(Z_{j+1}^n) - \frac{\phi(Z_j^n)}{Z_j^n}\right)\right]$$

$$\times \Delta\bar{p}_{j+1/2}^n. \tag{2.15}$$

By using the condition given by Remark (3.2), we conclude that

$$\bar{p}_{j+1/2}^{n-} - \bar{p}_{j-1/2}^{n-} \geq 0, \quad \bar{p}_{j+1/2}^{n+} - \bar{p}_{j-1/2}^{n+} \geq 0.$$

Also,

$$\frac{\Delta t}{\Delta v}\frac{\partial F}{\partial u}(\tilde{u}, \bar{p}_{j+1/2}^{n+})\left(\bar{p}_{j+1/2}^{n-} - \bar{p}_{j-1/2}^{n-}\right) \geq 0, \text{ as given } \frac{\Delta t}{\Delta v}\frac{\partial F}{\partial u}(\tilde{u}, \bar{p}_{j+1/2}^{n+}) \geq 0.$$

$$-\frac{\Delta t}{\Delta v}\frac{\partial F}{\partial v}(\bar{p}_{j-1/2}^{n-}, \tilde{v})\left(\bar{p}_{j+1/2}^{n+} - \bar{p}_{j-1/2}^{n+}\right) \geq 0 \text{ since } -\frac{\Delta t}{\Delta v}\frac{\partial F}{\partial v}(\bar{p}_{j-1/2}^{n+}, \tilde{u}) \geq 0.$$

Thus

$$D_{j-1/2}^n = \frac{\frac{\Delta t}{\Delta v}\frac{\partial F}{\partial u}(\tilde{u}, \bar{p}_{j+1/2}^{n+})\left(\bar{p}_{j+1/2}^{n-} - \bar{p}_{j-1/2}^{n-}\right)}{\Delta\bar{p}_{j+1/2}^n} \geq 0,$$

$$C_{j+1/2}^n = \frac{-\frac{\Delta t}{\Delta v}\frac{\partial F}{\partial v}(\bar{p}_{j-1/2}^{n-}, \tilde{v})\left(\bar{p}_{j+1/2}^{n+} - \bar{p}_{j-1/2}^{n+}\right)}{\Delta\bar{p}_{j-1/2}^n} \geq 0.$$

From the Remark (3.2), we have $C_{j+1/2}^n + D_{j+1/2}^n \leq 1$. From Eq. (2.13), one obtains

$$p_j^{n+1} = \bar{p}_j^n - D_{j-1/2}^n\Delta\bar{p}_{j+1/2}^n + C_{j+1/2}^n\Delta\bar{p}_{j-1/2}^n,$$

$$p_j^{n+1} = \bar{p}_j^n + C_{j+1/2}^n\Delta\bar{p}_{j-1/2}^n - D_{j-1/2}^n\Delta\bar{p}_{j+1/2}^n.$$

This is incremental form which shows that the MUSCL scheme is TVD. We have

$$\|p^{n+1}\|_{L^\infty(z)} \leq \|\bar{p}^n\|_{L^\infty(z)},$$
$$\text{and} \qquad TV(p^{n+1}) \leq TV(\bar{p}^n).$$

$$\text{Now,} \qquad \bar{p}_j^n = p_j^n + \Delta t S(\bar{p}_j^n),$$
$$|\bar{p}_j^n| = |p_j^n + \Delta t S(\bar{p}_j^n)| \leq |p_j^n| + \Delta t |S(\bar{p}_j^n)| \leq |p_j^n| + k\Delta t |\bar{p}_j^n|,$$
$$|(1 - k\Delta t)||\bar{p}_j^n| \leq |p_j^n|,$$
$$\text{Thus,} \qquad |\bar{p}_j^n| \leq \frac{1}{(1 - k\Delta t)} |p_j^n|.$$

Under the condition $k\Delta t < 1$, using $\mu = \frac{k}{(1-k\Delta t)} > 0$, we obtain

$$|\bar{p}_j^n| \leq (1 + \mu\Delta t)|p_j^n| \implies \|\bar{p}_j^n\|_{L^\infty(\mathbb{Z})} \leq (1 + \mu\Delta t)\|p_j^n\|_{L^\infty(\mathbb{Z})} \leq e^{n\mu\Delta t}\|p_0^n\|_{L^\infty(\mathbb{Z})}.$$
$$\text{Hence,} \qquad \|p^{n+1}\|_{L^\infty(\mathbb{Z})} \leq e^{\mu T}\|p_0^n\|_{L^\infty(\mathbb{Z})},$$
$$\text{and} \qquad TV(p^{n+1}) \leq e^{\mu T} TV(p^0).$$

Proposition 4.2. *(Existence of the solution of the developed scheme)* If $p^0 \in L^\infty(\mathbb{Z})$, the scheme (2.8) admits a unique solution $p^{n+1} \in L^\infty(\mathbb{Z})$.

Proof. Consider the function

$$\theta(x) = x - \Delta t S(x),\ \theta'(x) = 1 - \Delta t S'(x) > 0 \qquad (\because \quad S' \leq 0).$$

Therefore, $\theta(x)$ is differentiable and strictly monotonic. Hence the scheme

$$p_j^{n+1} = \bar{p}_j^n - \frac{\Delta t}{\Delta v}\left[F(\bar{p}_{j+1/2}^{n-}, \bar{p}_{j+1/2}^{n+}) - F(\bar{p}_{j-1/2}^{n-}, \bar{p}_{j-1/2}^{n+})\right],$$

admits a unique solution and $p^{n+1} \in L^\infty(\mathbb{Z})$, since $\|p^{n+1}\|_{L^\infty(\mathbb{Z})} \leq e^{kT}\|p_0^n\|_{L^\infty(\mathbb{Z})}$.

Remark 4.1. We now prove BV (Bounded Variation) stability in space. According to Chalabi [127] this is a sufficient condition for BV in time and space.

Theorem 4.1. *If the initial solution $p_0 \in L^\infty(\mathbb{R}) \cap L^1(\mathbb{R})$, flux function $f \in C^1(\mathbb{R})$ and source term $S \in C^1(\mathbb{R})$ such that $S(0) = 0$ and $S' \leq k$, then under the CFL condition (2.12), the approximate solution $p_{\Delta v}$ converges in $L^1_{loc}(\mathbb{R} \times (0,T))$ towards the entropy solution p of Eqs. (2.1) and (2.3) as mesh size Δv tends to zero.*

Proof. By Proposition (2.4.1) the approximate solution $p_{\Delta v}$ is bounded in $L^\infty(\mathbb{R}) \cap L^1(\mathbb{R} \cap BV(R \times (0,T))$, then by Helly's theorem we can extract a subsequence of $p_{\Delta v}$ which converges to p in $L^1_{loc}(\mathbb{R} \times (0,T))$.

Further, we show that p satisfies the entropy condition. As to do, write Eqs. (2.10) and

(2.11) in the following form

$$p_j^{n+1} = \bar{p}_j^n - \frac{\Delta t}{\Delta v}\left[F(\bar{p}_j^n, \bar{p}_{j+1}^n) - F(\bar{p}_{j-1}^n, \bar{p}_j^n)\right], \tag{2.16}$$

and

$$p_j^{n+1} = p_j^n - \frac{\Delta t}{\Delta v}\left[\Big(F(p_{j+1/2}^{n-}, p_{j+1/2}^{n+}) - F(p_j^n, p_{j+1}^n)\Big) - \Big(F(p_{j-1/2}^{n-}, p_{j-1/2}^{n+}) - F(p_{j-1}^n, p_j^n)\Big)\right] + \Delta t S(\bar{p}_j^n). \tag{2.17}$$

Since the scheme (2.16) is monotone under the CFL condition (2.12) then by the result of Tadmor [133], $\exists$ a numerical entropy flux G associated entropy function η such that

$$\eta(p_j^{n+1}) - \eta(\bar{p}_j^n) + \frac{\Delta t}{\Delta v}\left[G(\bar{p}_j^n, \bar{p}_{j+1}^n) - G(\bar{p}_{j-1}^n, \bar{p}_j^n)\right] \leq 0.$$

Using convexity of η, we get

$$\eta(p_j^{n+1}) - \eta(p_j^n) + \frac{\Delta t}{\Delta v}\left[G(\bar{p}_j^n, \bar{p}_{j+1}^n) - G(\bar{p}_{j-1}^n, \bar{p}_j^n)\right] \leq \eta'(\bar{p}_j^n)(p_j^{n+1} - \bar{p}_j^n),$$

$$\eta(p_j^{n+1}) - \eta(p_j^n) + \frac{\Delta t}{\Delta v}\left[G(\bar{p}_j^n, \bar{p}_{j+1}^n) - G(\bar{p}_{j-1}^n, \bar{p}_j^n)\right] \leq \eta'(\bar{p}_j^n) S(\bar{p}_j^n)\Delta t.$$

Multiplying by $\psi_j^n \Delta v$ on both side and adding over j and n.

$$\sum_{j,n} \Delta v\left[\eta(p_j^{n+1}) - \eta(p_j^n)\right]\psi_j^n + \sum_{j,n}\Delta t\left[G(\bar{p}_j^n, \bar{p}_{j+1}^n) - G(\bar{p}_{j-1}^n, \bar{p}_j^n)\right]\psi_j^n,$$

$$\leq \sum_{j,n} \eta'(\bar{p}_j^n) S(\bar{p}_j^n)\psi_j^n \Delta t \Delta v. \tag{2.18}$$

Using discrete integration by parts on the L.H.S of Eq. (2.18)

$$A = -\sum_{j,n} \Delta v\ \Delta t\ \eta(p_j^{n+1})\ \frac{(\psi_j^{n+1} - \psi_j^n)}{\Delta t} - \sum_{j,n}\Delta t\ \Delta v\ G(\bar{p}_j^n, \bar{p}_{j+1}^n)\ \frac{(\psi_{j+1}^n - \psi_j^n)}{\Delta v}.$$

Hence,

$$A = -\int_{\mathbb{R}}\int_{\mathbb{R}^+} \left[\eta(p_{\Delta v})(\psi_{\Delta v})_t + G_{\Delta v}(v,t)(\psi_{\Delta v})_v\right]\ dvdt,$$

where, $G_{\Delta v}(v,t) = G(\bar{p}_j^n, \bar{p}_{j+1}^n)$, $(v,t) \in (v_{j-1/2}, v_{j+1/2}) \times (n\Delta t, (n+1)\Delta t)$. By using Lebesgue Theorem, and obtain

$$\int_{\mathbb{R}}\int_{\mathbb{R}^+} \left[\eta(p_{\Delta v})(\psi_{\Delta v})_t + G_{\Delta v}(v,t)(\psi_{\Delta v})_v\right]\ dvdt \longrightarrow \int_{\mathbb{R}}\int_{\mathbb{R}^+} \left[\eta(p)\psi_t + G(p)\psi_v\right] dvdt. \tag{2.19}$$

Take the R.H.S of Eq. (2.18)

$$\sum_{j,n} \eta'(\bar{p}_j^n) S(\bar{p}_j^n)\psi_j^n \Delta t \Delta v. = \int_{\mathbb{R}}\int_{\mathbb{R}^+} \eta'(p) S(p)\psi dvdt. \tag{2.20}$$

Using Eqs. (2.19)-(2.20) in (2.15)

$$\int_{\mathbb{R}}\int_{\mathbb{R}^+} [\eta(p)\psi_t + G(p)\psi_v]\, dvdt \geq \int_{\mathbb{R}}\int_{\mathbb{R}^+} \eta'(p)S(p)\psi dvdt.$$

Thus, the limit p is the weak solution which satisfies the entropy condition. Note that the entropy solution is the unique solution. Hence the numerical approximation $p_{\Delta v}$ converges towards the entropy solution p as $\Delta v \to 0$.

5 Numerical Experiments

In this section, we present some numerical examples to show the performance of developed scheme. We do not have the exact solution of given problem (2.1), nevertheless we will use the conventional approach for estimating the convergence rate [134].

Consider a method of order q in some norm. Let $\tilde{p}(h)$ be the approximation to the exact solution with grid size h. Thus,

$$\tilde{p}(h) = p_{exact} + Ch^q + o(h^q),\ C \text{ is a constant.}$$

Let h^* be the finest grid used for this method, then on a coarser grid with the step size h, we have

$$\frac{\tilde{p}(h) - \tilde{p}(h^*)}{\tilde{p}(\frac{h}{2}) - \tilde{p}(h^*)} \approx 2^q \frac{1 - (\frac{h^*}{h})^q}{1 - (\frac{2h^*}{h})^q}. \tag{2.21}$$

From the Eq. (2.21) we can compute the order of accuracy. Suppose we double the number of grid points successively, i.e.

$$\frac{h^*}{h} = 2^{-k},\ k = 1, 2, 3, \cdots .$$

Then we get

$$\frac{\tilde{p}(h) - \tilde{p}(h^*)}{\tilde{p}(\frac{h}{2}) - \tilde{p}(h^*)} = \frac{2^q(1 - 2^{-kq})}{1 - 2^{q(1-k)}}. \tag{2.22}$$

For a first-order method, i.e. $q = 1$, we have

$$\frac{\tilde{p}(h) - \tilde{p}(h^*)}{\tilde{p}(\frac{h}{2}) - \tilde{p}(h^*)} = \frac{2(1 - 2^{-k})}{1 - 2^{(1-k)}} = \frac{2^k - 1}{2^{(k-1)} - 1},$$

for k=2, 3, 4,$\cdots$, the ratios are 3, 2.33, 2.1429$\cdots$.

For a second order method i.e. $q = 2$, we have

$$\frac{\tilde{p}(h) - \tilde{p}(h^*)}{\tilde{p}(\frac{h}{2}) - \tilde{p}(h^*)} = \frac{4(1 - 4^{-k})}{1 - 4^{(1-k)}},$$

for k=2, 3, 4, $\cdots$, the ratios are 5, 4.2, 4.0476$\cdots$.

For a third order method i.e. $q = 3$, we have

$$\frac{\tilde{p}(h) - \tilde{p}(h^*)}{\tilde{p}(\frac{h}{2}) - \tilde{p}(h^*)} = \frac{8(1 - 8^{-k})}{1 - 8^{(1-k)}},$$

for k=2, 3, 4,$\cdots$, the ratios are 9, 8.111, 8.01369 $\cdots$.

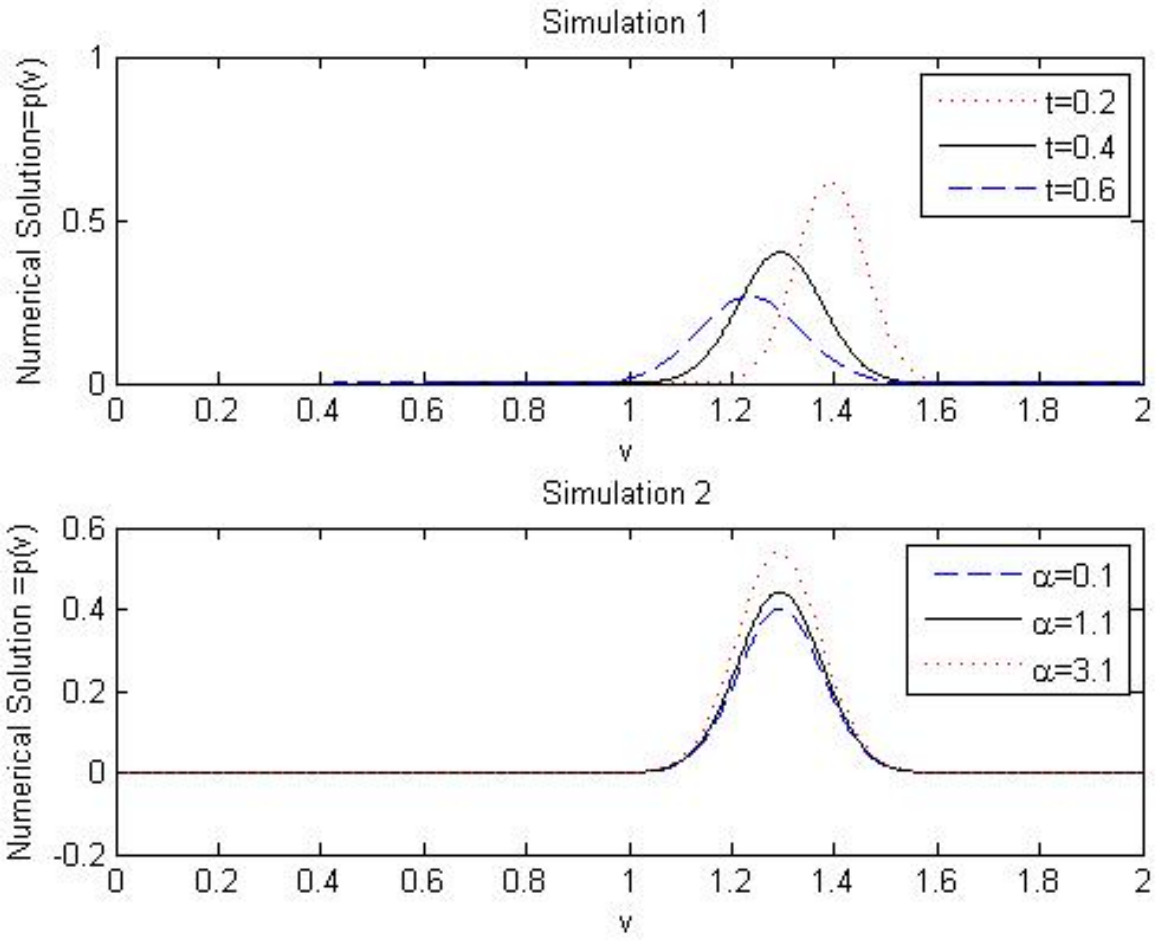

Figure 2.1: Numerical solution $p(v,t)$ of Example 1.

Example 1. Consider Eqs. (2.1)-(2.2) with the following coefficients

$$\tau = 1, \quad a(v,t) = -\frac{1+v^2}{1+2vt+2v^2+v^4}, \quad r = 2,$$
$$b(v,t) = \frac{1}{1+2vt+v^4t^4}, \quad RI(t) = 1+\cos 2t.$$

Initial condition

$$p(v,0) = e^{-10(4v-6)^2}.$$

Boundary conditions

$$p(v,t) = 0, \quad v \in [-\alpha, 0],$$
$$\frac{\partial p(r,t)}{\partial t} = a(r,t)\ [p(r,t) - p(r-\alpha,t)],\ p(v,t) = 0,\ v \in (r, r+\beta].$$

From Fig. 2.1 we see that the developed scheme is valid for higher value of delay argument α, however the scheme in [122, 135] is not valid as the delay term is increased. We also notice that as time increases, the graph of impulse moves from right to left and its height decrease gradually.

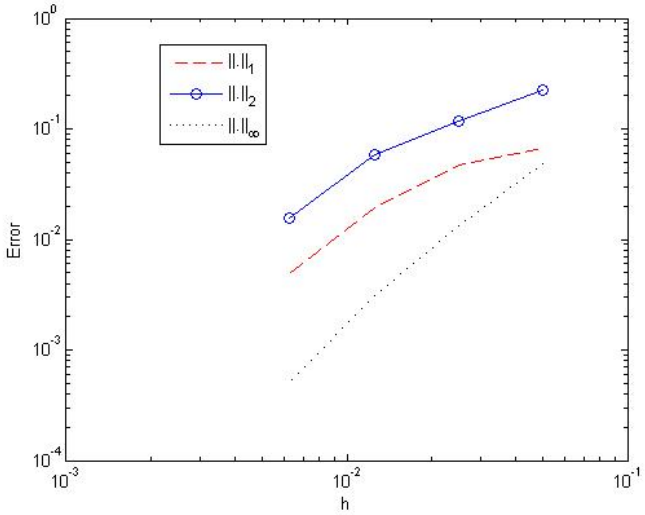

Figure 2.2: Error-norm for numerical solution $p(v,t)$ of Example 1.

Next step is to compute the errors of the computed numerical solution p at time $t = 0.5$

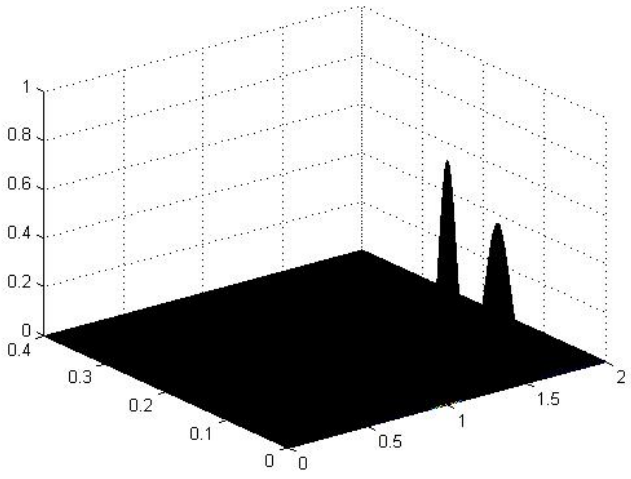

Figure 2.3: Numerical solution $p(v,t)$ in 3D for Example 1 at time $t = 0.4$ and $t = 0.6$ with $\Delta t = 0.001$ and $N = 1000$.

by using the higher order MUSCL scheme. The errors are computed in $\|.\|_1,\ \|.\|_2,\ \|.\|_\infty$

norms which are defined as follows

$$\|.\|_1 = \Delta v \sum_i |(p_{\Delta v})_i - (p^*)_i|, \qquad \|.\|_2 = \sqrt{\Delta v \sum_i |(p_{\Delta v})_i - (p^*)_i|^2},$$
$$\|.\|_\infty = \max |(p_{\Delta v}) - (p^*)|,$$

where p^* is the numerical solution at finest grid.

N	$\|.\|_1$	r_1	$\|.\|_2$	r_2	$\|.\|_\infty$	r_3
20	$6.76e-02$	–	$2.231e-01$	–	$4.85e-02$	–
40	$4.76e-02$	1.42	$1.160e-01$	1.92	$1.32e-02$	3.67
80	$1.92e-02$	2.47	$5.77e-02$	2.01	$3.1e-03$	4.25
160	$4.90e-03$	3.91	$1.54e-02$	3.74	$5.120e-04$	6.05

Table 2.1: Error Table for Example 1.

From Table 2.1, we conclude that the developed scheme is second-order accurate for the given problem. We also plotted the error norms (see Fig. 2.2).
In Fig. 2.3, we have shown the numerical solution by a 3D graph. From this figure (Fig. 2.3), we observe that as time increases the height of impulse decreases.

Example 2. Consider Eqs. (2.1)-(2.2) with the following coefficients

$$\tau = 1, \quad a(v,t) = \frac{1}{1+vt+v^3}, \quad r = 2,$$
$$b(v,t) = \frac{1+vt}{1+vt+v^4t^4}, \quad RI(t) = \sin t + \cos 2t.$$

Initial condition

$$p(v,0) = e^{-10(4v-4)^2}.$$

Boundary conditions

$$p(v,t) = 0, \quad v \in [-\alpha, 0],$$
$$\frac{\partial p(r,t)}{\partial t} = a(r,t)\ [p(r,t) - p(r-\alpha,t)],\ p(v,t) = 0,\ v \in (r, r+\beta].$$

From Fig. 2.4, we observe that at time $t = 0$, the impulse will be at threshold level and after that the size of the impulse is decreasing gradually as time increases. We easily conclude from Figure 2.4 that the developed scheme is also valid for the higher value of advance argument β.

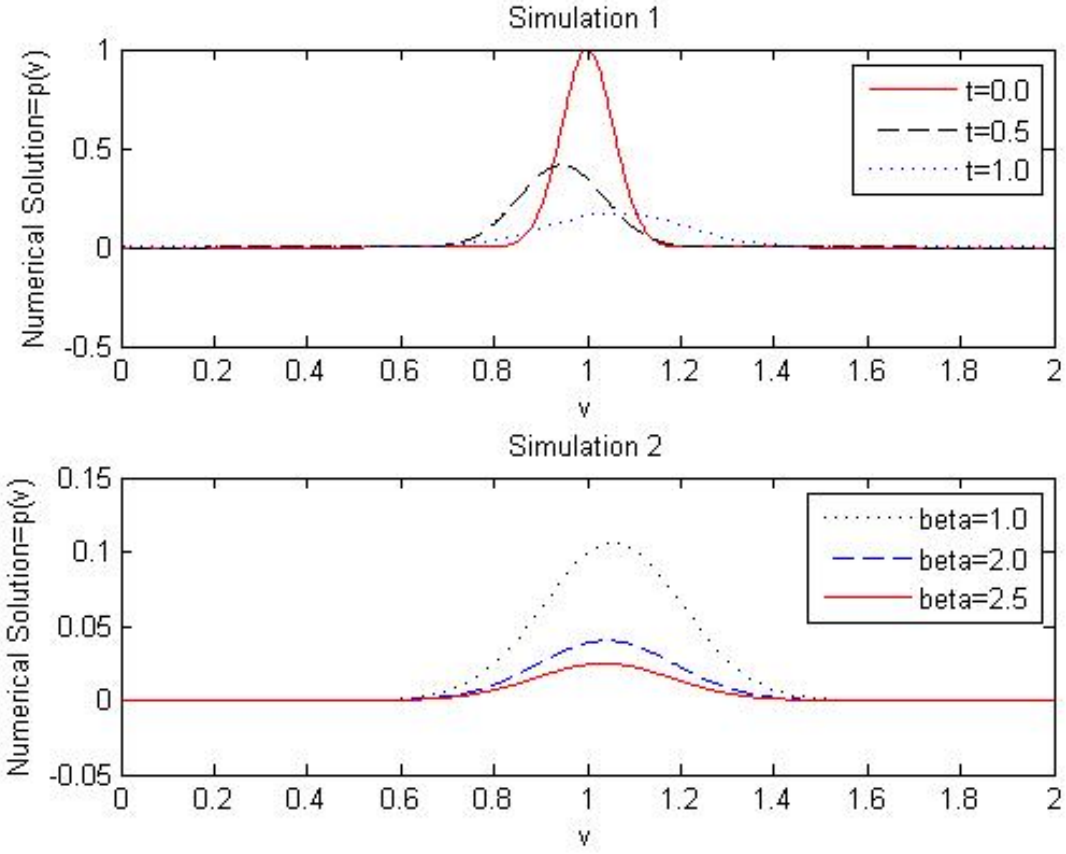

Figure 2.4: Numerical solution $p(v,t)$ of Example 2.

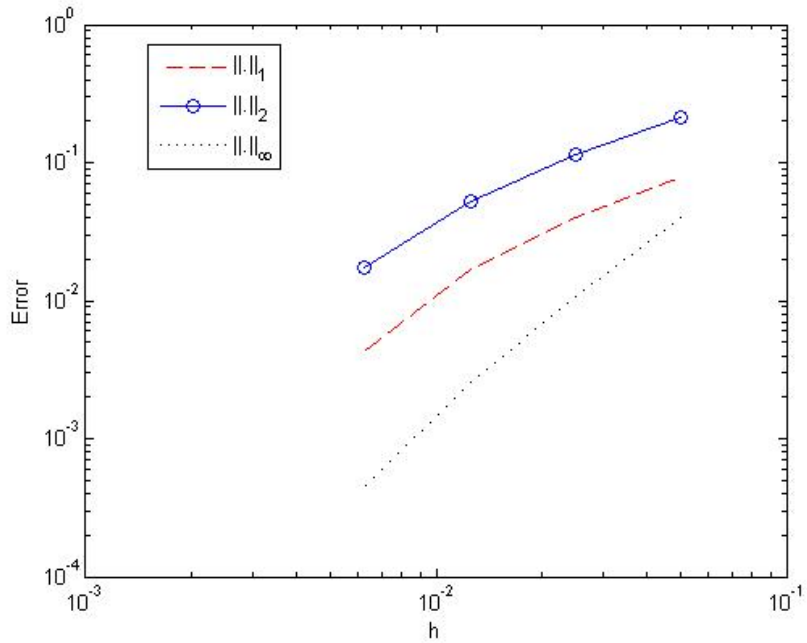

Figure 2.5: Error-norms for numerical solution $p(v,t)$ of Example 2.

N	$\|\|.\|\|_1$	r_1	$\|\|.\|\|_2$	r_2	$\|\|.\|\|_\infty$	r_3
20	$7.92e-02$	–	$2.106e-01$	–	$3.97e-02$	–
40	$4.04e-02$	1.96	$1.120e-01$	1.88	$1.07e-02$	3.71
80	$1.67e-02$	2.41	$4.990e-02$	2.24	$2.6e-03$	4.11
160	$4.30e-03$	3.88	$1.360e-02$	3.66	$4.43e-04$	5.86

Table 2.2: Error Table for Example 2

We have plotted the error-norms (see Fig. 2.5). We can also see the visualization of Example 2 in 3D (see Fig. 2.6). From Fig. 2.6, we see that the size of impulse approaches toward the threshold level at initial time.

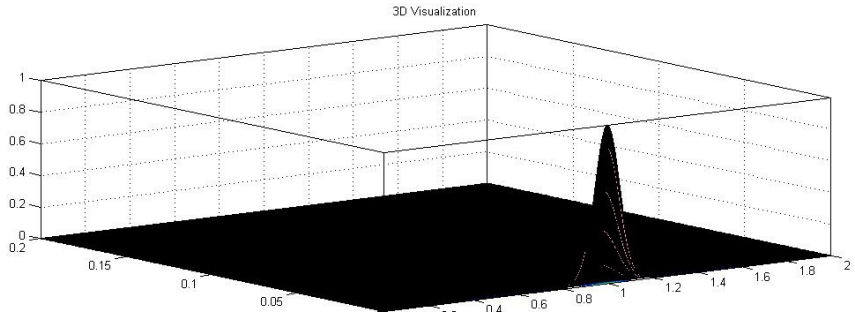

Figure 2.6: Numerical solution $p(v,t)$ of Example 2 in 3D at time $t = 0.0$ & $N = 1000$.

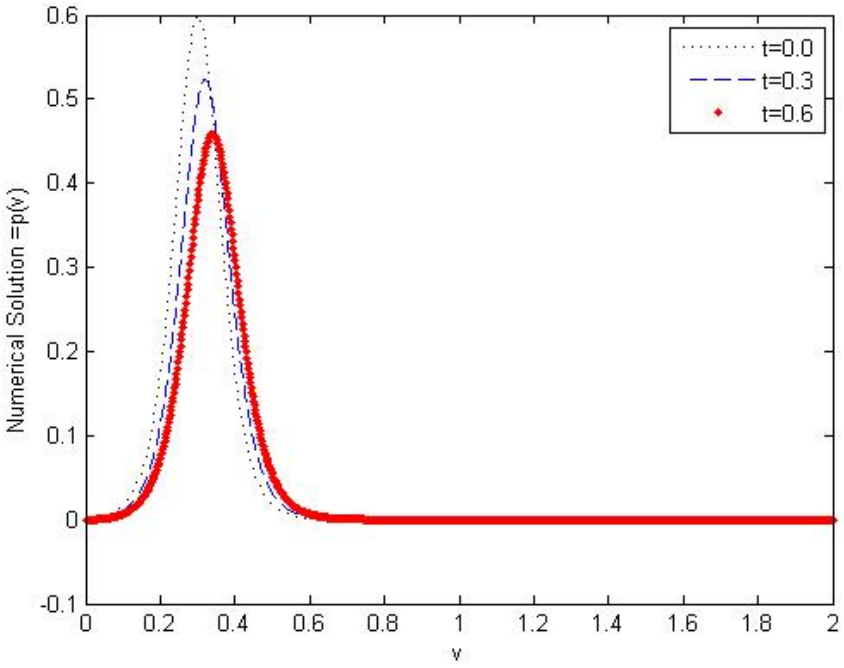

Figure 2.7: Numerical solution $p(v,t)$ of Example 3.

Example 3. Consider Eqs. (2.1)-(2.2) with the following coefficients

$$\tau = 1, \quad a(v,t) = \frac{1+t}{1+2v+t^2}, \alpha = 0.5, \beta = 0.5, \quad r = 2,$$
$$b(v,t) = \frac{1+vt}{1+2t+3t^2}, \quad RI(t) = \sin t(1-\cos t).$$

Initial condition

$$p(v,0) = g\sec h^2(l(v-v_0)), \quad v_0 = 0.4, \quad l = \frac{1}{2\sqrt{2}}\sqrt{\frac{g}{d}}, \quad d = 0.0005, \quad g = 0.6.$$

Boundary conditions

$$p(v,t) = 0, \quad v \in [-\alpha, 0],$$
$$\frac{\partial p(r,t)}{\partial t} = a(r,t)\ [p(r,t) - p(r-\alpha,t)],\ p(v,t) = 0,\ v \in (r, r+\beta].$$

From Fig. 2.7, we conclude that as time increases, the impulse moves toward the left side. In this experiment we take the same shift arguments from previous example.

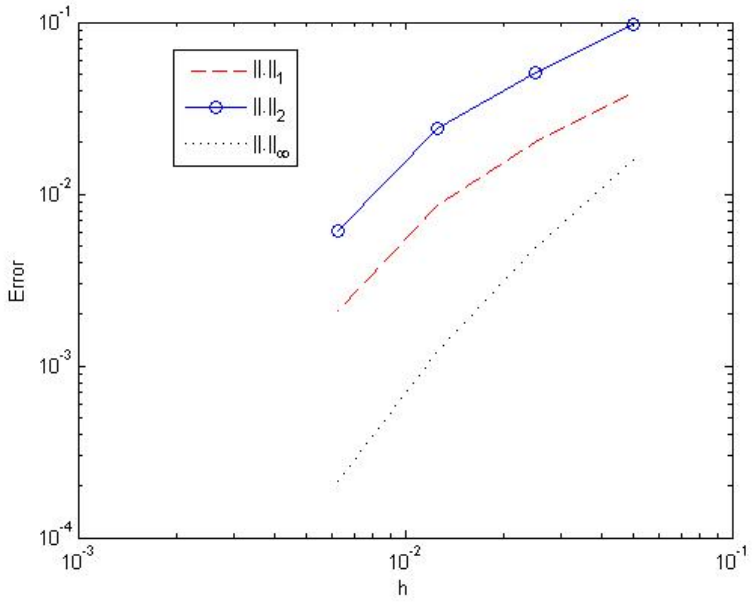

Figure 2.8: Error-norms for numerical solution $p(v,t)$ of Example 3.

Fig. 2.8 shows the error plot and Fig. 2.9 shows the envision of the Example 3 in 3D.

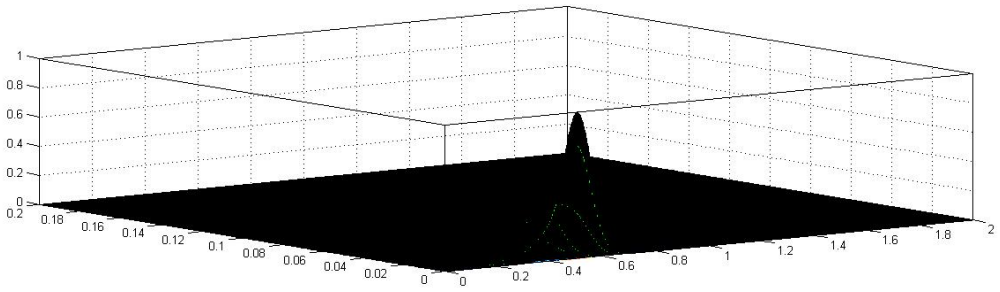

Figure 2.9: Numerical solution $p(v,t)$ of Example 2 in 3D at time $t = 0.6$ & $N = 1000$.

Table 2.3: Error Table for Example 3

N	$\|.\|_1$	r_1	$\|.\|_2$	r_2	$\|.\|_\infty$	r_3
20	$3.89e-02$	–	$9.64e-02$	–	$1.56e-02$	–
40	$1.99e-02$	1.95	$5.13e-02$	1.87	$4.90e-03$	3.18
80	$8.60e-03$	2.31	$2.42e-02$	2.11	$1.20e-03$	4.08
160	$2.10e-03$	4.09	$6.10e-03$	3.96	$2.11e-04$	5.69

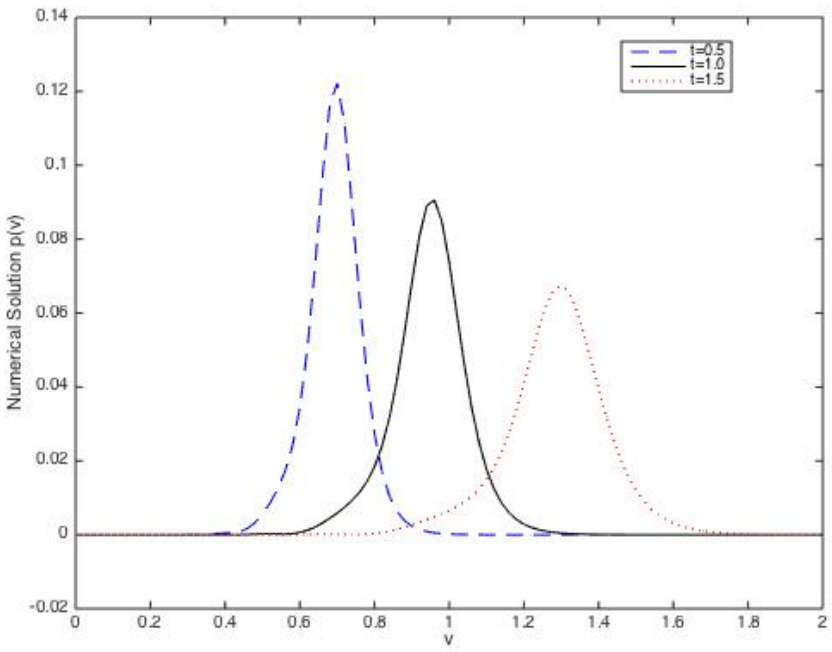

Figure 2.10: Numerical solution $p(v,t)$ of Example 4.

Example 4. Consider the Eqs. (2.1)-(2.2) with the following coefficients

$$\tau = 1, \quad a(v,t) = -\frac{1+v^2}{1+2vt+2v^2+t^4}, \ \alpha = 0.0001, \ \beta = 0.0001, \ r = 2,$$

$$b(v,t) = \frac{1}{1+2vt+v^4t^4}.$$

In this example, we take $RI(t) = I_0 + AN(t)$ and we take $I_0 = A = 1$, for numerical computations.

$$N(t) = \int_{-\infty}^{r} \gamma(v)p(v,t)dv.$$

We also take $\gamma(v) = 1$.
Initial condition

$$p(v,0) = 2g\,\mathrm{sec}\,h^2(3l(v-v_0)), \quad v_0 = 0.4, \qquad l = \frac{1}{2\sqrt{2}}\sqrt{\frac{g}{d}}, \quad d = 0.0005, \quad g = 0.1.$$

Boundary conditions

$$p(v,t) = 0, \quad v \in [-\alpha, 0],$$
$$\frac{\partial p(r,t)}{\partial t} = a(r,t)\ [p(r,t) - p(r-\alpha,t)],\ p(v,t) = 0,\ v \in (r, r+\beta].$$

From Fig. 2.10, we see the particular case when the impulse hits the threshold level, the impulse instantaneously increases at the moment, and after that as time increases the impulse size decreases and this process continues.

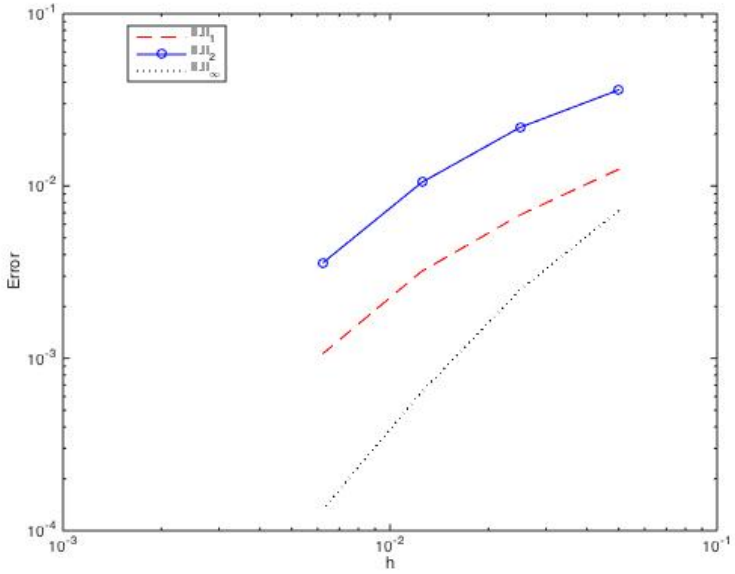

Figure 2.11: Error-norm for numerical solution $p(v,t)$ of Experiment 4.

Errors are plotted (see Fig. 2.11) and the picturization of the Experiment 4 is shown in 3D (see Fig. 2.12).

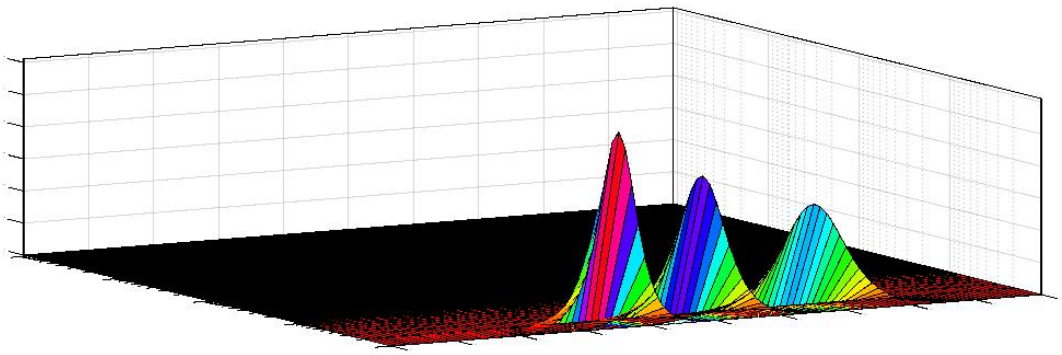

Figure 2.12: Numerical solution $p(v,t)$ in 3D at different time levels $t = 0.5,\ 1.0,\ 1.5$ & $N = 100$.

N	$\|\|.\|\|_1$	r_1	$\|\|.\|\|_2$	r_2	$\|\|.\|\|_\infty$	r_3
20	$1.25e-02$	–	$3.61e-02$	–	$7.20e-03$	–
40	$6.80e-03$	1.83	$2.19e-02$	1.64	$2.50e-03$	2.80
80	$3.20e-03$	2.12	$1.05e-02$	2.08	$6.45e-04$	3.87
160	$1.07e-03$	2.98	$3.60e-03$	2.91	$1.34e-04$	4.81

Table 2.4: Error Table for Example 4

6 Summary

We have presented a higher order MUSCL scheme for the neuronal model with mixed boundary conditions. The importance of this scheme is that it is valid for larger values of advance and delay argument, which can be seen in the numerical experiments. The stability and convergence of the present scheme are also discussed. The order of convergence of the developed scheme is obtained theoretically and verified numerically. The effect of point-wise delay with advance on the solution behavior is shown by taking some test examples.

Chapter 3

A Numerical Treatment of a Population Density Model Based on Quadratic-Integrate-And-Fire Neuron [2]

The previous chapter discussed Stein's model based on leaky-integrate-and-fire neuron and presented a high-order numerical scheme to find the approximate solution of the governing equation. This chapter introduces a population density model based on quadratic-integrate-and-fire neuron. This model (quadratic integrate-and-fire neuron) is used for the derivation of governing equation by using the population density approach. WENO (weighted essentially non-oscillatory) finite volume method together with RK (Runge-Kutta) method is applied to find the approximate solution of governing equation. The proposed scheme is compared with second and third-order existing schemes in the literature for the same type of model equation. Numerical results depict that the proposed algorithm is more efficient and produce accurate solutions with less number of grid cells. In addition to this, a discontinuity is added in the application of model equation to illustrate the good performance of the proposed scheme.

1 Introduction

It is well known that the size of presynaptic neuronal firings decides the next behavior of a neuron. In the complex neuronal networks, the variability in neuronal firings has been observed even the external stimuli are held constant or without any apparent external stimulus. The possible reason is that a large number of synapses and different types of synaptic inputs exist in neural network. In the mid of twentieth century, Stein introduced a model about theoretical study of neuronal variability. The model is basically based on the five assumptions and the theory of Hodgkin-Huxley (HH) model [17]. In addition to this, Stein also discussed the distribution of neuronal firing intervals, neuronal firing rate, and strength-duration curves. In 1979, Tuckwell modified the Stein's model and

[2] Santosh Kumar et al., *"High-Order Finite Volume Approximation for Population Density Model Based on Quadratic Integrate-and-fire neuron"*, Engineering Computations, Emerald. [Under Review]

discussed the behavior of neuronal activity in quantitative terms [27]. He concluded that the variation in inter-spike interval (times between subsequent spikes of a neuron) greater than one is due to the strong inhibition. A number of authors ([9, 28, 136–141]) have subsequently studied this model with different applications in modeling of neural variability. Some authors have implemented this model numerically with different forms. In 2004, Kadalbajoo and Sharma [120] introduced a numerical scheme to discuss the determination of the expected time for generation of action potentials in nerve cells; an action potential is a transient event in which membrane potential has instant increase and then decrease. Recently, several other authors [116, 122, 142], have presented high-order numerical schemes to find the numerical solution of the above model equation. Although a number of authors have studied the dynamic properties of the neuronal networks in the past. Their studies have mainly based on leaky integrate-and-fire (LIF) neuron. More information on LIF model can be found in [14, 17, 27, 53]. Moreover, their methodology is based on probability density approach that has been widely used in biological science and specially in neuroscience.

In this chapter, we present a quadratic-integrate-and-fire (QIF) neuron based population density model for the study of neuronal system. In contrast to LIF model, QIF model does have a spike production system, which means QIF model is a spiking neuron model and is very useful for us to describe the internal behavior of neurons population. In addition, our methodology is based on population density approach, which has become very popular and efficiently used to describe the evolution of neurons population. The following procedure [71], is used to derive population density model equation. Next, we obtain the population density model equation using QIF neuron model.

The QIF neuron model was introduced by Latham et al. in [38]. This model consists of an ordinary differential equation (ODE) that describes the time evolution of membrane potential, and a reset mechanism. The interested reader is referred to review-articles [10, 39, 143–145] for details. Let us consider QIF model with some modifications,

$$\begin{cases} \tau \dfrac{dv}{dt} = (v - V_{\text{rest}})(v - V_{\text{thresh}}) + I_{\text{syn}}(t) \\ \text{if } v = V_{\text{thresh}} \qquad \text{then } v = V_{\text{rest}}, \end{cases} \tag{3.1}$$

where $V_{\text{thresh}} > V_{\text{rest}}$. In Eq. (3.1), $v(t)$ denotes the neuron's membrane potential at time t, τ represents the relaxation time of the membrane potential towards the resting potential V_{rest}. Here, V_{thresh} denotes the threshold potential. The time when v hits the V_{thresh} value is considered as the time when the neuron is producing a spike and the membrane potential is instantaneously reset to V_{rest}. For $v(t) < V_{\text{thresh}}$, the membrane potential decays to the resting potential in the lack of any interaction. All the interactions

of the neuron with the network are modelled by an incoming synaptic current $I_{\text{syn}}(t)$. For $v > V_{\text{thresh}}$, the membrane potential increases so that an action potential is generated (the neuron produce a spike) and thereafter membrane potential is instantaneously reset to V_{rest}. The graphical representation of quadratic integrate-and-fire neuron is displayed in Fig. 3.1.

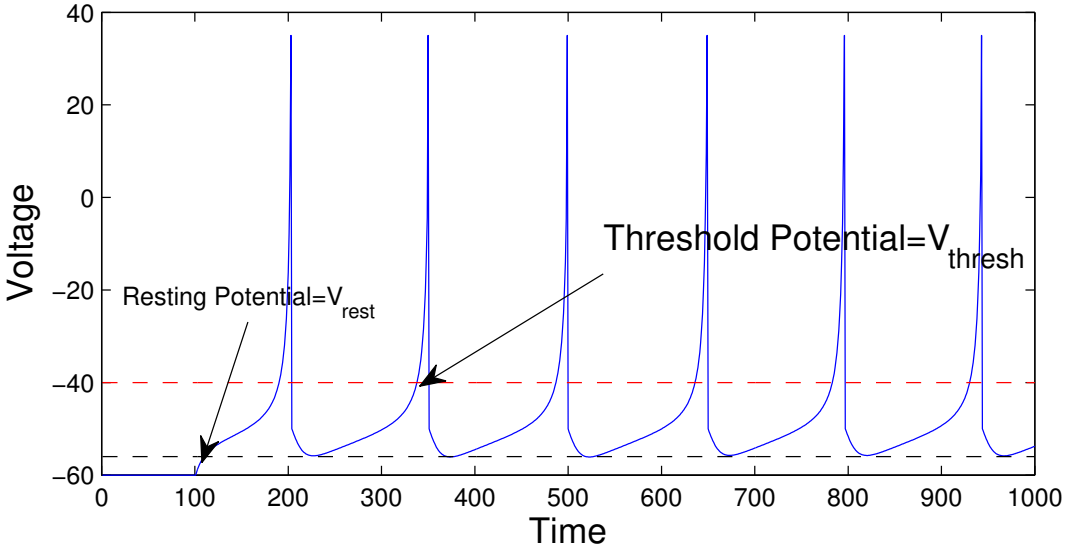

Figure 3.1: Time course of the membrane potential of quadratic integrate-and-fire neuron. Here $V_{\text{thresh}} = -40$, $V_{\text{rest}} = -56$ and consider $I_{\text{syn}}(t) = -u(t) + c, c = 70, \tau = 100$. $u(t)$ is the recovering current which satisfy $u'(t) = c_1 \left(c_2(v - V_{\text{rest}}) - u\right)$, where $c_1 = 0.03$ is the recovering time constant, $c_2 = -2$.

The interaction function, $I_{\text{syn}}(t)$ plays a key role in the dynamics of quadratic integrate-and-fire neuron model. It is engendered by the activity of pre-synaptic neurons. There are mainly two types of neurons: excitatory and inhibitory. In the structure of integrate-and-fire neuron model, each pre-synaptic impulse generates a post-synaptic current. To be more specific, assume that the pre-synaptic excitatory (inhibitory) neuron j has sent a signal at time t_j^E (t_j^I), a post-synaptic excitatory (inhibitory) neuron feels a current with time course $\delta(t - t_j^E)(\delta(t - t_j^I))$, where $\delta(.)$, the unit impulse function, represents the reaction of post-synaptic current. The total input current to the post-synaptic neuron is the sum over all incoming current impulses. Moreover, the effect of the response of a spike/current at neuron's synapse has been modeled as a jump of size α or β of the membrane potential. The jump is positive if the spike is received from the excitatory neurons and negative if it is received from the inhibitory neurons. In this way the total synaptic current is defined as

$$I_{\text{syn}}(t) = \alpha \sum_{j=1}^{\infty} \delta(t - t_j^E) - \beta \sum_{j=1}^{\infty} \delta(t - t_j^I). \tag{3.2}$$

For the dynamics of a neuron population, we derive the evolution equations for the population density function (see [70] for details). At first, we look at the population density function in any interval

$$\int_{v_1}^{v_2} F(v,t)dv = \{\text{Proportion of neurons with potential } V(t) \in [v_1, v_2] \text{ at time } t\}.$$

Then, $F(v,t)$ is the relative density of the population and satisfies

$$\int_{V_{\text{rest}}}^{V_{\text{thresh}}} F(v,t)dv = 1, \tag{3.3}$$

since the evolution equation is based on conservation of probability. This means the probability contained in any interval can change only due to the flux of probability at the end points of given interval.

Let us introduce $\mathsf{J}(v,t)$, the probability flux over v at time t, then

$$\mathsf{J}(v_1,t) - \mathsf{J}(v_2,t) = \frac{\partial}{\partial t} P_r(V(t) \in (v_1, v_2)) = \frac{\partial}{\partial t} \int_{v_1}^{v_2} F(w,t)dw.$$

Setting the above equation by using $v_2 = v$ and differentiating with respect to v, we obtain

$$\frac{\partial F}{\partial t} = -\frac{\partial \mathsf{J}}{\partial v}. \tag{3.4}$$

We now calculate the flux function based on Eqs. (3.1-3.2). For this purpose, we decompose the flux into three components: flux based on quadratic integrate-and-fire neuron, excitatory flux function based on the voltage of a neuron that jumps upward from $v-\alpha$ to v during the receiving of excitatory input, and inhibitory flux function based on the voltage of a neuron which jumps downward from $v+\beta$ to v during the receiving of inhibitory input, see Fig. 3.2. Thus, the total flux is

$$\mathsf{J}(v,t) = \overbrace{\frac{1}{\tau}\left((v - V_{\text{rest}})(v - V_{\text{thresh}})\right) F(v,t)}^{QIF} + \overbrace{p_e(t) \int_{v-\alpha}^{v} F(v,t)dv}^{excitatory} - \overbrace{p_i(t) \int_{v}^{v+\beta} F(v,t)dv}^{inhibitory}. \tag{3.5}$$

Here, p_e and p_i are the frequencies of excitatory and inhibitory input rates, respectively. The derivation related to the flux term is based on the article [56, 71]. Due to the reset mechanism, we use periodic boundary condition

$$\lim_{v \to V_{\text{rest}}} \frac{1}{\tau}(v - V_{\text{rest}})(v - V_{\text{thresh}})F(v,t) = \lim_{v \to V_{\text{thesh}}} \frac{1}{\tau}(v - V_{\text{rest}})(v - V_{\text{thresh}})F(v,t). \tag{3.6}$$

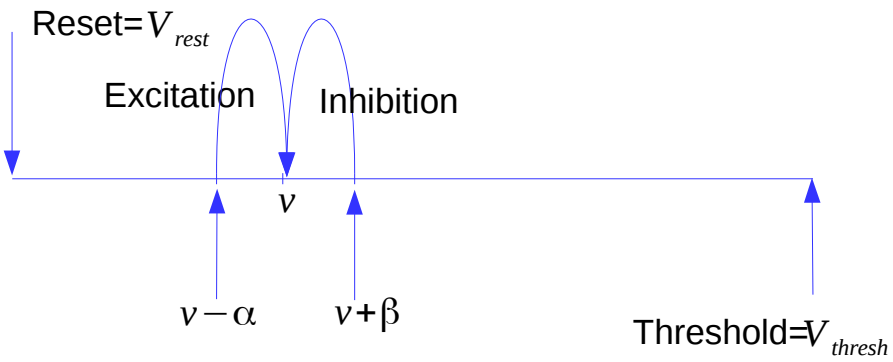

Figure 3.2: The behavior of excitatory and inhibitory neuron.

Using Eqs. (3.4)-(3.6), we have a complete model equation

$$\begin{cases} \frac{\partial F(v,t)}{\partial t} + \frac{\partial}{\partial v}\overbrace{\left[\frac{1}{\tau}\left([(v-V_{\text{rest}})(v-V_{\text{thresh}})]\right)F(v,t)\right]}^{quadratic\ integrate-and-fire} \\ \qquad = \underbrace{p_e(t)(F(v-\alpha,t)-F(v,t))}_{Excitation} + \underbrace{p_i(t)(F(v+\beta,t)-F(v,t))}_{Inhibition}, \\ \qquad\qquad (v,t) \in (V_{\text{rest}}, V_{\text{thresh}}) \times (0, T_{\max}), \\ \lim_{v\to V_{\text{rest}}} \frac{1}{\tau}(v-V_{\text{rest}})(v-V_{\text{thresh}})F(v,t) = \lim_{v\to V_{thesh}} \frac{1}{\tau}(v-V_{\text{rest}})(v-V_{\text{thresh}})F(v,t), \\ F(v,0) = F^0(v) \geq 0, \quad V_{\text{rest}} \leq v \leq V_{\text{thresh}}. \end{cases} \tag{3.7}$$

Due to delay and advance term we extend F by 0 for outside the domain.
The above equation is a hyperbolic partial differential equation (PDE) which includes delay in $v; F(v-\alpha,t)$ and advance in $v; F(v+\beta,t)$. Due to these arguments (delay and advance) and variable coefficients in t; $p_e(t)$, $p_i(t)$ in above equation, the analytical solution is not possible. Therefore, numerical methods are generally used to find the approximate solution of the model equation. The finite difference methods [56, 71, 120], quadrature type method [146] and finite element methods [122] are usually used to solve such type of biological model equation whereas the finite volume method had never been utilized. For all the above reasons, we propose a scheme based on FVM. In addition, the proposed scheme is high-order accurate for governing equation. Moreover, the geometrical flexibility of FVM is critical to deal with sophisticated neuron models that usually have complicated geometries within the computational domain.

We here draw the main features of the present study:

- QIF neuron model is being used to study the variability of neuronal population.
- The present study adopted population density approach and such an approach is useful to the simulation of neural network.

- Construct a high-order accurate finite volume method to find the approximate solution of governing Eq. (3.7).
- The efficiency of the design scheme is demonstrated via numerical simulations.

The remaining sections are organized as follows. In Section 2, we introduce some preliminaries about TVD (total variation diminishing) scheme that is related to SSP (strong stability preserving) method. Section 3 is devoted to the construction of deterministic scheme. To check the performance of the design scheme, we take some test examples in Section 4. In the final section, we present a summary about the chapter.

2 Preliminaries and Definitions

Definition 2.1. The total variation of a discrete scalar solution at nth time level is defined as

$$TV(p^n) = \sum_j |p^n_{j+1} - p^n_j|.$$

The scheme is said to be total variation diminishing (TVD) if

$$TV(p^{n+1}) \leq TV(p^n).$$

The scheme is total variation bounded (TVB) if $\exists$ some constant $B > 0$, depending on the initial data p^0, total variation $TV(p^0)$ and all possible values of n, and Δt with $n\Delta t \leq T_{end}$, such that

$$TV(p^n) \leq B.$$

Remark 2.1. *TVD* implies *TVB.*

Remark 2.2. TVD methods ensure that the total variation of numerical solution does not increase with time which is a fundamental property of the exact solution of hyperbolic conservation law. Hence, we can say that the TVD numerical methods just mimic the property of the exact solution stated above.

3 Numerical Approximation

Finite volume methods are well known for the approximate solution of hyperbolic conservation laws. In this chapter, the proposed approach is based on method of lines. Here, we used finite volume fifth-order WENO scheme for spatial discretization and strong stability preserving explicit Runge-Kutta scheme three-step three-order (SSPERK(3,3)) for temporal discretization.

3.1 Spatial Discretization

For the discretization of model equation, we rewrite Eq. (3.7) as follows

$$\partial_t F(v,t) = -\frac{\partial}{\partial v}\left[\frac{1}{\tau}\left([(v-V_{\text{rest}})(v-V_{\text{thresh}})]\right)F(v,t)\right] + p_e(t)(F(v-\alpha,t)-F(v,t)) + p_i(t)(F(v+\beta,t)-F(v,t)). \tag{3.8}$$

In standard form it can be read as

$$\partial_t F(v,t) = -\partial_v \mathsf{H}(F,v) + \mathsf{S}(F,t), \tag{3.9}$$

where

$\mathsf{H}(F,v) = \frac{1}{\tau}\left[(v-V_{\text{rest}})(v-V_{\text{thresh}})\right]F(v,t)$ is the flux term, and

$\mathsf{S}(F,t) = p_e(t)\left[F(v-\alpha,t)-F(v,t)\right] + p_i(t)\left[F(v+\beta,t)-F(v,t)\right]$ is the source term.

Due to the presence of delay and advance difference term, we decompose the domain $[V_{\text{rest}}, V_{\text{thresh}}]$ into uniform grid cells $[v_{j-1/2}, v_{j+1/2}],\ j = 1\ldots N$, where $v_{1/2} = V_{\text{rest}}$ and $v_{N+1/2} = V_{\text{thresh}}$, with step size Δv in such a way so that the jumps α and β are contained in the center of the cells, say $\alpha = 1/2(v_{m-1/2} + v_{m+1/2}),\ \beta = 1/2(v_{n-1/2} + v_{n+1/2}),\ 1 \le m, n \le N$.

Given the approximation of the cell averages of $F(v,t)$ over j^{th} grid cell:

$$\bar{F}_j \approx \frac{1}{\Delta v}\int_{v_{j-1/2}}^{v_{j+1/2}} F(v,t)dv,\ j = 1,\ldots,N.$$

Integral formulation of Eq. (3.9) over $I_j = [v_{j-1/2}, v_{j+1/2}]$, we have

$$\frac{d}{dt}\bar{F}_j(\cdot,t) \equiv -\frac{1}{\Delta v}\left[\mathsf{H}(F(v_{j+1/2},t),v_{j+1/2}) - \mathsf{H}(F(v_{j-1/2},t),v_{j-1/2})\right] + \frac{1}{\Delta v}\int_{v_{j-1/2}}^{v_{j+1/2}} \mathsf{S}(F,t)dv.$$

$$\frac{d}{dt}\bar{F}_j(\cdot,t) \equiv -\frac{1}{\Delta v}\left[\mathsf{H}_{j+1/2} - \mathsf{H}_{j-1/2}\right] + S_j^*. \tag{3.10}$$

where $\mathsf{H}_{j+1/2} = \mathsf{H}(F(v_{j+1/2},t),v_{j+1/2})$, $\mathsf{H}_{j-1/2} = \mathsf{H}(F(v_{j-1/2},t),v_{j-1/2})$ are approximations of the flux term at cell interfaces and S_j^* is approximation of the cell average of the source term. In order to carry out unwinding for stability, we replace $\mathsf{H}_{j+1/2} = \hat{\mathsf{H}}(F^-_{j+1/2}, F^+_{j+1/2})$, where $\hat{\mathsf{H}}(F^-,F^+)$ is a monotone numerical flux.

The modified version of Eq. (3.10) is

$$\frac{d}{dt}\bar{F}_j(\cdot,t) \equiv -\frac{1}{\Delta v}\left[\hat{\mathsf{H}}(F^-_{j+1/2},F^+_{j+1/2}) - \hat{\mathsf{H}}(F^-_{j-1/2},F^+_{j-1/2})\right] + S_j^*. \tag{3.11}$$

We now choose the numerical flux in such a way so that it must be consistent with the original flux term $\mathsf{H}(F,v)$. There are many choices of these type of fluxes such as Godunov

flux:

$$\hat{\mathsf{H}}(F_1, F_2) = \begin{cases} \min\limits_{F_1 \le F \le F_2} \mathsf{H}(F, .) & if\ F_1 \le F_2 \\ \max\limits_{F_2 \le F \le F_1} \mathsf{H}(F, .) & if\ F_1 > F_2. \end{cases}$$

Engquist-Osher flux:

$$\hat{\mathsf{H}}(F_1, F_2) = \int_0^{F_1} \max\left(\frac{d\mathsf{H}(F, .)}{dF}, 0\right) dF + \int_0^{F_2} \min\left(\frac{d\mathsf{H}(F, .)}{dF}, 0\right) dF + \mathsf{H}(0, .).$$

Lax-Friedrichs flux:

$$\hat{\mathsf{H}}(F_1, F_2) = \frac{1}{2}(\mathsf{H}(F_1, .) + \mathsf{H}(F_2, .) - \alpha(F_2 - F_1)),$$

where $\alpha = \max |\mathsf{H}'(F, v)|$.

The differences among these fluxes are significant for low-order scheme but it becomes less significant for high order reconstruction [147, 148]. In this chapter, we choose the simplest and inexpensive, Lax-Friedrichs formulation. The flux expression we use is

$$\hat{\mathsf{H}}(F^-_{j+1/2}, F^+_{j+1/2}) = \frac{1}{2}\left[\mathsf{H}(F^-_{j+1/2}, v_{j+1/2}) + \mathsf{H}(F^+_{j+1/2}, v_{j+1/2}) - \alpha\left(F^+_{j+1/2} - F^-_{j+1/2}\right)\right].$$

Here, the values $F^{\pm}_{j+1/2}$ and $F^{\pm}_{j-1/2}$ are high order point-wise approximations determined by WENO reconstruction procedure. We here present a review of WENO reconstruction procedure for the sake of completeness. The details about this method can be found in [147, 149–151].

We first calculate three reconstructed values based on the stencils

$$S^{(0)}_j = \{I_{j-2}, I_{j-1}, I_j\},\ S^{(1)}_j = \{I_{j-1}, I_j, I_{j+1}\},\ S^{(2)}_j = \{I_j, I_{j+1}, I_{j+2}\}, \tag{3.12}$$

as follows:

$$F^{(0)}_{j+1/2} = F^{(0)-}_{j+1/2} = \frac{1}{3}\bar{F}_{j-2} - \frac{7}{6}\bar{F}_{j-1} + \frac{11}{6}\bar{F}_j; \quad F^{(0)}_{j-1/2} = F^{(0)+}_{j-1/2} = -\frac{1}{6}\bar{F}_{j-2} + \frac{5}{6}\bar{F}_{j-1} + \frac{1}{3}\bar{F}_j,$$

$$F^{(1)}_{j+1/2} = F^{(1)-}_{j+1/2} = -\frac{1}{6}\bar{F}_{j-1} + \frac{5}{6}\bar{F}_j + \frac{1}{3}\bar{F}_{j+1}; \quad F^{(1)}_{j-1/2} = F^{(1)+}_{j-1/2} = \frac{1}{3}\bar{F}_{j-1} + \frac{5}{6}\bar{F}_j - \frac{1}{6}\bar{F}_{j+1},$$

$$F^{(2)}_{j+1/2} = F^{(2)-}_{j+1/2} = \frac{1}{3}\bar{F}_j + \frac{5}{6}\bar{F}_{j+1} - \frac{1}{6}\bar{F}_{j+2}; \qquad F^{(2)}_{j-1/2} = F^{(2)+}_{j-1/2} = \frac{11}{6}\bar{F}_j - \frac{7}{6}\bar{F}_{j+1} + \frac{1}{3}\bar{F}_{j+2}.$$

The WENO reconstruction is a convex combination of all the above reconstructed values, therefore,

$$F^-_{j+1/2} = \sum_{r=0}^{2} \omega_r F^{(r)-}_{j+1/2}; \quad \sum_{r=0}^{2} \omega_r = 1, \quad \text{and } \omega_r = \frac{\alpha_r}{\sum\limits_{m=0}^{2} \alpha_m}, \quad \alpha_r = \frac{\gamma_r}{(\epsilon + \beta_r)^2},$$

$$F^{+}_{j-1/2} = \sum_{r=0}^{2} \tilde{\omega_r} F^{(r)+}_{j-1/2}; \quad \sum_{r=0}^{2} \tilde{\omega_r} = 1, \text{ and } \tilde{\omega_r} = \frac{\tilde{\alpha_r}}{\sum_{m=0}^{2} \tilde{\alpha_m}}, \quad \tilde{\alpha_r} = \frac{\tilde{\gamma_r}}{(\epsilon + \beta_r)^2}, \tilde{\gamma_r} = \gamma_{2-r},$$

where $\omega_r, \tilde{\omega_r} \geq 0$ are non-linear weights and γ_r are linear weights whose values are given by $\gamma_0 = \frac{1}{10}, \gamma_1 = \frac{6}{10}, \gamma_2 = \frac{3}{10}$. The terms β_r are the smoothness indicators of the stencil $S^{(r)}_j$ to measure the smoothness of the function $F(v,t)$ in the stencil, while $\epsilon = 10^{-6}$ is just a number to avoid the denominator to become zero. The values of smoothness indicators are given by

$$\beta_0 = \frac{13}{12}\left(\bar{F}_{j-2} - 2\bar{F}_{j-1} + \bar{F}_j\right)^2 + \frac{1}{4}(\bar{F}_{j-2} - 4\bar{F}_{j-1} + 3\bar{F}_j)^2.$$
$$\beta_1 = \frac{13}{12}\left(\bar{F}_{j-1} - 2\bar{F}_j + \bar{F}_{j+1}\right)^2 + \frac{1}{4}(\bar{F}_{j-1} - \bar{F}_{j+1})^2.$$
$$\beta_2 = \frac{13}{12}\left(\bar{F}_j - 2\bar{F}_{j+1} + \bar{F}_{j+2}\right)^2 + \frac{1}{4}(3\bar{F}_j - 4\bar{F}_{j+1} + \bar{F}_{j+2})^2.$$

The next step is to find the approximate solution of source term,

$$\mathsf{S}^{*}_j = \frac{1}{\Delta v} \int_{v_{j-1/2}}^{v_{j+1/2}} \mathsf{S}(F,t)dv = \bar{\mathsf{S}}_j, \ \bar{\mathsf{S}}_j = p_e(t)(\bar{F}_{j-m} - \bar{F}_j) + p_i(t)(\bar{F}_{j+n} - \bar{F}_j).$$

We now turn our attention to the rezoning approach for temporal discretization.

3.2 Temporal Discretization (strong-stability-preserving method)

In this study, we use SSPERK(3,3) scheme based on TVD, for the time integration of the following ODE (ordinary differential equation) system.

Consider the semi-discrete scheme of model Eq. (3.7) at n^{th} time level

$$\frac{d\bar{F}^n_j}{dt} = \mathsf{L}(\bar{F}^n_j, t^n), \tag{3.13}$$

where L is the numerical approximation of the flux and the source term, determined by WENO finite volume method.

$$\mathsf{L}(F(v,t),t) \approx -\frac{\partial}{\partial v}\left[\frac{1}{\tau}\left([(v - V_{\text{rest}})(v - V_{\text{thresh}})]\right)F(v,t)\right] + p_e(t)(F(v-\alpha,t) - F(v,t)) + p_i(t)(F(v+\beta,t) - F(v,t)).$$

Next step is to compute the numerical solution at $(n+1)^{th}$ time level. This is achieved by the aforementioned method, details can be found in [151–153]. When it is applied to Eq. (3.12), we obtain,

$$\bar{F}^{(1)}_j = \bar{F}^n_j + \Delta t \mathsf{L}\left(\bar{F}^n_j, t^n\right),$$
$$\bar{F}^{(2)}_j = \frac{3}{4}\bar{F}^n_j + \frac{1}{4}\bar{F}^{(1)}_j + \frac{1}{4}\Delta t \mathsf{L}\left(\bar{F}^{(1)}_j, t^n + \Delta t\right),$$

$$\bar{F}_j^{n+1} = \frac{1}{3}\bar{F}_j^n + \frac{2}{3}\bar{F}_j^{(2)} + \frac{2}{3}\Delta t \mathsf{L}\left(\bar{F}_j^{(2)}, t^n + \Delta t/2\right),$$

where Δt is the time step which is conditioned by the following CFL restriction:

$$\Delta t \leq C \frac{\Delta v}{\max\limits_v \left|\frac{1}{\tau}(v - V_{\text{rest}})(v - V_{\text{thresh}})\right|},$$

where C is a CFL coefficient and according to [151] we take $C = 1$. Since the spatial approximation is high order accurate, the CFL condition does not yield restrictive time stepping.

4 Numerical Experiments

In this section, we present some applications of our model introduced in Section 1. In order to validate the numerical results, we compare the simulations of our model with the simulations determined by the existing schemes in the literature [121, 122], which was used for the population of leaky integrate-and-fire neurons. Here, we discuss the blow up phenomena of excitatory population of quadratic integrate-and-fire neurons. For this case, we assume that the frequency of inhibitory input rate is zero, i.e., $p_i = 0$. We now choose the following parameters in model Eq. (3.7),

$$\tau = 1,\ \alpha = 0.5,\ p_e(t) = \frac{3}{2 - t + t^4},\ p_i(t) = 0,$$

according to the analyzed phenomena [121, 122]. Here, we normalized the domain $[V_{\text{rest}}, V_{\text{thresh}}]$ into $[0, 2]$ interval, where $V_{\text{rest}} = 0$, and $V_{\text{thresh}} = 2$.
The initial approximation is taken of Gaussian type,
i.e., $F(v, 0) = e^{-10(4v-5)^2}$.
The boundary condition is given by

$$F(v, t) = 0,\ v \in [-\alpha, 0] \cup [2, 2 + \beta].$$

The numerical results of the above problem at different time levels are plotted in Fig. 3.3. This figure depicts the evolution in time of the membrane potential distribution of the excitatory neuron population. In all the plots there are three curves: the blue solid bar line represents the numerical solution determined by WENO-FVM, red solid line for MUSCL-FVM based on quadratic reconstruction, and black dotted line for UFVEM. As time goes on, the number of potential jumps increase and the solution curve tends to stabilize to a steady state which can be seen in the lower right plot of Fig. 3.3. Further, Fig. 3.4, displays the influence of excitatory input rate in modeling equation (3.7). Under the influence of excitatory impulse rate, p_e, taken constant in the simulation, the potential jump move towards the threshold potential, see again in Fig. 3.4 (the threshold potential

is the critical level to which a membrane potential must be depolarized to initiate an action potential/spike. Threshold potential is necessary to propagate signaling to the neuronal system). From the above observation, we conclude that the excitatory neurons are the responsible factor of neuronal firing in a neural network. In other words, the excitatory neurons respond by finite potential jumps when they receive the incoming spikes from other neurons. The resolution of Example 1 in 3D at different time levels, determined by all three schemes, is displayed in Fig. 3.5.

In order to show the accuracy and rate of convergence of the proposed scheme in the absence of exact solution, we measured by calculating errors in the discrete L_∞ norm, where the maximum absolute error is given by

$$\epsilon^N = \max_{v\in\Omega_h} \left| F_j^N - F_j^{2N} \right|, \Omega_h = \{V_{\text{rest}} = v_0, v_1, \cdots, v_N = V_{\text{thresh}}\}.$$

Here, the terms F_j^N and F_j^{2N} are numerical solutions with N and $2N$ grid points, respectively. Further, the rate of accuracy is given by

$$r = \log_2 \left(\epsilon^N / \epsilon^{2N} \right).$$

The max-norm error for F is calculated for above three schemes. The results are displayed in Table 3.1 which show that the proposed scheme is of order 4 in space for the considered problem, while MUSCL and UFVEM schemes converge to the order 3 and 2, respectively. The max-norm error of F for WENO, MUSCL, and UFVEM schemes at time $t = 0.5$ is displayed in Fig. 5(D). The above results show that the accuracy of present scheme is better than the existing schemes in the literature. Moreover, the proposed scheme requires less CPU time than the other two schemes. The next example is taken to show the behavior of inhibitory neuron population. In this case, we assume that the excitatory input rate $p_e(t) = 0$.

Example 2. Consider the model equation (3.7) with the following parameters,

$$\tau = 1,\ \beta = 0.5,\quad p_e(t) = 0,\ p_i(t) = \frac{3 - 2t^6}{1 + 2t^2}.$$

The initial and boundary conditions are given by

$$F(v, 0) = e^{-10(4v-5)^2},$$
$$F(v, t) = 0,\ v \in [-\alpha, 0] \cup [2, 2 + \beta].$$

The numerical solution $F(v, t)$ of this problem is shown in Fig. 3.6 at different time

levels. From this figure, we observe that the solution curve tends to stabilize to a steady state. The influence of inhibitory input rate in time evolution of potential distribution of modeling Eq. (3.7) are shown in Fig. 3.7. Due to this, (inhibitory input rate, p_i, taken constant in the simulation) the potential jump move gradually towards the resting potential, see in Fig. 3.7. The computation of max-norm error determined by WENO-FVM, MUSCL-FVM and UFVEM at time $t = 0.5$ are displayed in Table 3.2. From this table, we again observe that the proposed scheme is more accurate than the other schemes which are used in the literature. In Fig. 3.8, we can see the visualization of Example 2 in 3D. The max-norm errors of F for Example 2 is plotted in Fig. 3.8(D).

Example 3. This example is taken to show the performance of proposed scheme in case of discontinuous problem. Let us consider Eq. (3.7) with some modifications and choose the following parameters,

$$\tau = 1,\ \alpha = 0.2,\ \beta = 0.5,\ p_e(t) = 0.2,\ p_i(t) = 0.2,\ \mathsf{H}(F, v) = \mathsf{a}v,\ \mathsf{a} = -0.3.$$

The initial and boundary conditions are given by

$$F(v,0) = \begin{cases} 0 & v > 1.7, v < 1.3 \\ 0.3 & 1.3 \leq v \leq 1.7 \end{cases}$$
$$F(v,t) = 0,\ v \in [-\alpha, 0] \cup [2, 2+\beta].$$

From Fig. 3.9, we observe that our proposed scheme and MUSCL scheme perform nicely and give accurate solutions than the UFVEM scheme. The solution obtained by these two schemes depict no numerical oscillations. However, MUSCL scheme used 800 grid cells to obtain the above resolution, while our proposed scheme needs only 160 grid cells to achieve comparable resolution. From all the above observations, we point out that the proposed scheme is efficient for this model equation.

Table 3.1: Error table for Example 1 by using three different schemes at time $t = 0.5$

	WENO			MUSCL			UFVEM		
N	$\|\|\|_\infty$	r	CPU(s)	$\|\|\|_\infty$	r	CPU(s)	$\|\|\|_\infty$	r	CPU(s)
20	1.59e-2	-	0.0766	1.60e-2	-	0.1098	8.56e-2	-	0.1670
40	9.46e-4	4.07	0.0945	2.11e-3	2.92	0.1481	1.96e-2	2.12	0.1859
80	5.18e-5	4.19	0.1618	3.29e-4	2.68	0.1514	5.02e-3	1.97	0.2264
160	3.24e-6	4.00	0.1971	4.53e-5	2.86	0.3397	1.31e-3	1.93	0.3727
320	1.90e-7	4.09	0.2141	8.41e-6	2.43	0.4891	3.92e-4	1.75	0.7998

Table 3.2: Error table for Example 2 by using three different schemes at time $t = 0.5$

	WENO			MUSCL			UFVEM		
N	$\|\|\|_\infty$	r	CPU(s)	$\|\|\|_\infty$	r	CPU(s)	$\|\|\|_\infty$	r	CPU(s)
20	2.12e-2	-	0.0992	2.12e-2	-	0.1494	3.70e-2	-	0.1781
40	1.56e-3	3.76	0.1207	5.42e-3	1.97	0.1819	1.73e-2	1.09	0.2024
80	1.04e-4	3.91	0.1579	1.49e-3	1.86	0.2462	8.01e-3	1.11	0.3265
160	6.64e-6	3.97	0.1712	4.20e-4	1.83	0.4065	3.97e-3	1.01	0.4197
320	4.29e-7	3.95	0.2219	1.21e-4	1.79	0.6907	1.78e-3	1.16	0.9613

4.1 Authors' Contributions

The model of the current study is inspired from the base model given in [17] and modified version in [120, 122]. The model equation provided by these authors is based on leaky integrate-and-fire neuron. In the present study, the model equation is based on quadratic integrate-and-fire neuron. The reason behind that the QIF model does have a spike generation mechanism, which makes it suitable for us to describe the internal behavior of a neuronal population. Further-also, we used different and latest approach for the derivation of the model equation called population density approach. Our main aim is to find the numerical solution based on the model presented here for the occurrence of interesting behaviors of neuronal population, such as neuronal firing. In addition, we introduced a discontinuous example to check the efficiency of proposed scheme.

5 Summary

The model equation is based on a quadratic-integrate-and-fire neuron. With the help of population density approach, we obtained a model equation, which is a hyperbolic partial differential equation. Due to the delay, advance shifts, and non-constant coefficients, the analytical solution is not possible. Therefore, we designed a high-order numerical scheme for the simulation of model equation. Moreover, we have discussed the role of an inhibitory and excitatory part in the variation of neuronal firing. The validation of designed scheme is made by comparing it with the existing schemes in the literature. It is also observed that the proposed scheme performs nicely in case of the discontinuous solution.
The next chapter presents a numerical study of an excitatory and inhibitory population density model based on leaky integrate-and fire neurons with jumps.

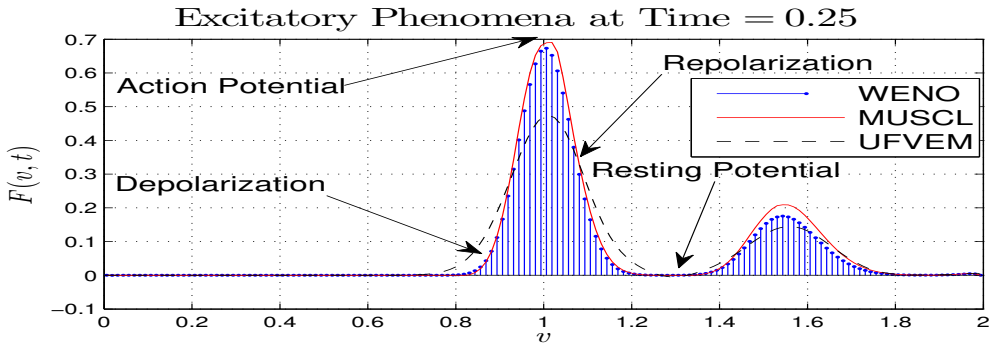

(a) Numerical solution of Experiment 1 at time $t = 0.25$

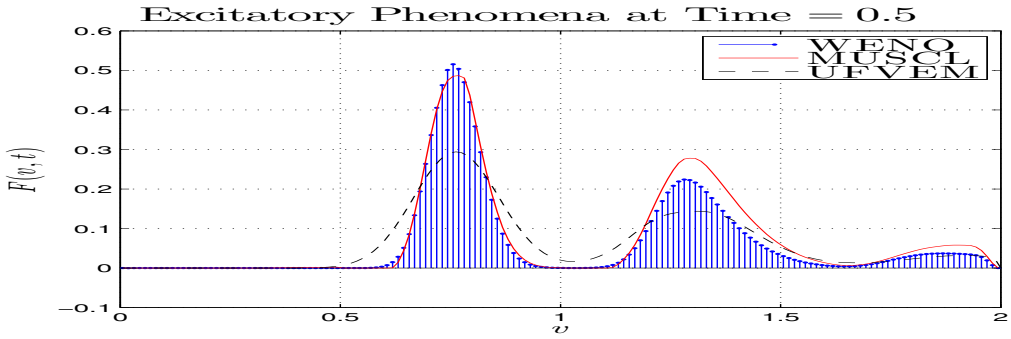

(b) Numerical solution of Experiment 1 at time $t = 0.50$

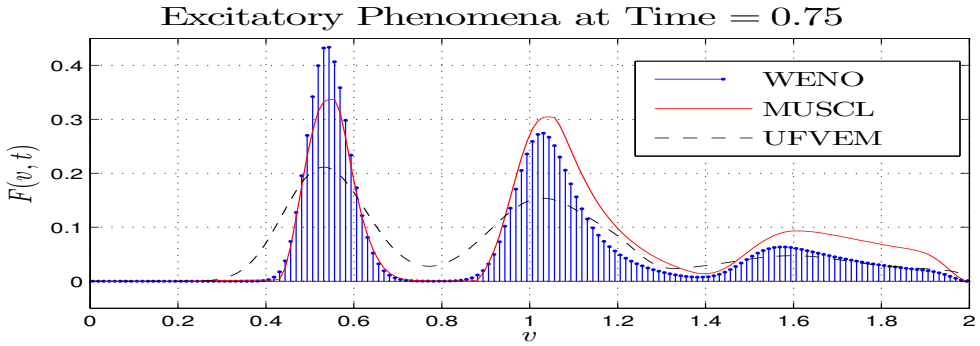

(c) Numerical solution of Experiment 1 at time $t = 0.75$

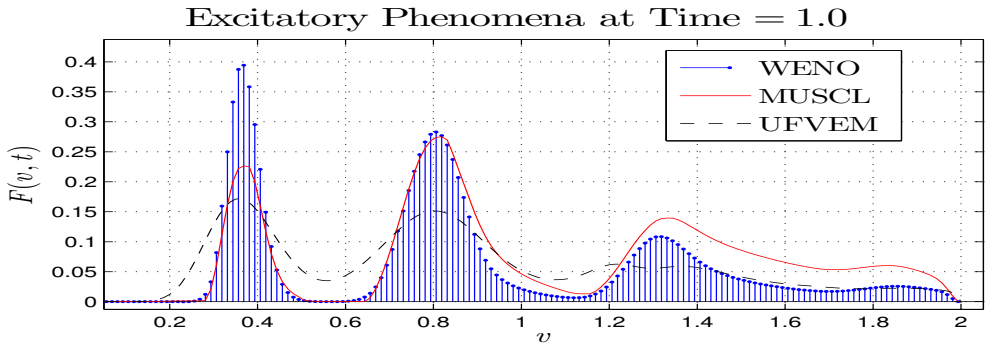

(d) Numerical solution of Experiment 1 at time $t = 1$

Figure 3.3: Excitatory Phenomena : Blue solid bar line represents the numerical solution determined by WENO-FVM, red solid line for MUSCL-FVM and black dotted line for UFVEM by using 160 grid points.

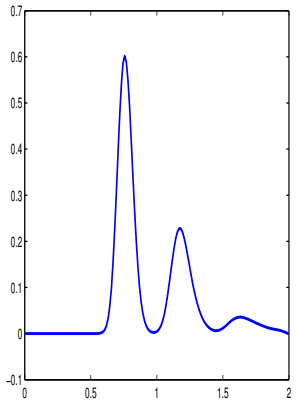

(a) $p_e = 2$

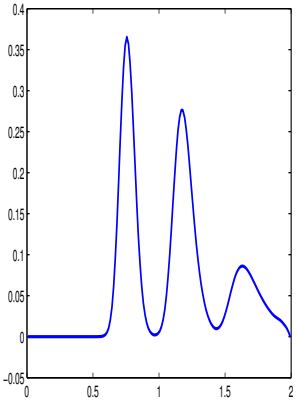

(b) $p_e = 4$

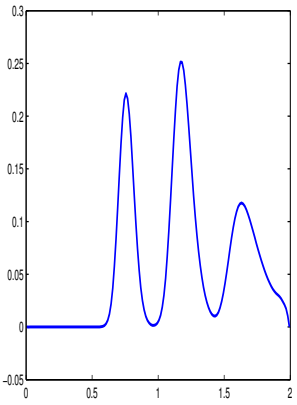

(c) $p_e = 6$

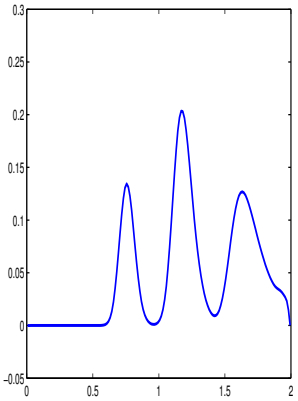

(d) $p_e = 8$

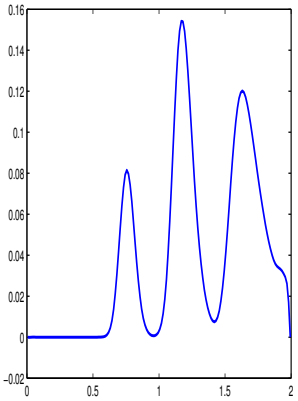

(e) $p_e = 10$

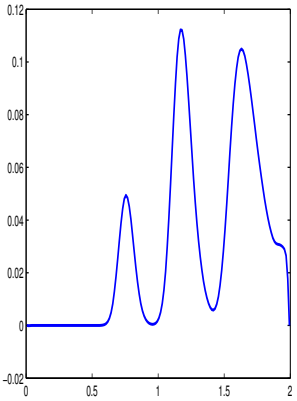

(f) $p_e = 12$

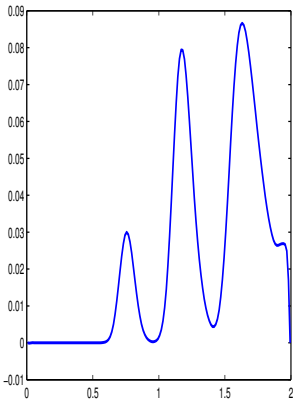

(g) $p_e = 14$

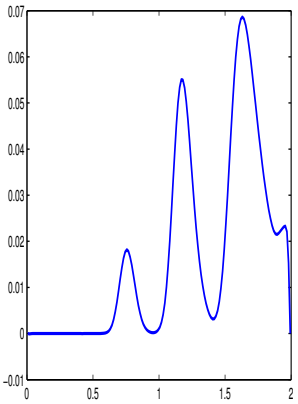

(h) $p_e = 16$

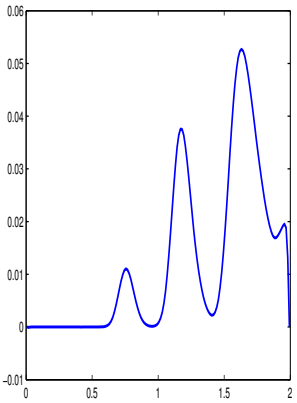

(i) $p_e = 18$

Figure 3.4: The time evolution of population density function under the influence of excitatory input rates at time level $t = 0.5$.

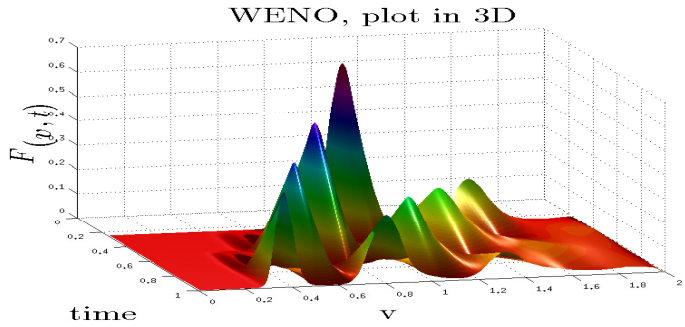

(a) Numerical solution $F(v,t)$ determined by WENO-FVM in 3D for Experiment 1 at different time levels t=0.25, 0.50, 0.75, 1.0 with N=160

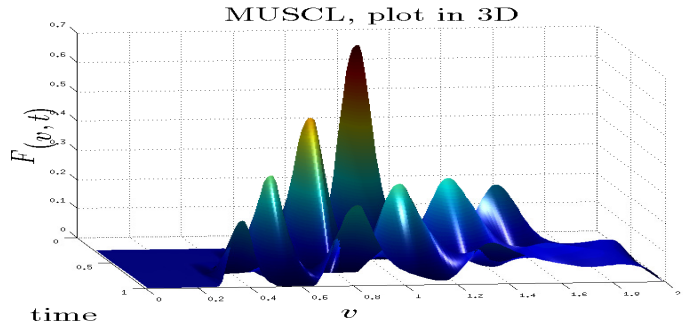

(b) Numerical solution $F(v,t)$ determined by MUSCL-FVM in 3D for Experiment 1 at different time levels t=0.25, 0.50, 0.75, 1.0 with N=160

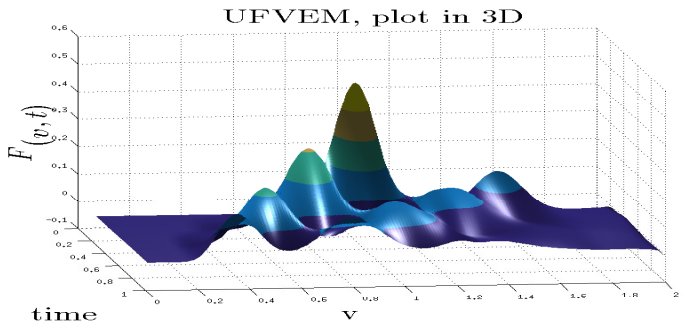

(c) Numerical solution $F(v,t)$ determined by UFVEM in 3D for Experiment 1 at different time levels t=0.25, 0.50, 0.75, 1.0 with N=160

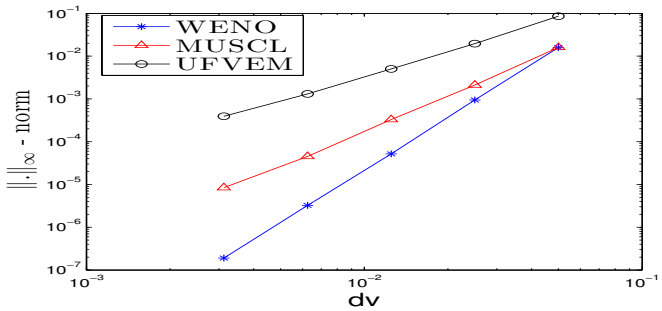

(d) The max norm plot of the computed solution of Experiment 1 determined by three different scheme.The slopes of the curves are the order of convergence.

Figure 3.5: Concentration profiles of $F(v,t)$ of Example 1 at different time levels.

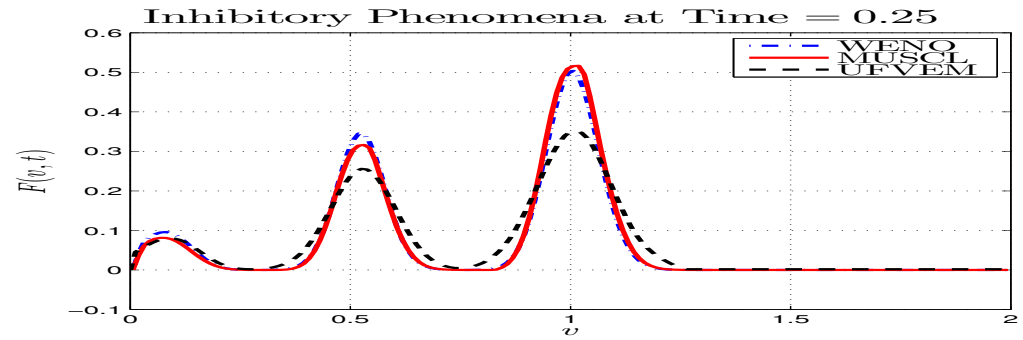

(a) Numerical solution of Experiment 2 at time $t = 0.25$

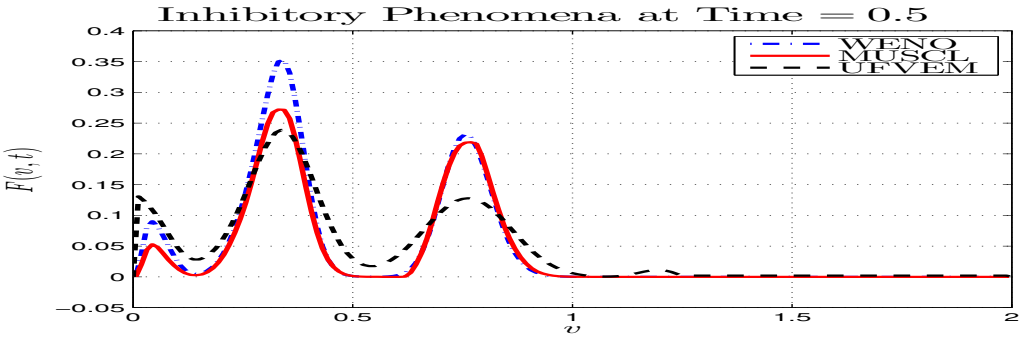

(b) Numerical solution of Experiment 2 at time $t = 0.50$

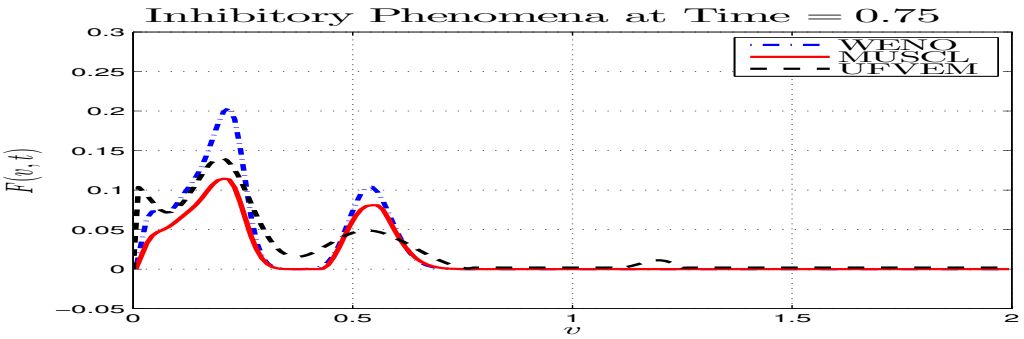

(c) Numerical solution of Experiment 2 at time $t = 0.75$

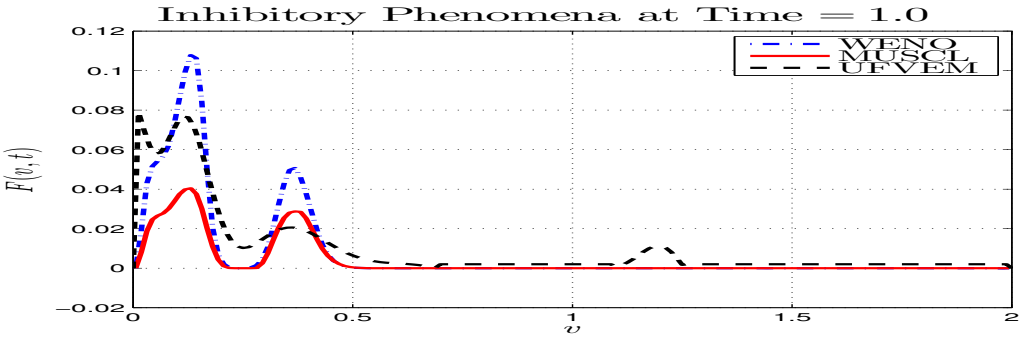

(d) Numerical solution of Experiment 2 at time $t = 1.0$

Figure 3.6: Inhibitory Phenomena : blue solid line represents the numerical solution determined by WENO-FVM, red solid line for MUSCL-FVM and black dotted line for UFVEM by using 160 grid points.

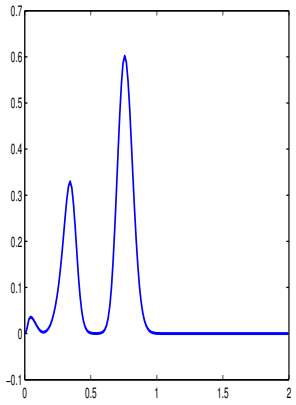

(a) $p_i = 2$

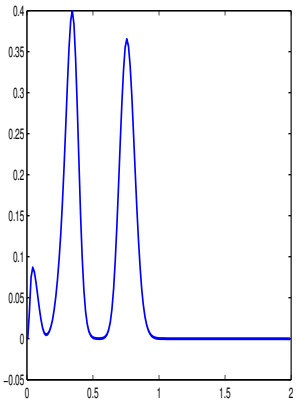

(b) $p_i = 4$

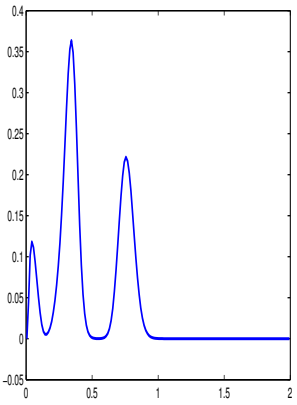

(c) $p_i = 6$

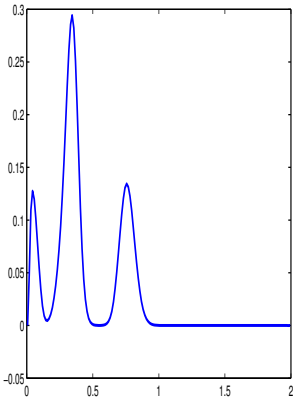

(d) $p_i = 8$

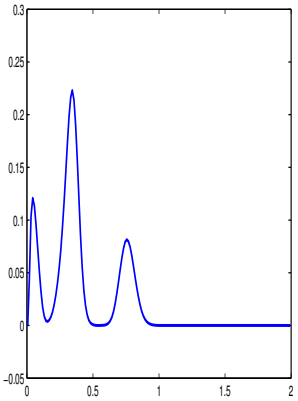

(e) $p_i = 10$

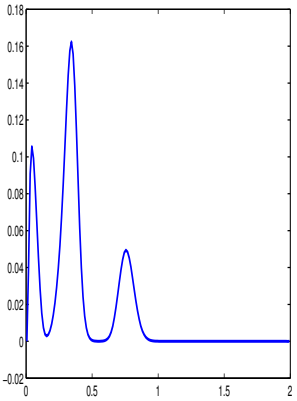

(f) $p_i = 12$

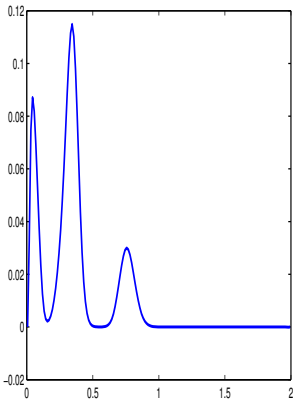

(g) $p_i = 14$

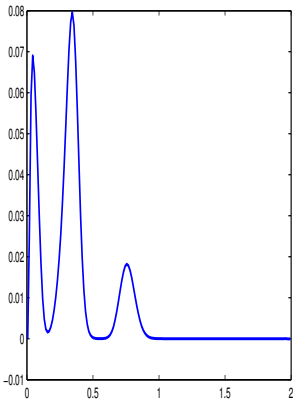

(h) $p_i = 16$

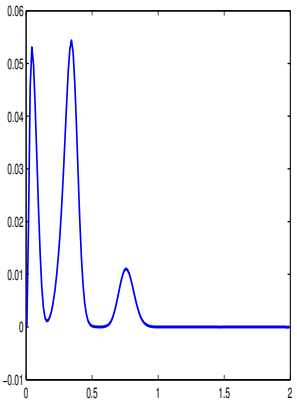

(i) $p_i = 18$

Figure 3.7: The time evolution of population density function under the influence of inhibitory input rate at time level $t = 0.5$.

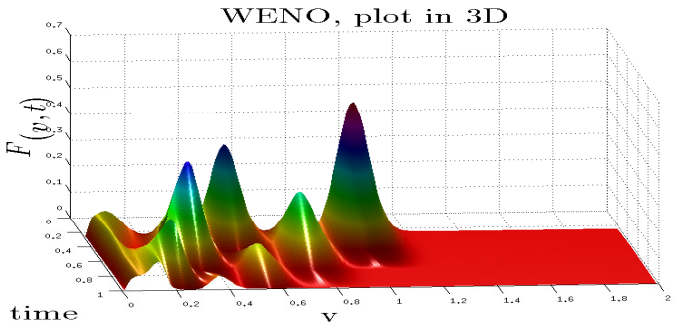

(a) Numerical solution $F(v,t)$ determined by WENO-FVM in 3D for Experiment 2 at different time levels t=0.25, 0.50, 0.75, 1.0 with grids N=160

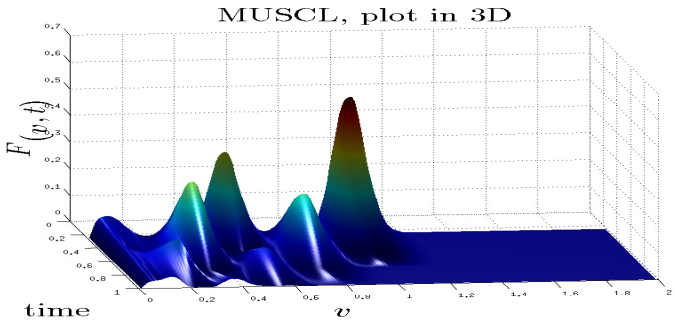

(b) Numerical solution $F(v,t)$ determined by TVD-RK in 3D for Experiment 2 at different time levels t=0.25, 0.50, 0.75, 1.0 with grids N=160

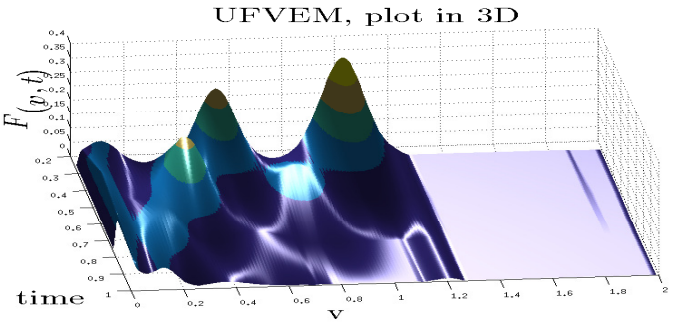

(c) Numerical solution $F(v,t)$ determined by UFVEM in 3D for Experiment 2 at different time levels t=0.25, 0.50, 0.75, 1.0 with grids N=160

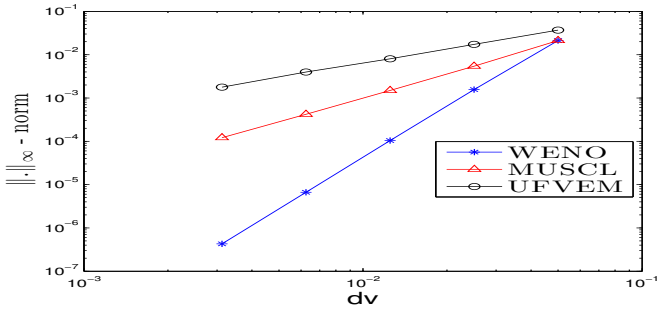

(d) The max norm plot of the computed solution of Experiment 2 determined by three different scheme.The slopes of the curves are the order of convergence.

Figure 3.8: Concentration profiles of $F(v,t)$ of Example 2 at different time levels.

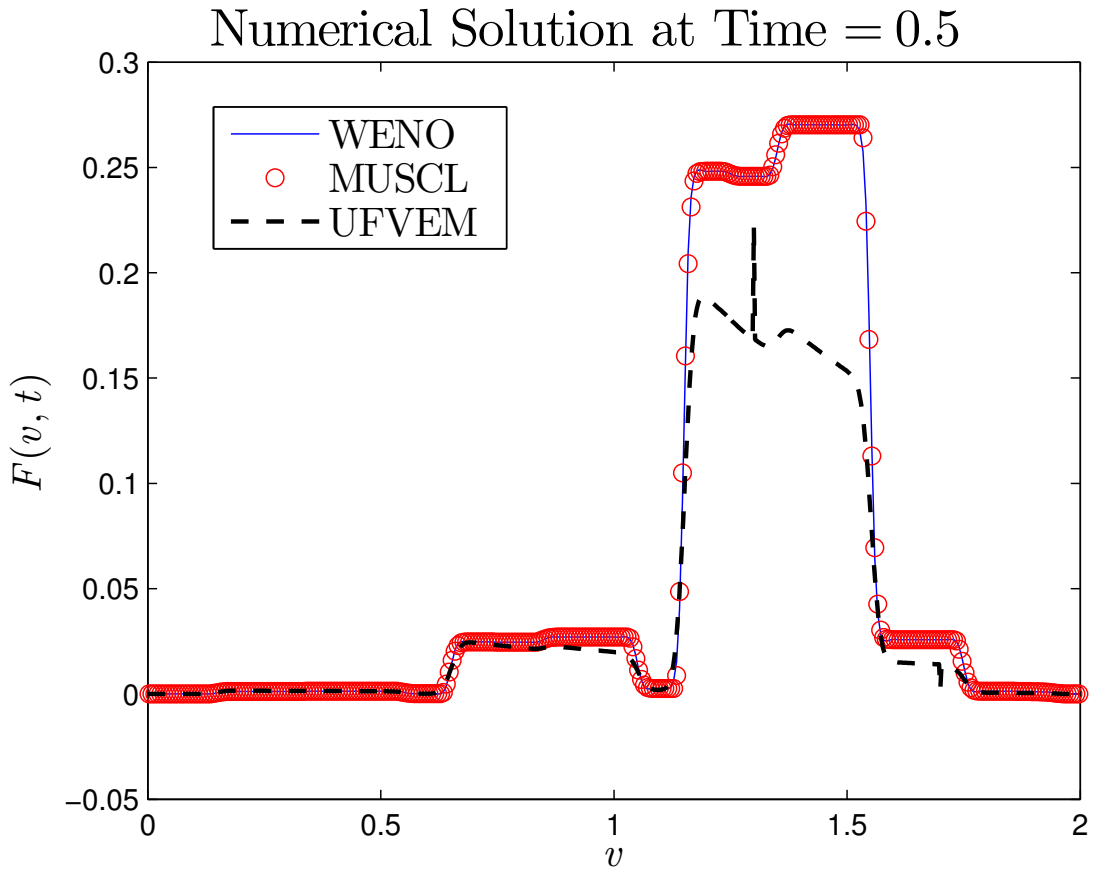

(a) Numerical solution of Experiment 3 at time $t = 0.20$

Figure 3.9: Excitatory-Inhibitory Phenomena : blue solid line represents the numerical solution determined by WENO scheme, red circle for MUSCL scheme and black dotted line for UFVEM at time t=1.0.

Chapter 4

A Numerical Study of the Excitatory and Inhibitory Population Density Model [3]

The last chapter presented the numerical study of population density model based on quadratic integrate-and-fire neurons. This chapter describes the excitatory and inhibitory population density model based on leaky integrate-and-fire neuron with jumps. The time evolution of population density function is determined by a hyperbolic partial differential equation. There are two factors which may cause difficulties to find the solution. First one is the presence of point-wise delta type source term and second one is the presence of the non-local terms of the voltage of a neuron. The chapter also presents a high accurate scheme based on finite volume weighted essential non-oscillatory (WENO) scheme for spatial discretization. The time evolution is done through SSPRK (strong stability preserving Runge-Kutta) scheme. This chapter also includes some empirical examples. Further, the behavior of governing model is compared with its diffusion approximation. The performance of the designed scheme is shown by the convergence results.

1 Introduction

The capacity to simulate the brain activities on the computer is confined by available computational time, because a small part of the brain includes tens of thousands of neurons and billions of synapses (synapse is a junction at which a neuron communicates with another neuron). Even today computers are emerging very fast, but these models have limited study due to very high computational time. If one would like to approximate the networks of neurons more closely, various factors have to be included and analyzed carefully which can further create additional difficulties and the required computational time can be unrealistic.

The population density approach is innovated for the simulation of large-scale neural networks, which is initiated from an ordinary differential equation (ODE), describes the

[3] Santosh Kumar and Paramjeet Singh, *"A numerical treatment for the excitatory and inhibitory population density model"*, [under review].

dynamics of a single neuron. Under the key assumption that there is a large population of similar neurons, one can derive a partial differential equation (PDE) that describes the behavior of the whole population of neurons [56, 70, 71]. The possible applications of these approach are numerous, see for instance [60, 72, 154, 155]. In addition, it can also be used for the realistic models with two or three state variables describing the dynamics of a single neuron, one can derive a two or three-dimensional PDE for the whole population [59, 156]. However, such type of PDEs are very difficult to simulate and analyse. A large amount of mathematical tools such as moment reduction [59] and phase reduction [11] were used to reduce the computational time.

In this chapter, the large-scale excitatory and inhibitory neuronal networks is considered. More information about the behavior of this neural network can be found in [67, 157–161] and references therein. In present study, this approach (population density approach) is used for the simulation of considered neural network. The approach is based on one-dimensional leaky integrate-and-fire (LIF) neuron model that determines one dimensional hyperbolic PDE [56, 71]. Although, the governing equation is one dimensional, analytic solution of the model is intractable due to it's high nonlinearity. In literature, there are some analytical methods, for example, characteristic method [69] and eigenfunction theory [162], that have been proposed to solve such type of PDEs, but these theories are restricted for some simplified cases. Therefore, numerical schemes are usually used to solve the governing equation. The finite difference method (FDM) and finite element method (FEM) have been proposed to solve such type of PDEs, see in [120, 142, 163, 164]. However, these techniques have some drawbacks. For example, if the governing equation contains delta type source term, the solution of the population density become divergent in case of FDM. In order to use FDM appropriately, the modification of the governing equation is necessary. In modification, the density function is separated into a smooth component and a delta function component in which the smooth density is still governed by a nonlinear PDE whereas the delta function component is described by an ODE, see in [56]. On the other hand, FEM solves this issue, but it makes the solution more complicated. Moreover, FEM produces less physical significance solution in some cases of the population density approach. Hence, the present study proposes a formulation based on finite volume method (FVM) for the governing equation. In order to see the high-order accuracy and type of model equation, WENO scheme is a suitable scheme for this work, which was innovated by Liu et al. for hyperbolic conservation laws without source term [149]. The scheme was earlier constructed for third order accurate, based on finite volume method. Later it was extended for arbitrary high-order accurate based on FDM by Shu et al. in [150]. In this chapter, WENO scheme based on FVM is designed to solve the governing model equation in which source term is available. Moreover, the proposed

scheme is stable and produce more accurate solutions. To demonstrate the performance of proposed scheme, some test examples are taken. The comparison of results between proposed scheme and upwind FDM (proposed in [56, 71]) have been shown.
The next section reviews the introduction of population density approach and derives the evolution of population density equation. A numerical method for the solution of governing equation is presented in Section 3. Section 4 is devoted to the simulation results and validation of the proposed scheme. The final section summarizes the key features of this chapter.

2 Population Density Approach

The population density approach in present study is based on the leaky integrate-and-fire (LIF) neuron model. In general form, it can be described as

$$\begin{cases} \dfrac{dV}{dt} = -\dfrac{1}{\tau}(V - E_L) + S(t) \\ \text{if } V \geq V_{th} \text{ then } V \to V_r, \end{cases} \tag{4.1}$$

where $V(t)$ is the membrane potential of a neuron and τ is a time membrane constant. A spike occurs in neuron if the membrane potential V crosses the threshold level, V_{th}, and then reset to the resetting potential V_r. In this model, the time variation of V is influenced by the leakage term and current $S(t)$, that is the so called post synaptic current induced by the presynaptic spike train. The presynatpic input $S(t)$ is described as (see [53])

$$S(t) = h\sum_j \delta(t - t_e^j) - h\sum_k \delta(t - t_i^k),\ h > 0, \tag{4.2}$$

where t_e^j and t_i^k are the arrival times of the synaptic input spikes for the excitatory and inhibitory synapses, respectively. These inputs are usually simulated by inhomogeneous Poisson process with individual excitatory and inhibitory synaptic input average rates. Since the dynamics induced by the presynaptic inputs is neglected, it is assumed that each coming spike leads to a delta type change in membrane potential V with a jump of size h. The jump (positive or negative) depending on the input spike is received from excitatory or inhibitory neuron, respectively. Detailed information about LIF model can be found in [4, 9, 48–50, 138, 155, 165, 166] and references therein.

2.1 Population Density Evolution Equation

The population density function $\rho(v,t)$ is based on probability density function. The fraction of neurons with voltage $V(t) \in (v_1, v_2)$ at time t is defined as $= \int_{v_1}^{v_2} \rho(v,t)dv$.
The evolution equation for $\rho(v,t)$ is based on the conservation of total probability. That is the probability contained in any interval can only be changed across the boundary points of that interval.
Let us assume that (a_1, a_2) be any arbitrary interval for which the time variation of total probability is required to be evaluated. Suppose $\mathcal{J}(v,t)$ is the probability flux across v at time t then

$$\mathcal{J}(a_1,t) - \mathcal{J}(a_2,t) = \frac{\partial}{\partial t} P_r\{V(t) \in (a_1,a_2)\} = \frac{\partial}{\partial t}\int_{a_1}^{a_2} \rho(w,t)dw$$

$$\implies -\int_{a_1}^{a_2} \frac{\partial}{\partial v}\mathcal{J}(v,t)dv = \frac{\partial}{\partial t}\int_{a_1}^{a_2} \rho(w,t)dw.$$

Thus

$$\frac{\partial \rho}{\partial t} = -\frac{\partial \mathcal{J}}{\partial v}. \tag{4.3}$$

In order to account the firing rate and reset mechanism of total population, the modified version of Eq. (4.3) is

$$\frac{\partial \rho}{\partial t} = -\frac{\partial \mathcal{J}}{\partial v} + r(t)\delta(v - V_r). \tag{4.4}$$

Here, $r(t)$, is the firing rate of the population and delta term denotes the source of probability at resting potential, V_r, produced by the reset of neurons.
Next step is to compute the flux term, $\mathcal{J}(v,t)$, which can be decomposed into three parts

$$\mathcal{J}(v,t) = \mathcal{J}_L(v,t) + \mathcal{J}_e(v,t) + \mathcal{J}_i(v,t). \tag{4.5}$$

$\mathcal{J}_L(v,t)$ is advective flux developed by the leakage term in the absence of presynaptic input. $\mathcal{J}_e(v,t)$ and $\mathcal{J}_i(v,t)$ are the excitatory and inhibitory flux caused by the receiving of excitatory and inhibitory input, respectively.
Leakage Flux $\mathcal{J}_L(v,t)$: This flux is related to the leakge term (see Eq. (4.1)) [56]. The leakage flux at v is the probability per unit time that a neuron crosses v from the lower side. Any neuron whose voltage $V(t) \in (v - \Delta v, v)$ will cross v in time interval $(t, t + \Delta t)$,

where

$$\Delta v = \frac{dV}{dt}\Delta t.$$

The probability that a neuron is in that interval is

$$\rho(v,t)\Delta v = \rho(v,t)\frac{dV}{dt}\Delta t.$$

Therefore, the leakage flux, the probability per unit time that neuron crosses v

$$\mathcal{J}_L(v,t) = \frac{\rho(v,t)\Delta v}{\Delta t} = \rho(v,t)\frac{dV}{dt} = -\frac{(v-E_L)}{\tau}\rho(v,t). \tag{4.6}$$

Excitation Flux $\mathcal{J}_e(v,t)$: A presynaptic input event elevates the membrane potential of neuron by a jump of size h. Any neuron with voltage $V(t) = v', v' \in (v-h, v)$ will cross v in time interval $(t, t+\Delta t)$ if it receives an excitatory input in this time interval. Let us assume that $I_e(t)$ be the excitatory synaptic input rate which is the probability per unit time that a neuron will receive excitatory input. According to Poisson process [167], the probability that an excitatory synaptic input receive in $(t, t+\Delta t)$ is $I_e(t)\Delta t$. The probability that a neuron with voltage $V(t) \in (v', v'+\Delta v')$ which receives an excitatory input event in time interval $(t, t+\Delta t)$ is

$$\underbrace{\rho(v',t)\Delta v'}_{I}\overbrace{I_e(t)\Delta t}^{II}. \tag{4.7}$$

Note that these two probabilistic events are independent by assumption of Poisson process. The total flux of probability across v in time interval $(t, t+dt)$ is determined by the summation of Eq. (4.7) over all infinitesimal intervals from anywhere below v:

$$\left(\int_{v-h}^{v} \rho(v',t)dv'\right)(I_e(t)\Delta t).$$

The excitation flux, $\mathcal{J}_e(v,t)$, is the probability per unit time across v i.e.

$$\mathcal{J}_e(v,t) = I_e(t)\int_{v-h}^{v} \rho(v',t)dv'. \tag{4.8}$$

In the same manner, the total inhibition flux can be obtained

$$\mathcal{J}_e(v,t) = -I_i(t)\int_{v+h}^{v} \rho(v',t)dv', \tag{4.9}$$

where $I_i(t)$ be the inhibitory synaptic input rate. The excitation/inhibition,$I_{e/i}(t)$, impulse rate is expressed as a sum of external excitatory/inhibitory input rates, $I_{e/i,o}(t)$, and the response of the population, $J\int_0^t \alpha(t')r(t-t')dt'$. When an external synaptic inputs either from excitatory population of neurons or inhibitory population of neurons

arrived in the population, as a result, the population produce the firing rate, $r(t)$, is said to be called firing rate of the population. Further, this firing rate plays a key role in the response of the population. If the population is coupled with strength, $J \neq 0$, and assume that there is some latencies of synapses within the population, the response is given by $J\int_0^t \alpha(t')r(t-t')dt'$ (see Fig. 4.1). Here, $\alpha(t')$, is the distribution of the latency of synapses which satisfy the condition,

$$\int_0^\infty \alpha(t')dt' = 1.$$

If there is no latency of synapses, the corresponding reaction of the population is given by $Jr(t)$ (see Fig. 4.2),

$$\begin{cases} I_{e/i}(t) = I_{e/i,o}(t) + J\int_0^t \alpha(t')r(t-t')dt' \text{ with latencies of synapses.} \\ I_{e/i}(t) = I_{e/i,o}(t) + Jr(t), \text{ without latencies of synapses.} \end{cases}$$

Next step is to compute the firing rate of the population which is determined by the

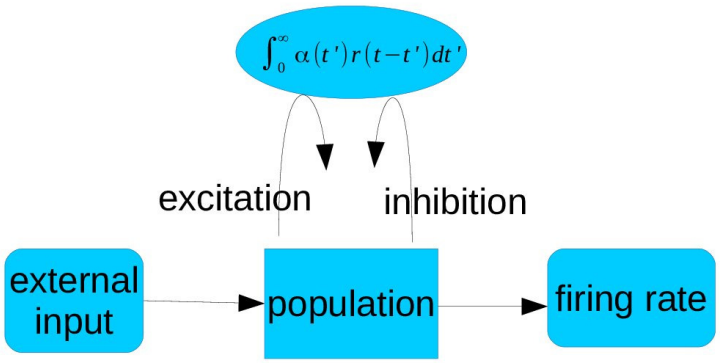

Figure 4.1: The evolution of a population of neuron under external synaptic input with latencies of synapses

probability flux across the threshold level, V_{th},

$$r(t) = \mathcal{J}(V_{th},t) = -\frac{1}{\tau}(V_{th}-E_L)\rho(V_{th},t) + I_e(t)\int_{V_{th}-h}^{V_{th}} \rho(v',t)dv' + I_i(t)\int_{V_{th}}^{V_{th}+h} \rho(v',t)dv'. \tag{4.10}$$

The first and last terms of the right hand side of Eq. (4.8) are actually a flux to the left, so it cannot contribute to the firing rate. Thus, it requires

$$\rho(V_{th},t) = 0, \rho(v,t) = 0, \ \forall v \geq V_{th}.$$

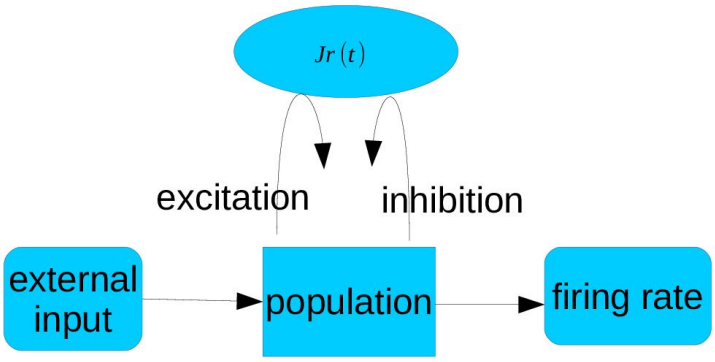

Figure 4.2: The evolution of a population of neuron under external synaptic input without latencies of synapses

Substituting these fluxes in Eqs. (4.6), (4.8) and (4.9) back into Eq. (4.4) yields

$$\frac{\partial \rho}{\partial t} = -\frac{\partial}{\partial v}\left(-1/\tau(v-E_L)\rho(v,t)\right) + I_e(t)\left(\rho(v-h,t)-\rho(v,t)\right)$$
$$+ I_i(t)\left(\rho(v+h,t)-\rho(v,t)\right) + \delta(v-v_r)I_e(t)\int_{V_{th}-h}^{V_{th}} \rho(v',t)dv'. \tag{4.11}$$

Hence, the complete model equation is

$$\begin{cases} \dfrac{\partial \rho}{\partial t} + \dfrac{\partial}{\partial v}\left(-1/\tau(v-E_L)\rho(v,t)\right) = I_e(t)\left(\rho(v-h,t)-\rho(v,t)\right) \\ \qquad\qquad +I_i(t)\left(\rho(v+h,t)-\rho(v,t)\right) + \delta(v-v_r)r(t),\ E_L \le v < V_{th}. \\ I_{e/i}(t) = I_{e/io}(t) + J\displaystyle\int_0^t \alpha(t')r(t-t')dt' \text{ with latencies of synapses.} \\ I_{e/i}(t) = I_{e/io}(t) + Jr(t) \text{ without latencies of synapses.} \\ r(t) = I_e(t)\displaystyle\int_{V_{th}-h}^{V_{th}} \rho(w,t)dw. \end{cases} \tag{4.12}$$

The initial and boundary conditions are given by

$$\rho(v,0) = \rho_0(v) \in C^1(E_L, V_{th}),\ \rho(V_{th},t) = 0. \tag{4.13}$$

The conservation property of the model equation can be easily checked by integrating over the interval (E_L, V_{th}) and using the condition $\rho(V_{th},t) = 0$.
To solve such type of PDEs, the common approach is to first discretize the spatial variables to get a semi-discrete method of a line of approximation. In this approach, the original

PDE is reduced to the system of time-dependent ODE. Then the ODE system is solved by some appropriate ODE solver. The next section presents a numerical scheme in the same manner.

3 Numerical Approximation

This chapter introduces a numerical scheme for Eq. an(4.12) based on the finite volume WENO approximation for the advection term as well as the source term. The time evolution is done by SSP (strong stability preserving) 3rd-order Runge-Kutta method. Consider Eq. (4.12) and rewrite it as follows

$$\partial_t(\rho(v,t)) = -\partial_v\left(\frac{-(v-E_L)\rho(v,t)}{\tau}\right) + I_e(t)\left(\rho(v-h,t)-\rho(v,t)\right) \\ +I_i(t)\left(\rho(v+h,t)-\rho(v,t)\right) + \delta(v-v_r)r(t). \tag{4.14}$$

Discretize the domain $[E_L, V_{th}]$ into uniform grid cells $I_j = [v_{j-1/2}, v_{j+1/2}],\ j = 1,\ldots,N$, with step size $\Delta v = \frac{V_{th}-E_L}{N}$ in such a way so that the jump h contains in center of the cell, say $h = 1/2(v_{m-1/2} + v_{m+1/2}), 1 \le m \le N$. Let $\bar{\rho}_j(t) = \frac{1}{\Delta v}\int\limits_{v_{j-1/2}}^{v_{j+1/2}} \rho(v,t)dv$ denote the approximation of the cell average of $\rho(.,t)$ over the j^{th} grid cell I_j.

The finite volume method approximate the above equation in integral form,

$$\frac{d}{dt}\bar{\rho}_j(t) = -\frac{1}{\Delta v}\left[f(\rho_{j+1/2}, v_{j+1/2}) - f(\rho_{j-1/2}, v_{j-1/2})\right] + \frac{1}{\Delta v}\int\limits_{v_{j-1/2}}^{v_{j+1/2}} S(\rho,t).$$

$$\frac{d}{dt}\bar{\rho}_j(t) \approx -\frac{1}{\Delta v}\left[\hat{f}_{j+1/2} - \hat{f}_{j-1/2}\right] + \bar{S}_j(t).$$

Here,

$f(\rho, v) = -\dfrac{(v-E_L)}{\tau}\rho(t,v)$ is the flux term and

$S(\rho,t) = I_e(t)\left[\rho(v-h,t)-\rho(v,t)\right] + I_i(t)\left[\rho(v+h,t)-\rho(v,t)\right] + \delta(v-v_r)r(t)$ is the source term.

In order to use upwinding for stability, replace $\hat{f}_{j+1/2}$ by $F(\rho^-_{j+1/2}, \rho^+_{j+1/2})$, where $F(\rho^-, \rho^+)$ is a monotone numerical flux. In this work, the flux term is linear, thus the choice of WENO finite volume approximation is just a simple high order for the model equation.

The simple and monotone numerical flux is

$$F(u,v) = \frac{1}{2}\left(f(u) + f(v) - a(v-u)\right),$$

where $a = \max|f'(\rho, v)|$. On the other side, $\bar{S}_j(t)$ denotes the approximation of the cell average of $S(\rho, t)$.
The values $\rho^-_{j+1/2}$ and $\rho^+_{j+1/2}$ are high order point-wise approximation to $\rho(t, v_{j+1/2})$ at the interface of j^{th} cell determined by WENO reconstruction procedure.

WENO-FVM: In this scheme, the advection term of model equation is approximated by a fifth-order conservative finite volume WENO scheme. Basically, WENO scheme was developed for the hyperbolic conservation laws. This type of finite volume method is a mixture of the high accuracy for the smooth part of the evolution and nice treatment of possible steep fronts by locally weighting the best stencils. This chapter summarizes the WENO finite volume approximation for the sake of completeness. The details about this method can be found in [149–151].

Consider the stencils

$$S_j^{(0)} = \{I_j, I_{j+1}, I_{j+2}\},\ S_j^{(1)} = \{I_{j-1}, I_j, I_{j+1}\},\ S_j^{(2)} = \{I_j, I_{j+1}, I_{j+2}\}.$$

which produce 3-different reconstruction for $\rho^-_{j+1/2}$ and $\rho^+_{j-1/2}$, as follows

$$\rho^{(0)-}_{j+1/2} = \frac{1}{3}\bar{\rho}_{j-2} - \frac{7}{6}\bar{\rho}_{j-1} + \frac{11}{6}\bar{\rho}_j; \quad \rho^{(0)+}_{j-1/2} = -\frac{1}{6}\bar{\rho}_{j-2} + \frac{5}{6}\bar{\rho}_{j-1} + \frac{1}{3}\bar{\rho}_j.$$
$$\rho^{(1)-}_{j+1/2} = -\frac{1}{6}\bar{\rho}_{j-1} + \frac{5}{6}\bar{\rho}_j + \frac{1}{3}\bar{\rho}_{j+1}; \quad \rho^{(1)+}_{j-1/2} = \frac{1}{3}\bar{\rho}_{j-1} + \frac{5}{6}\bar{\rho}_j - \frac{1}{6}\bar{\rho}_{j+1}.$$
$$\rho^{(2)-}_{j+1/2} = \frac{1}{3}\bar{\rho}_j + \frac{5}{6}\bar{\rho}_{j+1} - \frac{1}{6}\bar{\rho}_{j+2}; \qquad \rho^{(2)+}_{j-1/2} = \frac{11}{6}\bar{\rho}_j - \frac{7}{6}\bar{\rho}_{j+1} + \frac{1}{3}\bar{\rho}_{j+2}.$$

After the values $\rho^{(r),-}_{j+1/2}$ and $\rho^{(r),+}_{j-1/2},\ r = 0, 1, 2$, are determined, take a convex combination of these reconstructed values to obtain

$$\rho^-_{j+1/2} = \sum_{r=0}^{2} \omega_r \rho^{(r)-}_{j+1/2}; \quad \sum_{r=0}^{2} \omega_r = 1, \quad \text{and } \omega_r = \frac{\alpha_r}{\sum_{m=0}^{2} \alpha_m}, \quad \alpha_r = \frac{\gamma_r}{(\epsilon + \beta_r)^2},$$

$$\rho^+_{j-1/2} = \sum_{r=0}^{2} \tilde{\omega_r} \rho^{(r)+}_{j-1/2}; \quad \sum_{r=0}^{2} \tilde{\omega_r} = 1, \text{ and } \tilde{\omega_r} = \frac{\tilde{\alpha_r}}{\sum_{m=0}^{2} \tilde{\alpha_m}}, \quad \tilde{\alpha_r} = \frac{\tilde{\gamma_r}}{(\epsilon + \beta_r)^2}, \tilde{\gamma_r} = \gamma_{2-r},$$

where $\omega_r, \tilde{\omega_r} \geq 0$ are non-linear weights and γ_r are linear weights whose values are given by $\gamma_0 = \frac{1}{10}, \gamma_1 = \frac{6}{10}, \gamma_2 = \frac{3}{10}$. The terms β_r are the smoothness indicators of the stencil $S_j^{(r)}$ to measure the smoothness of the function $\rho(v, t)$ in the stencil, while $\epsilon = 10^{-6}$ is just a number to avoid the denominator to become zero. The values of smoothness indicators

are given by

$$\beta_0 = \frac{13}{12}\left(\bar{\rho}_{j-2} - 2\bar{\rho}_{j-1} + \bar{\rho}_j\right)^2 + \frac{1}{4}(\bar{\rho}_{j-2} - 4\bar{\rho}_{j-1} + 3\bar{\rho}_j)^2.$$
$$\beta_1 = \frac{13}{12}\left(\bar{\rho}_{j-1} - 2\bar{\rho}_j + \bar{\rho}_{j+1}\right)^2 + \frac{1}{4}(\bar{\rho}_{j-1} - \bar{\rho}_{j+1})^2.$$
$$\beta_2 = \frac{13}{12}\left(\bar{\rho}_j - 2\bar{\rho}_{j+1} + \bar{\rho}_{j+2}\right)^2 + \frac{1}{4}(3\bar{\rho}_j - 4\bar{\rho}_{j+1} + \bar{\rho}_{j+2})^2.$$

For the above scheme to be well defined, the ghost points are necessary at the boundary points. In this work, the values at the ghost points are zero, i.e., $\rho_j^n = 0, j = -2, -1, N+1, N+2$. The next step is to use numerical approximation for the flux function. In this study, the local Lax-Friedrichs flux is used

$$\hat{f}_{j+1/2} = F(\rho^-_{j+1/2}, \rho^+_{j+1/2}) = \frac{1}{2}\left[f^-_{j+1/2} + f^+_{j+1/2} - \alpha_{j+1/2}(\rho^+_{j+1/2} - \rho^-_{j+1/2})\right],$$

where

$$f^\pm_{j+1/2} = -\left(\frac{v_{j+1/2} - E_L}{\tau}\right)\rho^\pm_{j+1/2} \text{ and } \alpha_{j+1/2} = \left|\frac{v_{j+1/2} - E_L}{\tau}\right|.$$

In the same manner, the remaining flux term $\hat{f}_{j-1/2}$ can be defined.

It remains to define the approximation of source term. The approximation of the integral of source term is given by,

$$\bar{S}_j(t) \approx I_e(t)[\bar{\rho}_{j-m} - \bar{\rho}_j] + I_i(t)[\bar{\rho}_{j+m} - \bar{\rho}_j] + r(t)\frac{H(v_j - v_r) - H(v_{j-1} - v_r)}{\Delta v},$$

where $H(y)$ represents the Heaviside unit step function:

$$H(y) = \begin{cases} 1 & \text{if } y \geq 0; \\ 0 & \text{if otherwise.} \end{cases}$$

The numerical approximations of synaptic input rates $I_e(t)$ and $I_i(t)$, in both cases, are defined in the following manner

Case 1: With latency of synapses:

$$I_{e/i}(t) = I_{e/io}(t) + J\int_0^t \alpha(t')r(t-t')dt' \text{ and } r(t) = I_e(t)\int_{V_{th}-h}^{V_{th}} \rho(w,t)dw.$$

$$I_{e/i}(t) = I_{e/io}(t) + J\int_0^t \alpha(t')I_e(t-t')\int_{V_{th}-h}^{V_{th}} \rho(w,t-t')dt'dw,\ 0 \leq t' \leq t.$$

In particular, to discretized the excitation impulse rate $I_e(t)$ at n-th time level:

$$I_e(t_n) \approx I_{eo}(t_n) + J\Delta t\Delta v\sum_{k=0}^{n}\alpha(t_k)I_e(t_n - t_k)\sum_{i=N-m}^{N}\rho_i^{n-k},\ t_n = n\Delta t.$$

where $I_e(t_n - t_k)$ is the approximation of the excitation impulse rate $I_e(t)$ at previous time levels $\{(n-k)\Delta t, k = 0, 1, \ldots, n\}$ and the voltage of jump h consist in centre of

m-th cell.

$$I_e(t_n) = I_{eo}(t_n) + J\Delta t\Delta v\alpha(t_0)I_e(t_n)\sum_{i=N-m}^{N}\rho_i^n + J\Delta t\Delta v\sum_{k=1}^{n}\sum_{i=N-m}^{N}\alpha(t_k)I_e(t_n-t_k)\rho_i^{n-k},\ t_0=0,$$

$$I_e(t_n) = \frac{I_{eo}(t_n) + J\Delta t\Delta v\sum_{k=1}^{n}\sum_{i=N-m}^{N}\alpha(t_k)I_e(t_n-t_k)\rho_i^{n-k}}{1 - J\Delta t\Delta v\alpha(t_0)\sum_{i=N-m}^{N}\rho_i^n}, \tag{4.15}$$

and the corresponding firing rate

$$r(t) \approx I_e(t_n)\Delta v\sum_{i=N-m}^{N}\rho_i^n.$$

Similarly the inhibition impulse rate $I_i(t)$, and the corresponding firing rate $r(t)$, at n-th time level is evaluated:

$$I_i(t_n) = I_{io}(t_n) + J\Delta t\Delta v\sum_{k=0}^{n}\sum_{i=N-m}^{N}\alpha(t_k)I_e(t_n-t_k)\rho_i^{n-k}, \tag{4.16}$$

$$r(t) \approx I_i(t_n)\Delta v\sum_{i=N-m}^{N}\rho_i^n.$$

Case 2: Without latency of synapses:

$$I_e(t^n) = I_{e,o}(t^n) + JI_e(t^n)\int_{V_{th}-h}^{V_{th}}\rho(w,t^n)dw \approx \frac{I_{e,o}^n}{1 - J\Delta v\sum_{i=N-m}^{N}\rho_i^n}. \tag{4.17}$$

$$I_i(t^n) = I_{i,o}^n + Jr(t^n). \tag{4.18}$$

TVD-3rd order RK. The evolution in time is done by the 3rd-order SSP Runge-Kutta method.

$$\rho^{(1)} = \rho^{(n)} + \Delta t\tilde{L}\left(\rho^n,\ \cdot\ , t^n\right)$$
$$\rho^{(2)} = \frac{3}{4}\rho^{(n)} + \frac{1}{4}\rho^{(1)} + \frac{1}{4}\Delta t\tilde{L}\left(\rho^{(1)},\ \cdot\ , t^n + \Delta t\right)$$
$$\rho^{(n+1)} = \frac{1}{3}\rho^n + \frac{2}{3}\rho^{(2)} + \frac{2}{3}\Delta t\tilde{L}\left(\rho^{(2)},\ \cdot\ , t^n + \Delta t/2\right).$$

Here $\tilde{L}$ is the numerical approximation of the flux and the source term, i.e.

$$\tilde{L}(\rho(v,t),v,t) \approx -\frac{\partial}{\partial v}(f(\rho,v)) + S(\rho,t),$$

where Δt is the time step. Here, an explicit time-stepping scheme is used, so Δt is conditioned on the following CFL restriction: $\Delta t \le CFL\dfrac{\Delta v}{\left\|\frac{-(v-E_L)}{\tau}\right\|_\infty}$. Since WENO-FVM is high accurate approximation for the term $\tilde{L}$, the CFL condition does not yield restrictive time stepping. In the next section numerical experiments are considered for the simulation of model equation.

4 Numerical Simulation

This section introduces some test examples of the model introduced above. A comparison between the proposed scheme and upwind finite difference scheme (proposed in [56, 71] for similar type of model equation) are shown in this section. Moreover, the convergence ratios are also evaluated. All these factors are a benchmark to validate the general behavior of the model. In order to illustrate the performance of designed scheme, some numerical experiments are performed. In the first numerical experiment, the following type of initial condition is used

$$\rho_0(v) = \exp(-10(4v-2)^2). \tag{4.19}$$

Choose the parameters and function (given in Eq.(4.12)) as $\tau = 1, v_r = 0, V_{th} = 2, E_L = 0, J = 0.5, h = 0.2, \alpha(t) = \exp(-t)$. The numerical result determined by the proposed scheme at time level $t = 1.0$ is shown in Fig. 4.3. The same experiment is performed by using upwind FDM scheme which was used in [56, 71]. In Fig. 4.3, there are two curves: the blue solid curve corresponding to a WENO-FVM simulation and the red dotted curve corresponds to a upwind FDM simulation. The upper left plot of Fig. 4.3 shows the influence of excitatory input rate which is taken constant in the simulation. Since the population density becomes positive near the threshold level, and this positive value leaves the domain and is reset to the resting potential, this phenomena can be seen in all plots of Fig. 4.3, where a jump is present at the resting potential and it propagates with jump size h. The corresponding firing rate of above experiment is shown in Fig. 4.4.

The validation of the proposed scheme is shown by the convergence result. Due to the impulse reception rate (with/without latencies of synapses) the exact solution of model equation is not available. To illustrate the performance of designed scheme, we will compute $\|.\|_1, \|.\|_2$ and $\|.\|_\infty$ error norms. The error norms are defined in the following manner

$$\|.\|_1 = \Delta v \sum_{j=1}^{N} \left|(\rho_{\Delta v})_j - (\rho_{\Delta v*})_j\right|, \ \|.\|_2 = \sqrt{\Delta v \sum_{j=1}^{N} \left|(\rho_{\Delta v})_j - (\rho_{\Delta v*})_j\right|^2},$$

$$\|.\|_\infty = \max_j \left|(\rho_{\Delta v})_j - (\rho_{\Delta v*})_j\right|,$$

where $\rho_{\Delta v}$ is the approximated solution with step size Δv and $\rho_{\Delta v*}$ is the numerical solution calculated from the finest grid with step size $\Delta v* = \frac{1}{640}$. In this work, the approach for error-norms is based on [134]. The order of accuracy is obtained from the following ratio $\|\rho_{\Delta v} - \rho_{\Delta v*}\|/\|\rho_{\Delta v/2} - \rho_{\Delta v*}\|$. If the ratio approaching the number $2, 5$ and 9, it would indicate the order of convergence $1, 2$ and 3 respectively. The $\|.\|_1, \|.\|_2$

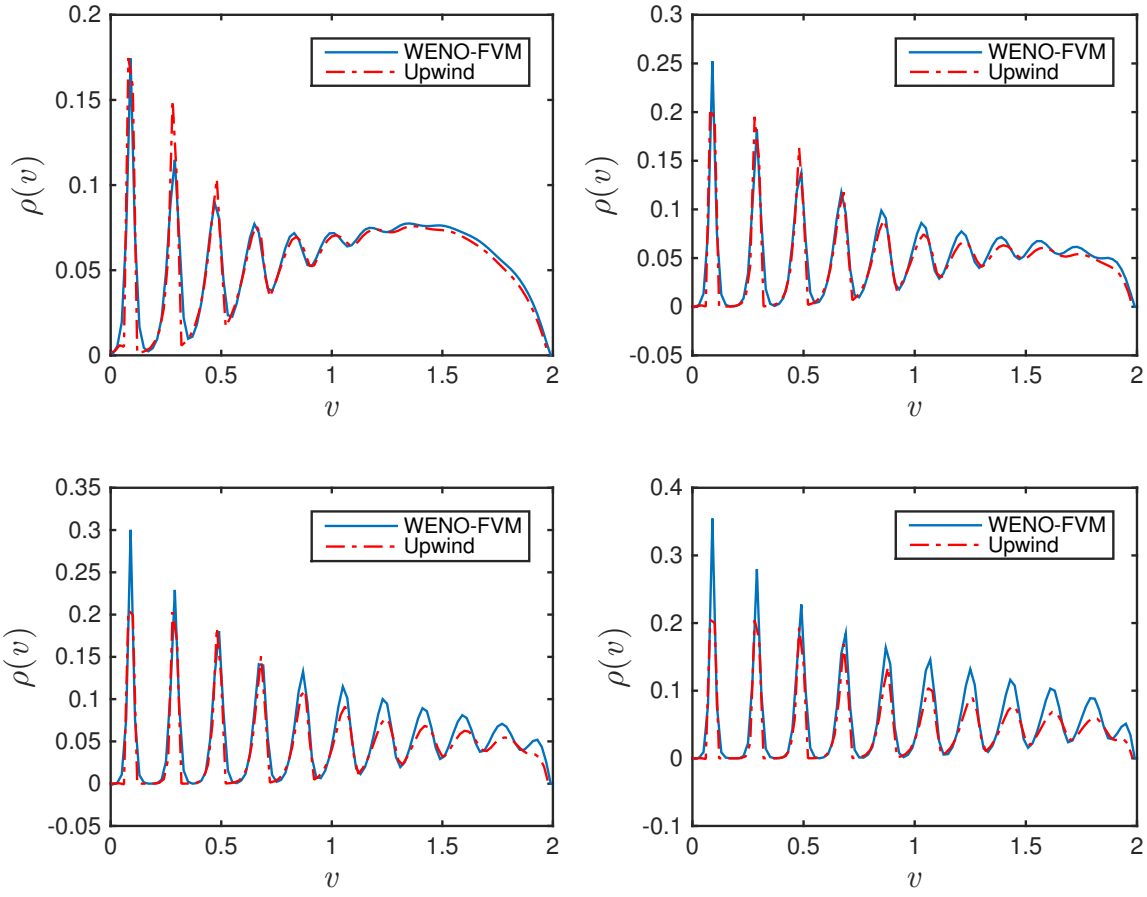

Figure 4.3: The approximate solution of Eqs. (4.12)-(4.13) that represents the physical phenomena of excitatory neuron population. Top left: external excitation input $I_{e,o} = 20$ units. Top right: $I_{e,o} = 40$ units. Bottom left: $I_{e,o} = 60$ units. Bottom right: $I_{e,o} = 80$ units. The representation of ρ is evaluated at time $t = 1$ unit with 100 grid cells. The external inhibition input $I_{i,o} = 5$ unit is fixed for all subplots.

and $\|.\|_\infty$ norms for ρ have been computed by WENO-FVM and upwind-FVM scheme at time t=1.0 (see Tables 4.1-4.2). Table 4.1 shows that the proposed scheme is of order 3 in space for the considered problem while the upwind scheme is of order 1 in space. The L_1 error norm ($\|.\|_1$) of ρ as a function of resolution for WENO-FVM (star line) and upwind (triangle line) schemes are shown in Fig. 4.5. The result shows the advantages of the proposed scheme over existing scheme in the literature.

The second numerical experiment is chosen to demonstrate the inhibitory phenomena. In this experiment, the initial condition is chosen of the following type

$$\rho_0(v) = \frac{e^{-(v-\bar{h})^2}}{2\alpha^2}, \ \bar{h} = 0.03 \text{ and } \alpha = 0.3\bar{h}, \tag{4.20}$$

and with the same parameters and function as defined in the first experiment. But in

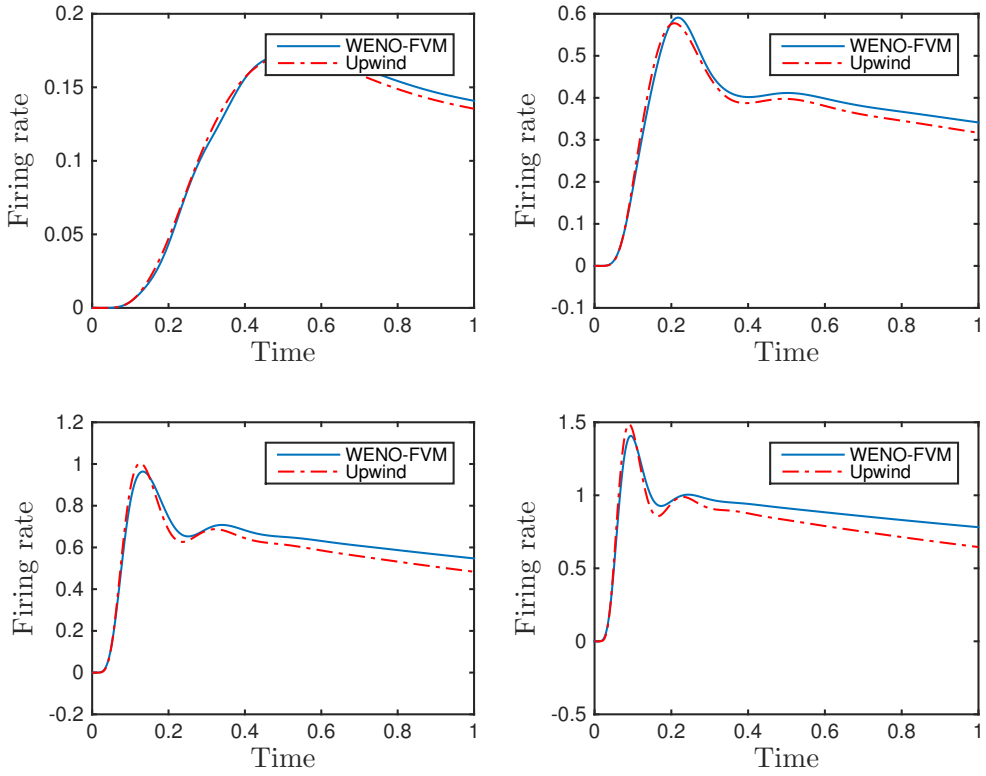

Figure 4.4: Firing rate $r(t)$. Top left: external excitation input $I_{e,o} = 20$ units with same initial data as described in Eq. (4.19) and external inhibition input $I_{i,o} = 5$ units. Top right: $I_{e,o} = 40$ units. Bottom left: $I_{e,o} = 60$ units. Bottom right: $I_{e,o} = 80$ units.

this experiment, the frequency of inhibitory input rate increased instead of excitatory input rate. Fig. 4.6 depicts that the neuron's movement (jumps) is very slow compare to the excitatory phenomena. The upper part of the simulation is done by WENO-FVM scheme while lower part of the simulation is done by upwind scheme. The corresponding firing rate of the inhibitory neuron population is displayed in Fig. 4.7.

4.1 Diffusion Approximation

In this subsection, we present the comparison between the model for a neuron population with voltage jumps and it's diffusion approximation for small values of h. For this purpose, we remove the nonlocal terms, $\rho(v-h,t)$, $\rho(v+h,t)$, from model Eq. (4.12).
Assume that h is very small, then

$$\rho(v-h,t) - \rho(v,t) \approx -h\frac{\partial \rho(v,t)}{\partial v} + \frac{h^2}{2}\frac{\partial^2 \rho(v,t)}{\partial v^2},$$

N	$\|.\|_1$	r	$\|.\|_2$	r	$\|.\|_\infty$	r
20	$2.08e-02$	$-$	$3.231e-02$	$-$	$1.35e-01$	$-$
40	$2.54e-03$	8.18	$4.03e-03$	8.43	$1.46e-02$	9.21
80	$3.40e-04$	7.47	$5.03e-04$	8.01	$1.91e-03$	7.65
160	$4.21e-05$	8.08	$6.78e-05$	7.43	$2.69e-04$	7.10

Table 4.1: Error norms of Experiment 1 using WENO-FVM at time t=1.0.

N	$\|.\|_1$	r	$\|.\|_2$	r	$\|.\|_\infty$	r
20	$9.02e-02$	$-$	$8.31e-02$	$-$	$9.75e-01$	$-$
40	$3.02e-02$	2.98	$2.76e-02$	3.01	$4.62e-01$	2.11
80	$1.23e-02$	2.45	$9.55e-03$	2.89	$2.76e-01$	1.67
160	$6.14e-03$	2.01	$4.50e-03$	2.12	$1.43e-04$	1.93

Table 4.2: Error norms of Experiment 1 using upwind FDM at time t=1.0.

$$\rho(v+h,t)-\rho(v,t)\approx h\frac{\partial\rho(v,t)}{\partial v}+\frac{h^2}{2}\frac{\partial^2\rho(v,t)}{\partial v^2},$$

$$\int_{v_{th-h}}^{V_{th}}\rho(w,t)dw\approx\rho(V_{th},t)-\frac{h}{2}\frac{\partial\rho(V_{th},t)}{\partial v}=-\frac{h}{2}\frac{\partial\rho(V_{th},t)}{\partial v}.$$

Putting these expressions in Eq. (4.12) and obtain

$$\frac{\partial\rho(v,t)}{\partial t}+\frac{\partial}{\partial v}\left[-\frac{(v-E_L)}{\tau}+h(I_e-I_i)\right]\rho(v,t)-\frac{h^2}{2}(I_e+I_i)\frac{\partial^2\rho(v,t)}{\partial v^2}=\delta(v-v_R)r(t).$$

$I_{e/i}(t)=I_{e/io}(t)+J\int_0^t\alpha(u)r(t-u)du$ with conduction delay.

$I_{e/i}(t)=I_{e/io}(t)+Jr(t)$ without conduction delay.

$$r(t)=I_e-\frac{h}{2}\frac{\partial\rho(V_{th},t)}{\partial v}.$$

For the simulation of diffusion approximation, Strang splitting scheme [168] based on WENO-finite volume approximation is used. Figs. (4.8-4.9) display the results of diffusion approximation corresponding to same data that are used for Figs. (4.3-4.4), respectively. The results obtained from diffusion approximation removes the oscillation due to the jump effect at low potential but nevertheless it provides a good simulation of excitatory and inhibitory population neuron model.

Up to now, the impulse (excitatory/inhibitory) reception rate without latencies of synapses, given in Eqs.(4.17)-(4.18), are taken for simulation.

We consider, the impulse (excitatory/inhibitory) reception rate with latencies of synapses given in Eqs. (4.19)-(4.20). To see the effect of these terms, the same data has been used as given in the first experiment except the domain. The results are displayed in Fig. 4.10. Examination of Fig. 4.10 shows that the effect of latencies of synapses on the neuron's

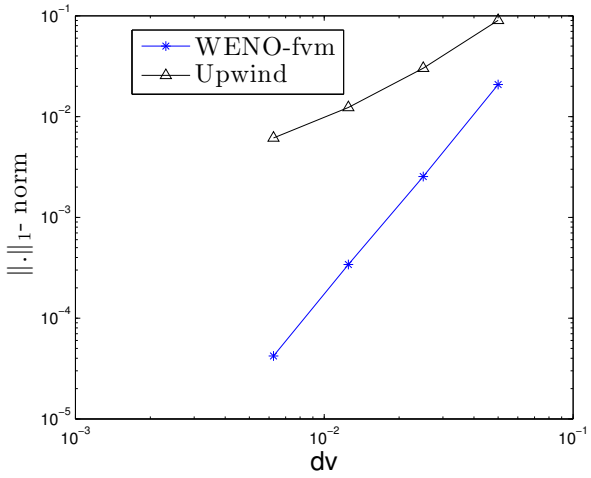

Figure 4.5: $\|.\|_1$ of ρ as a function of resolution for Experiment 1.

firing is almost same as the case of without latencies of synapses.

5 Summary

In this chapter, the excitatory and inhibitory neuron population model has been studied. Initiated with a leaky integrate-and-fire neuron model that describes the dynamics of a single neuron and then with the help of population density approach, we derive a partial differential equation for the whole population with or without latencies of synapses. The resulting model equation is approximated by WENO-FVM and SSP Runge-Kutta scheme. The numerical results revealed that the present scheme is an efficient, reliable, and of high accuracy for simulating the dynamics of a population of excitatory and inhibitory neurons. In order to validate the proposed scheme, some test examples are taken, which are also solved using existing schemes of similar type of model equation [56, 71], and the results are compared. The order of convergence revealed that the proposed scheme is better than the existing scheme. Moreover, the comparison between the original model and the model determined with the diffusion approximation have been shown.

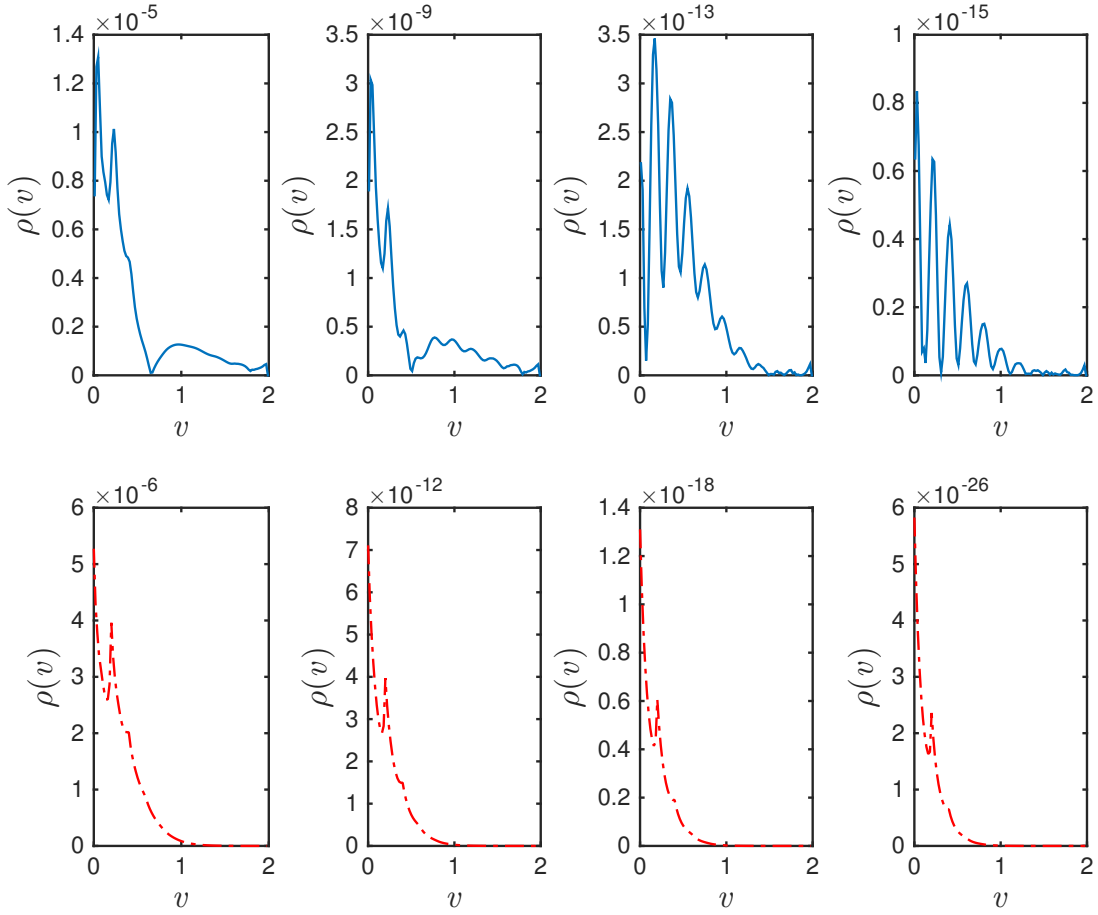

Figure 4.6: The approximate solution of Eq. (4.12) that represents the physical phenomena of inhibitory neuron population. All plotted figures in upper part are made by WENO-FVM approximation while lower plots are made by upwind scheme scheme. The initial data (given in Eq. 4.20) with external excitation input rate $I_{e,o} = 5$ unit is used for this figure. An external inhibitory input rate in first plot: $I_{i,o} = 20$ units. Second plot: $I_{i,o} = 40$ units. Third plot: $I_{i,o} = 60$ units. Fourth plot: $I_{i,o} = 80$ units.

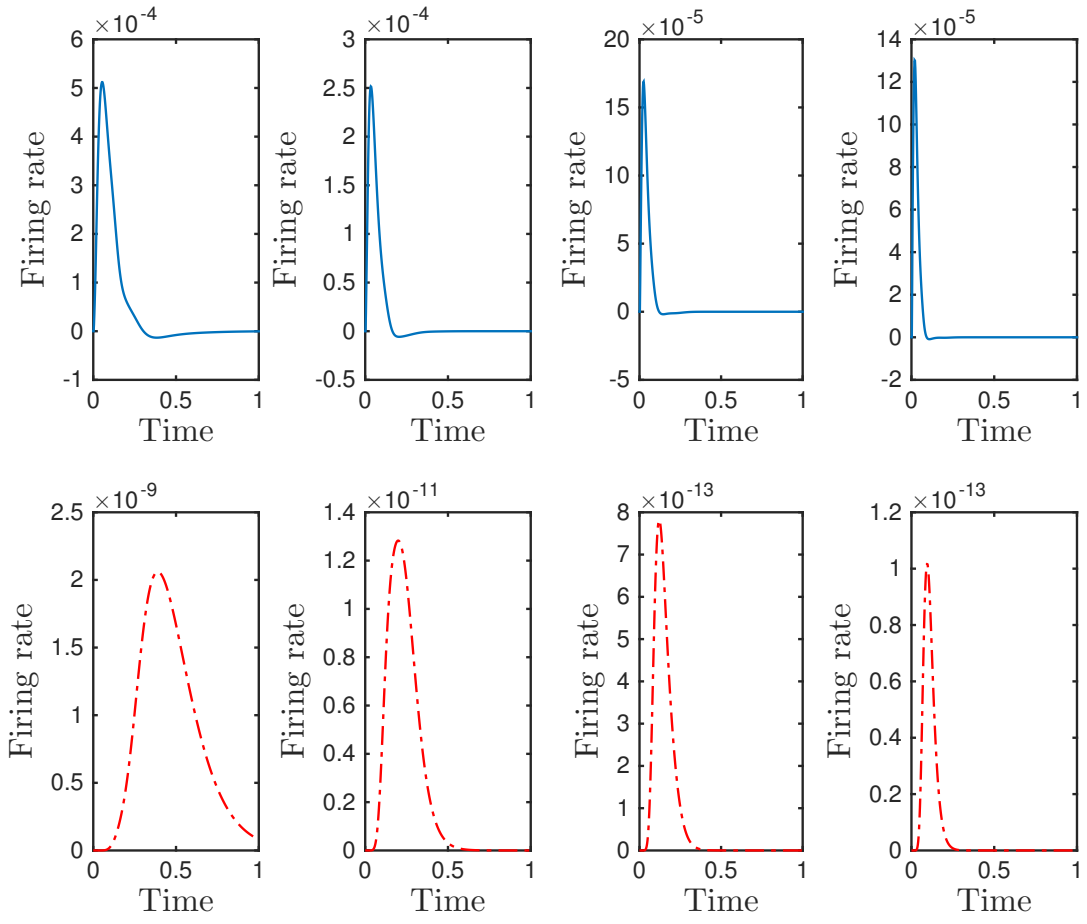

Figure 4.7: Firing rate $r(t)$. The graph displays the firing rate of inhibition corresponding to the external inhibition inputs, $I_{i,o} = 20, 40, 60, 80$ units with same initial data as described in Eq. (4.20). The upper part of the graph is done by WENO-FVM while lower part is done by upwind scheme.

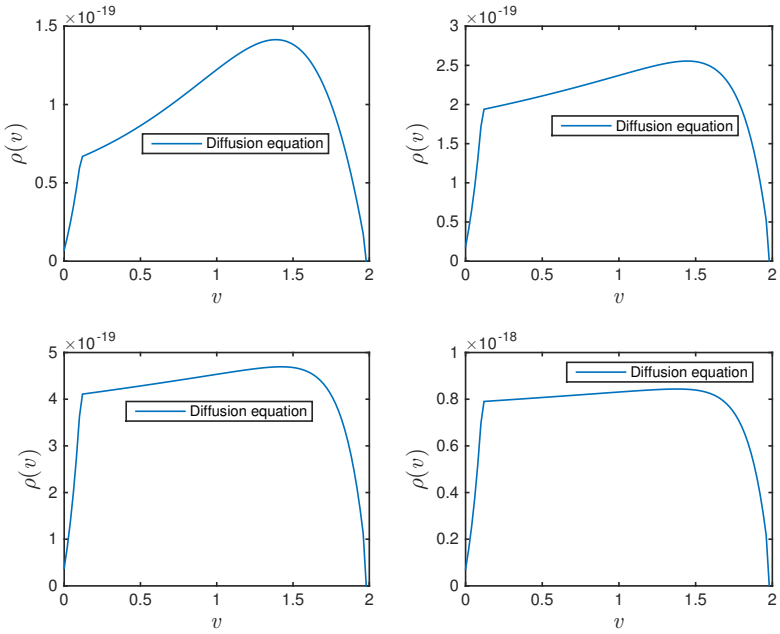

Figure 4.8: The diffusion approximation for the excitatory neural networks phenomena. The parameters and function are same as used for the simulation of Fig. chapter4:fig3.

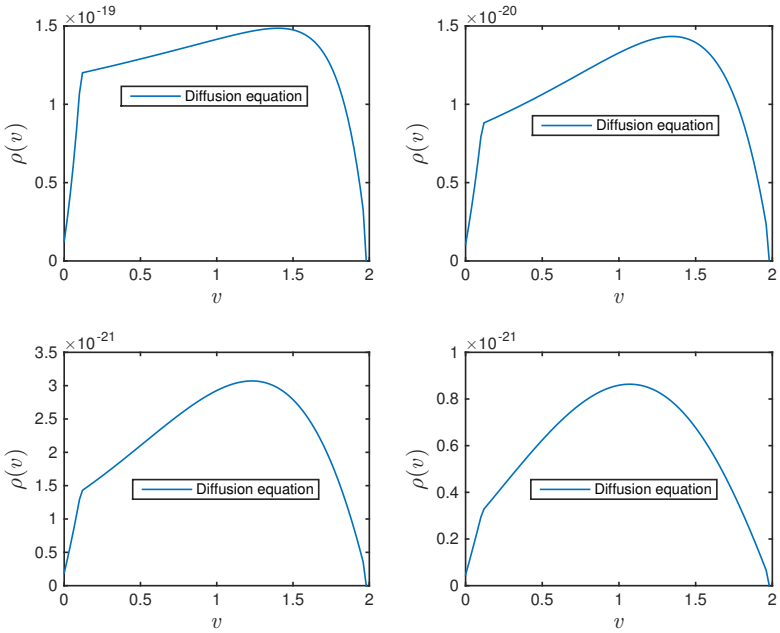

Figure 4.9: The diffusion approximation for the inhibitory neural networks phenomena. The parameters and function are same as used for the simulation of Fig. chapter4:fig6 .

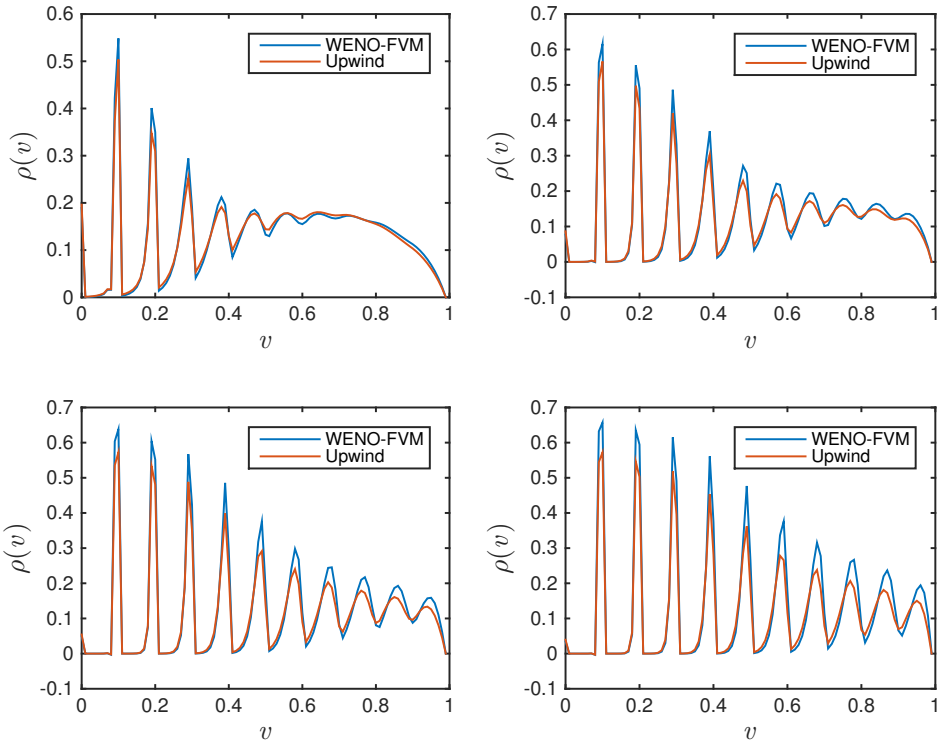

Figure 4.10: The simulation of excitatory population neuron model under the influence of excitatory reception rate $I_e(t)$ in case of conduction delay.

Chapter 5

Numerical Solver of Size Structured Neuron Model [4]

This chapter and subsequent chapter deals with the numerical study of structured population dynamics where the structure leads to a partial differential equation. The current chapter deals with the age size-structured neuron population model which characterizes the evolution of the density of nerve cells that grow and divide. Two numerical schemes based on finite volume method are used to find the approximate solution of governing partial differential equation. The proposed numerical schemes are analyzed for consistency, stability, and convergence. Some numerical examples are tested to show the performance of designed schemes.

1 Introduction

Various mathematical models for biological neurons have been developed to represent their biological activities. Size is usually a better physiological trait to structure nerve cell populations. Consider the size-structured population density model

$$\begin{cases} \dfrac{\partial p(s,t)}{\partial t} + \dfrac{\partial (g(s)p(s,t))}{\partial s} + B(s)p(s,t) = 4B(2s)p(t,2s), (s,t) \in \mathbb{R} \times \mathbb{R}_+ \\ \qquad\qquad p(s=0,t) = 0; \qquad p(0,s) = p^0(s) \in L^1(R^+). \end{cases}$$

- Here $p(s,t)$ denotes the population density of cells of size 's' at time 't'.
- $g(s)$ is the growth rate of individuals at size s.
- $B(.)$ is the cell-division rate.
- $\dfrac{\partial}{\partial s} g(s)p(s,t)$ represents the growth of nerve cells by using the external input.
- $B(s)$ and $B(2s)$ describe the division of cells of size $2s$ into two cells of size s.

[4] Santosh Kumar, Paramjeet Singh *"Finite volume approximation for age size structured neuron model"*, Differential Equations and Dynamical Systems, 25 (02) , Springer, 251-265, (2017).

This model appears in many areas, for example, in physics, it represents a fragmentation (degradation) phenomenon in polymer, and in telecommunication, it describes some internet protocols. Many variants of the above model are possible (see for example [99, 169–176] and references therein).

The dynamics of above model is characterized by the total biomass, $M(t) = \int_0^\infty sp(s,t)ds$, and the total number of cells $N(t) = \int_0^\infty p(s,t)ds$, which increase only by external input cells and the division of cells, respectively. This chapter focuses only on the second case, i.e., the number of cells increase due to the division of the cells. For this reason, we take $g(s) = 1$ in the above equation

$$\begin{cases} \dfrac{\partial p(s,t)}{\partial t} + \dfrac{\partial p(s,t)}{\partial s} + B(s)p(s,t) = 4B(2s)p(t,2s), (s,t) \in \mathbb{R} \times \mathbb{R}_+, \\ \qquad\qquad p(s=0,t) = 0, \qquad p(0,s) = p^0(s) \in L^1(R^+). \end{cases} \tag{5.1}$$

The above equation represents the size-structure of the population of nerve cells. The analytical solution of governing equation cannot be easily calculated because the governing equation consists variable coefficients. Therefore, numerical schemes are usually used to solve the governing equation. Here, numerical schemes are based on finite volume approximation, which are widely applicable to understand the behavior of model equation. In the next section, numerical schemes are designed to solve the above Eq. (5.1).

2 Numerical Techniques

In this section, the numerical schemes based on finite volume of type upwind and Lax-Wendroff are designed. Since the spatial domain of governing equation is infinite, thus the actual domain is normalized into a finite domain, namely $[a, b]$, to find the approximate solution of Eq. (5.1).

Upwind Finite Volume Approximation: Discretize the spatial domain into grid cells/control volumes,

$$D = \cup_{j=1}^{N}(s_{j-1/2}, s_{j+1/2}), s_{1/2} = a,\ s_{N+1/2} = b,\ \Delta s = s_{j+1/2} - s_{j-1/2},$$
$$s_j = \frac{1}{2}(s_{j-1/2} + s_{j+1/2}).$$

Rewrite Eq. (5.1) in standard form

$$\partial_t p(s,t) + \partial_s f(p(s,t)) = S(p,s). \tag{5.2}$$

Here, $f(p(s,t)) = p(s,t)$ is a flux function and $S(p,s)$ is a source term. Integrating Eq. (5.2) over any finite grid cell $(s_{j-\frac{1}{2}}, s_{j+\frac{1}{2}})$, from time level t^n to t^{n+1}, we obtain

$$\int_{t^n}^{t^{n+1}} \int_{s_{j-1/2}}^{s_{j+1/2}} \partial_t p(s,t)\, ds\, dt + \int_{t^n}^{t^{n+1}} \int_{s_{j-1/2}}^{s_{j+1/2}} \partial_s f(p(s,t))\, ds\, dt = \int_{t^n}^{t^{n+1}} \int_{s_{j-1/2}}^{s_{j+1/2}} S(p,s) ds\, dt,$$

and on using Fundamental Theorem of Calculus, we have

$$\int_{s_{j-1/2}}^{s_{j+1/2}} p(s,t^{n+1}) ds - \int_{s_{j-1/2}}^{s_{j+1/2}} p(s,t^n) ds + \int_{t^n}^{t^{n+1}} f(p(s_{j+1/2},t)) dt - \int_{t^n}^{t^{n+1}} f(p(s_{j-1/2},t)) dt$$
$$= \Delta t\ \Delta s\ S_j^n.$$

We now define the approximate value of the cell average of $p(s,t)$ over j^{th} grid cell and flux function over $[t^n.t^{n+1})$

$$\bar{p}_j^n = \frac{1}{\Delta s} \int_{s_{j-1/2}}^{s_{j+1/2}} p(s,t^n) ds, \text{ and } F_{j+1/2}^n = \frac{1}{\Delta t} \int_{t^n}^{t^{n+1}} f(p(s_{j+1/2},t))\, dt.$$

Dividing both sides of the above equation by Δs, to obtain

$$\therefore (\bar{p}_j^{n+1} - \bar{p}_j^n)\Delta s + (F_{j+\frac{1}{2}}^n - F_{j-\frac{1}{2}}^n)\Delta t = \Delta t S(\bar{p}_j^n).$$

$$\implies (\bar{p}_j^{n+1} - \bar{p}_j^n)\Delta s + (\bar{p}_j^n - \bar{p}_{j-1}^n)\Delta t = \Delta t S_j^n.$$

$$\implies \bar{p}_j^{n+1} = \bar{p}_j^n - \frac{\Delta t}{\Delta s}(\bar{p}_j^n - \bar{p}_{j-1}^n) + \Delta t S_j^n. \tag{5.3}$$

It can be clearly seen that this scheme is consistent and conservative.

Lax-Wendroff Finite Volume Approximation: The numerical flux in this approximation is

$$F_{j+1/2}^n = \frac{1}{2}(\bar{p}_{j+1}^n + \bar{p}_j^n) - \frac{1}{2}(\bar{p}_{j+1}^n - \bar{p}_j^n).$$

Thus the final approximation for Eq. (5.2) is

$$\bar{p}_j^{n+1} = \bar{p}_j^n - \frac{1}{2}\left(\frac{\Delta t}{\Delta s}\right)(\bar{p}_{j+1}^n - \bar{p}_{j-1}^n) + \frac{1}{2}\left(\frac{\Delta t}{\Delta s}\right)^2 (\bar{p}_{j-1}^n - 2\bar{p}_j^n + \bar{p}_{j+1}^n) + \Delta t S_j^n. \tag{5.4}$$

This scheme is also conservative and consistent for the given Eq. (5.2).

3 Consistency, Stability and Convergence

This section focuses on the consistency, stability and convergence of the above schemes. **Consistency:** A general explicit scheme can be written as $\mathsf{A}^{n+1} = \mathsf{B}(A^n)$. Where $\mathsf{B}(.)$ represent the numerical operator which map the numerical solution at one time step to the next time step. One step error is defined by $\mathsf{B}(\mathsf{A}^n) - \bar{p}^{n+1}$ and the local truncation error is defined by

$$\tau^n = \frac{1}{\Delta t}[\mathsf{B}(\mathsf{A}^n) - \bar{p}^{n+1}].$$

Upwind Scheme: The local truncation error for the upwind scheme is defined as

$$\tau^n = \frac{1}{\Delta t}\left[p(s_j,t_n) - \frac{\Delta t}{\Delta s}(p(s_j,t_n) - p(s_{j-1},t_n)) + \Delta t S(p(s_j,t_n)) - p(s_j,t_{n+1})\right].$$

Expand $p(s_{j-1},t_n)$ and $p(s_j,t_{n+1})$ in Taylor series

$$\tau^n = \frac{1}{\Delta t}[p(s_j,t_n) - \frac{\Delta t}{\Delta s}\left(p(s_j,t_n) - [p(s_j,t_n) - \Delta s p_s(s_j,t_n) + \frac{(\Delta s)^2}{2}p_{ss}(s_j,t_n)\cdots]\right)$$
$$+ \Delta t S(p(s_j,t_n)) - p(s_j,t_n) + \Delta t p_t(s_j,t_n) - \frac{(\Delta t)^2}{2}p_{tt}(s_j,t_n)].$$

Simplying and obtain

$$\tau^n = \frac{1}{\Delta t}\left[-\Delta t p_s(s_j,t_n) - \Delta t p_t(s_j,t_n) + \Delta t(S(p_j^n)) + \frac{\Delta t \Delta s}{2}p_{ss}(s_j,t_n) - \frac{(\Delta t)^2}{2}p_{tt}(s_j,t_n)\right].$$
$$\tau^n = \frac{1}{\Delta t}\left[0 + \frac{\Delta t \Delta s}{2}p_{ss}(s_j,t_n) - \frac{(\Delta t)^2}{2}p_{tt}(s_j,t_n) + O(\Delta t)^2\right].$$
$$\tau^n = \frac{1}{2}\Delta s\left(1 - \frac{\Delta t}{\Delta s}\right)p_{ss}(s_j,t_n) + O(\Delta t)^2.$$

Thus $\tau^n \to 0$ as $\Delta s, \Delta t \to 0$. Hence the given scheme is consistent with the given partial differential Eq. (5.2).

The Lax-Wendroff Scheme: The local truncation error is defined as

$$\tau^n = \frac{1}{\Delta t}[p(s_j,t_n) - \frac{1}{2}\frac{\Delta t}{\Delta s}(p(s_{j+1},t_n) - p(s_{j-1},t_n))$$
$$+ \frac{1}{2}\left(\frac{\Delta t}{\Delta s}\right)^2(p(s_{j-1},t_n) - 2p(s_j,t_n) + p(s_{j+1},t_n)) + \Delta t S(p_j^n) - p(s_j,t_{n+1})].$$

Expanding the terms the $p(s_{j+1},t_n)$, $p(s_{j-1},t_n)$, and $p(s_j,t_{n+1})$ in Taylor series, to get

$$\tau^n = \frac{1}{\Delta t}\left[p(s_j,t_n) - \frac{1}{2}\frac{\Delta t}{\Delta s}\left(p(s_j,t_n) + \Delta s p_s(s_j,t_n) + \frac{(\Delta s)^2}{2}p_{ss}(s_j,t_n)\right.\right.$$
$$\left.\left. + \frac{(\Delta s)^3}{6}p_{sss}(s_j,t_n)\cdots\right) - \frac{1}{2}\frac{\Delta t}{\Delta s}\left(-p(s_j,t_n) + \Delta s p_s(s_j,t_n) - \frac{(\Delta s)^2}{2}p_{ss}(s_j,t_n)\right.\right.$$

$$+\frac{(\Delta s)^3}{6}p_{sss}(s_j,t_n)\Big)+\frac{1}{2}\left(\frac{\Delta t}{\Delta s}\right)^2(p(s_j,t_n)-\Delta s p_s(s_j,t_n)+\frac{(\Delta s)^2}{2}p_{ss}(s_j,t_n)$$
$$-\frac{(\Delta s)^3}{6}p_{sss}(s_j,t_n)-2p(s_j,t_n)+p(s_j,t_n)+\Delta s p_s(s_j,t_n)+\frac{(\Delta s)^2}{2}p_{ss}(s_j,t_n)$$
$$+\frac{(\Delta s)^3}{6}p_{sss}(s_j,t_n))+\Delta t S(p(s_j,t_n))-p(s_j,t_n)-\Delta t p_t(s_j,t_n)-\frac{(\Delta t)^2}{2}p_{tt}(s_j,t_n)$$
$$-\frac{(\Delta t)^3}{6}p_{ttt}(s_j,t_n)+\cdots\Big].$$

$$\tau^n=\frac{1}{\Delta t}\left[-\frac{\Delta t}{\Delta s}\left(\Delta s p_s(s_j,t_n)+\frac{(\Delta s)^3}{6}p_{sss}(s_j,t_n)\right)+\left(\frac{\Delta t}{\Delta s}\right)^2\left(\frac{(\Delta s)^2}{2}p_{ss}(s_j,t_n)\right)\right.$$
$$\left.+\Delta t S(p(s_j,t_n))-\Delta t p_t(S_j,t_n)-\frac{(\Delta t)^2}{2}p_{tt}(s_j,t_n)-\frac{(\Delta t)^3}{6}p_{ttt}(s_j,t_n)\cdots\right].$$

$$\tau^n=\frac{1}{\Delta t}\left[-\Delta t\left(p_s(s_j,t_n)+\frac{(\Delta s)^2}{6}p_{sss}(s_j,t_n)\right)+\frac{(\Delta t)^2}{2}p_{ss}(s_j,t_n)\right.$$
$$\left.+\Delta t S(p(s_j,p_n))-\Delta_t p_t(s_j,p_n)-\frac{(\Delta t)}{2}p_{tt}(s_j,t_n)-\frac{(\Delta t)^2}{6}p_{ttt}(s_j,t_n)\right].$$

$$\Rightarrow\tau^n=-\frac{(\Delta s)^2}{6}p_{sss}(s_j,t_n)+\frac{\Delta t}{2}p_{ss}(s_j,t_n)-\frac{\Delta t}{2}p_{tt}(s_j,t_n)-\frac{(\Delta t)^2}{6}p_{ttt}(s_j,t_n).$$

Thus,

$$\tau^n=-\frac{1}{6}(\Delta s)^2\left(1-\left(\frac{\Delta t}{\Delta s}\right)^2\right)p_{sss}(x_s,t_n)+O(\Delta t)^3.$$

Hence, $\tau^n\to 0$ as $\Delta s\to 0,\ \Delta t\to 0$. Hence the scheme is consistent.

Remark. Since the Lax-Wendroff method is second-order accurate and the dominant term depends on the third derivative of p, whereas the upwind are first order accurate with dominant error depending on the second derivative of p.

Stability. Next step is to discuss the stability of an upwind approximation and Lax-Wendroff approximation in the l_1-norm under the time step restriction.

Theorem 3.1. *Under the condition $k\Delta t<1$ (k is the Lipschitz constant), the upwind and Lax-Wendroff schemes satisfy the following inequality*

$$\|p^{n+1}\|_1\le C\|p^n\|.$$

Proof. Since the upwind scheme for Eq. (5.1) is

$$\bar{p}_j^{n+1}=\bar{p}_j^n-\frac{\Delta t}{\Delta s}(\bar{p}_j^n-\bar{p}_{j-1}^n)+\Delta t S(\bar{p}_j^n)=\left(1-\frac{\Delta t}{\Delta s}\right)p_j^n+\frac{\Delta t}{\Delta s}p_{j-1}^n+\Delta t S(p_j^n).$$
$$\|\bar{p}^{n+1}\|_{L^1}=\Delta s\sum_j|\bar{p}_j^{n+1}|=\Delta s\sum_j\left|\left(1-\frac{\Delta t}{\Delta s}\right)\bar{p}_j^n+\frac{\Delta t}{\Delta s}\bar{p}_{j-1}^n+\Delta t S_j^n\right|,$$
$$\le\left(1-\frac{\Delta t}{\Delta s}\right)\Delta s\sum_j|\bar{p}_j^n|+\frac{\Delta t}{\Delta s}\Delta s\sum_j|\bar{p}_{j-1}^n|+\Delta t\Delta s\sum_j|S_j^n|,$$

$$\leq \left(1-\frac{\Delta t}{\Delta s}\right)\|\bar{p}^n\|_{L^1}+\frac{\Delta t}{\Delta s}\|\bar{p}^n\|_{L^1}+k\Delta t\|\bar{p}^n\|_{L^1}\leq \|\bar{p}^n\|_{L^1}+\|\bar{p}^n\|_{L^1},$$
$$= C\|\bar{p}^n\|_{L^1}.$$

Hence the inequality is proved for the upwind approximation.

Since the Lax-wendroff approximation for Eq. (5.1) is

$$\bar{p}_j^{n+1}=\bar{p}_j^n-\frac{1}{2}\left(\frac{\Delta t}{\Delta s}\right)(\bar{p}_{j+1}^n-\bar{p}_{j-1}^n)+\frac{1}{2}\left(\frac{\Delta t}{\Delta s}\right)^2(\bar{p}_{j-1}^n-2\bar{p}_j^n+\bar{p}_{j+1}^n)+\Delta t S_j^n.$$

$$\|\bar{p}^{n+1}\|_{L^1}=\Delta s\sum_j|\bar{p}_j^{n+1}|=\Delta s\sum_j\Bigg|\bar{p}_j^n-\frac{1}{2}\left(\frac{\Delta t}{\Delta s}\right)\bar{p}_{j+1}^n+\frac{1}{2}\left(\frac{\Delta t}{\Delta s}\right)\bar{p}_{j-1}^n+\frac{1}{2}\left(\frac{\Delta t}{\Delta s}\right)^2\bar{p}_{j-1}^n,$$
$$-\left(\frac{\Delta t}{\Delta s}\right)^2\bar{p}_j^n+\frac{1}{2}\left(\frac{\Delta t}{\Delta s}\right)^2\bar{p}_{j+1}^n+\Delta t S_j^n\Bigg|,$$
$$=\Delta s\sum_j\Bigg|\left(1-\left(\frac{\Delta t}{\Delta s}\right)^2\right)\bar{p}_j^n+\frac{1}{2}\frac{\Delta t}{\Delta s}\left(1+\frac{\Delta t}{\Delta s}\right)\bar{p}_{j-1}^n-\frac{1}{2}\frac{\Delta t}{\Delta s}\left(1-\frac{\Delta t}{\Delta s}\right)\bar{p}_{j+1}^n,$$
$$+\Delta t S_j^n\Bigg|,$$
$$\leq\left(1-\left(\frac{\Delta t}{\Delta s}\right)^2\right)\Delta s\sum_j|\bar{p}_j^n|+\frac{1}{2}\frac{\Delta t}{\Delta s}\left(1+\frac{\Delta t}{\Delta s}\right)\Delta s\sum_j|\bar{p}_{j-1}^n|-\frac{1}{2}\frac{\Delta t}{\Delta s}\left(1-\frac{\Delta t}{\Delta s}\right)$$
$$\sum_j|\bar{p}_{j+1}^n|+\Delta t\Delta s\sum_j|S_j^n|,$$
$$\leq\left(1-\left(\frac{\Delta t}{\Delta s}\right)^2\right)\|\bar{p}^n\|_{L^1}+\frac{1}{2}\frac{\Delta t}{\Delta s}\left(1+\frac{\Delta t}{\Delta s}\right)\|\bar{p}^n\|_{L^1}-\frac{1}{2}\frac{\Delta t}{\Delta s}\left(1-\frac{\Delta t}{\Delta s}\right)\|\bar{p}^n\|_{L^1}$$
$$+k\Delta t\|\bar{p}^n\|_{L^1},$$
$$=\left(2+\frac{1}{2}\left(\frac{\Delta t}{\Delta s}\right)^2\right)\|\bar{p}^n\|_{L^1}\leq C'\|\bar{p}^n\|_{L^1},\ \text{since } k\Delta t<1,\quad 0\leq\frac{\Delta t}{\Delta s}\leq 1.$$

Because both the schemes (upwind and Lax-wendroff) are consistent and stable, hence, they are convergent (by Lax-Equivalence theorem).

In the subsequent section, we take some applications of the above model problem.

4 Numerical Experiments

In this section, some numerical experiments are presented to show the performance of the developed schemes. Since exact solution of the governing equation is not available, so errors are calculated through refining the grids. Using the half mesh principle, the

absolute error is defined as

$$\text{Abs Er} = \max_{s \in D^N} |p_j^N - p_j^{2N}|,$$

where p_j^N and p_j^{2N} are computed solutions by taking N and $2N$ grid cells, respectively.

Example 1. Consider Eq. (5.1) and assume that the cell-division rate is constant, i.e., $B(s) = 1$.
Initial and boundary conditions are given by

$$p_0(s) = e^{-10(4s-1)^2}, \quad p(s,0) = 0, \qquad s \in [-\delta, 0] \cup [2, 2+\delta].$$

The numerical solution $p(s,t)$ otained by upwind finite volume approximation at time

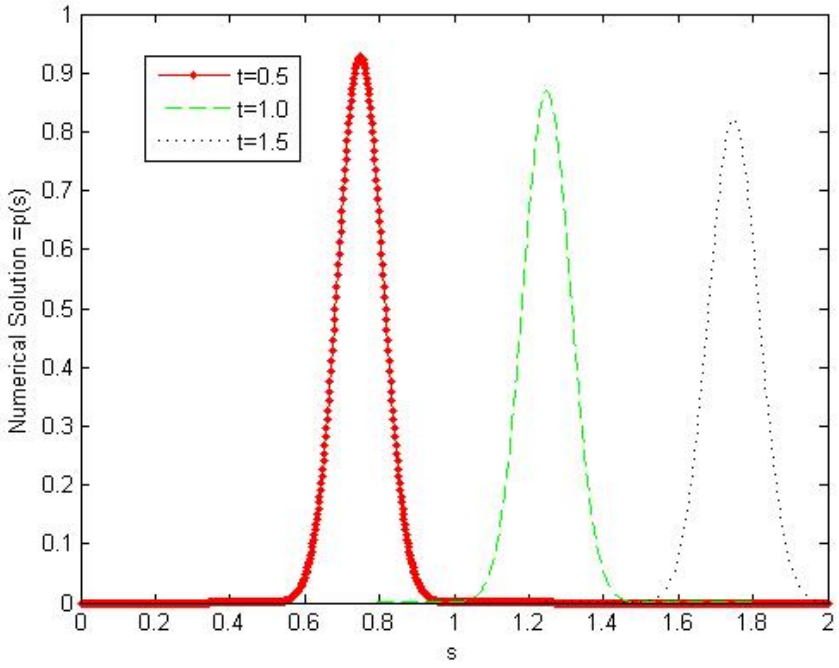

Figure 5.1: Numerical solution $p(s,t)$ of Example 1 at different time level by upwind scheme.

point $t = 0.5, t = 1.0$ and $t = 1.5$ are shown in Fig. 5.1, where time step $\Delta t = 0.1$ and space step $\Delta v = 0.2$. We notice from Fig. 5.1, as time increases the impulse size gradually decreases and move towards on the right side.

The numerical solution $p(s,t)$ generated by **Lax-Wendroff** finite volume approximation at different time level $t = 0.5, t = 1.0$ and $t = 1.5$ are displayed in Fig. 5.2. The time-step and mesh-step are same as taken in the simulation of an upwind scheme. In Fig. 5.2, as time increases the impulse size remains same. From Fig. 5.3, it is clear that as time

The Maximum Absolute Error					
$\Delta t \downarrow$	$\Delta s \rightarrow$	1/200	1/400	1/800	1/1600
$\Delta s/2$		0.054246	0.027123	0.013561	0.006781
$\Delta s/4$		0.027155	0.013578	0.006789	0.003394
$\Delta s/8$		0.013564	0.006782	0.003391	0.001695
$\Delta s/16$		0.006782	0.003391	0.001695	0.000848

Table 5.1: Error table of Example 1 based on the upwind scheme.

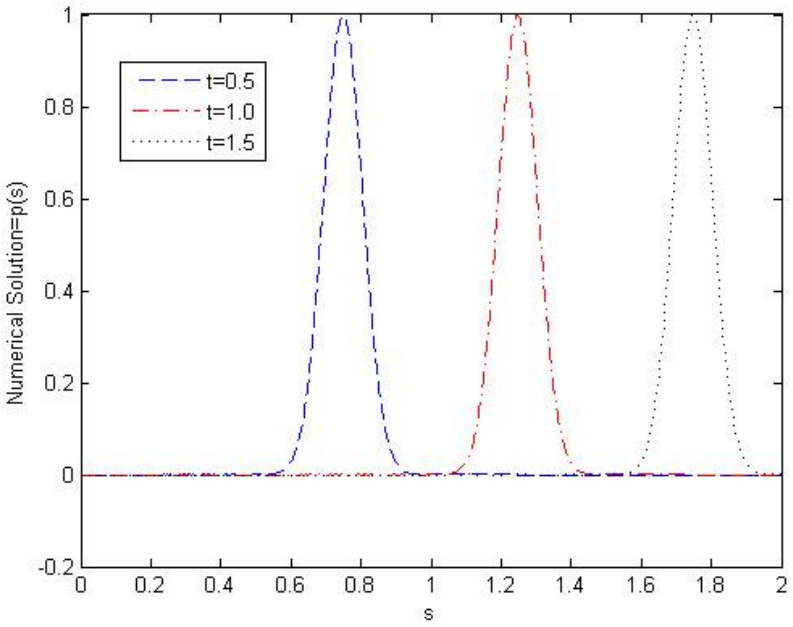

Figure 5.2: Numerical solution $p(s,t)$ of Example 1 at different time steps by Lax-Wendroff method.

increases the impulse size remains same in case of Lax-Wendroff approximation, on the other side (upwind approximation), the size of impulse decreases.

Example 2. Consider Eq. (5.1) with coefficient $B(s) = \sin s$.
Initial and boundary conditions are given by

$$p_0(s) = e^{-10(5s-3)^2}, \quad p(s,0) = 0, \qquad s \in [-\delta, 0] \cup [2, 2+\delta].$$

The numerical simulation determined by upwind finite volume approximation at different time step $t = 0.5, t = 1.0$ and $t = 1.5$ are depicted in Fig. 5.4, where the size of time-step $\Delta t = 0.1$ and mesh-size $\Delta v = 0.2$. From Fig. 5.4, we observe that, as time increases the impulse size decreases.

The approximate solution $p(s,t)$ determined by Lax-Wendroff finite volume approximation at different time levels $t = 0.5, t = 1.0$ and $t = 1.5$ are displayed in Fig. 5.5. The

The Maximum Absolute Error					
$\Delta t \downarrow$	$\Delta s \rightarrow$	1/200	1/400	1/800	1/1600
$\Delta s/2$		0.055536	0.027368	0.013620	0.006794
$\Delta s/4$		0.027272	0.013592	0.006792	0.003395
$\Delta s/8$		0.013581	0.006785	0.003392	0.001696
$\Delta s/16$		0.006784	0.003391	0.001695	0.000848

Table 5.2: Error table of Example 1 determined by Lax-Wendroff scheme.

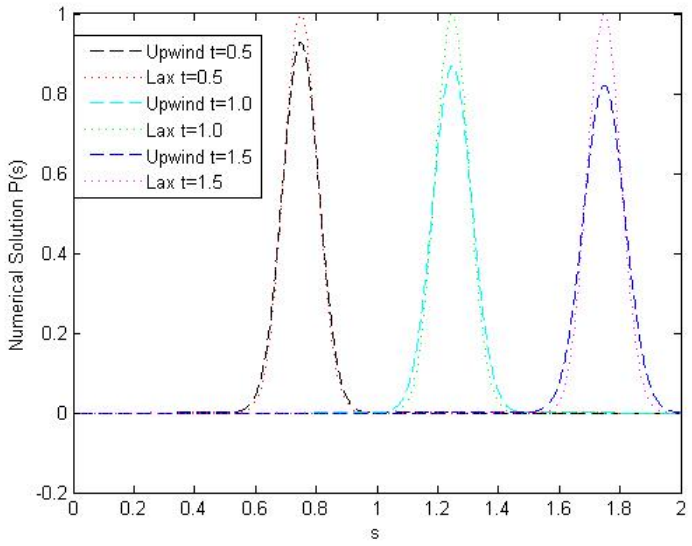

Figure 5.3: Comparison of numerical solution $p(s,t)$ between upwind and Lax-Wendroff approximations at different time levels.

comparison between numerical results obtained by upwind and Lax-Wendroff schemes are shown in Fig. 5.6.

Example 3. Consider Eq. (5.1) with parameter $B(s) = \sin s + \cos s$.
Initial and boundary conditions are given by

$$p_0(s) = e^{-10(12s-3)^2/5}, \quad p(s,0) = 0, \qquad s \in [-\delta, 0] \cup [2, 2+\delta].$$

The numerical solution $p(s,t)$ obtained by upwind finite volume approximation at different time level $t = 0.5, t = 1.0$ and $t = 1.5$ are given in Fig. 5.7. The numerical solution $p(s,t)$ engendered by Lax-Wendroff finite volume approximation at different time level $t = 0.5, t = 1.0$ and $t = 1.5$ are shown in Fig. 5.8.
Figure 5.9 shows that as time increases the impulse size remains same in case of Lax-Wendroff approximation, whereas in upwind approximation, impulse size decreases.

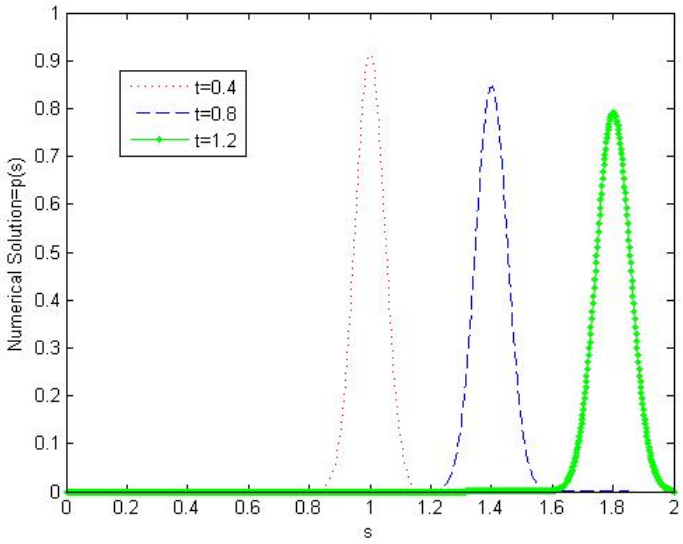

Figure 5.4: Numerical solution $p(s,t)$ of Example 2 at different times obtained by upwind scheme.

The Maximum Absolute Error					
$\Delta t \downarrow$	$\Delta s \rightarrow$	1/200	1/400	1/800	1/1600
$\Delta s/2$		0.090845	0.045423	0.022711	0.011356
$\Delta s/4$		0.054467	0.027234	0.013617	0.006808
$\Delta s/8$		0.026910	0.013455	0.006727	0.003364
$\Delta s/16$		0.013843	0.006921	0.003461	0.001730

Table 5.3: Error table of Example 2 determined by upwind scheme.

5 Summary

This chapter presented a numerical solution of the governing equation by using two different schemes. The governing equation is associated with the age-structured neuron model. Numerical construction mainly relies on the construction of upwind and Lax-wendroff finite volume approximations. The consistency, stability, and convergence for above schemes are discussed. A number of numerical examples are carried out in the support of the proposed theory. Finally, the half meshing error table demonstrate the fact that the methods are convergent in space and time.

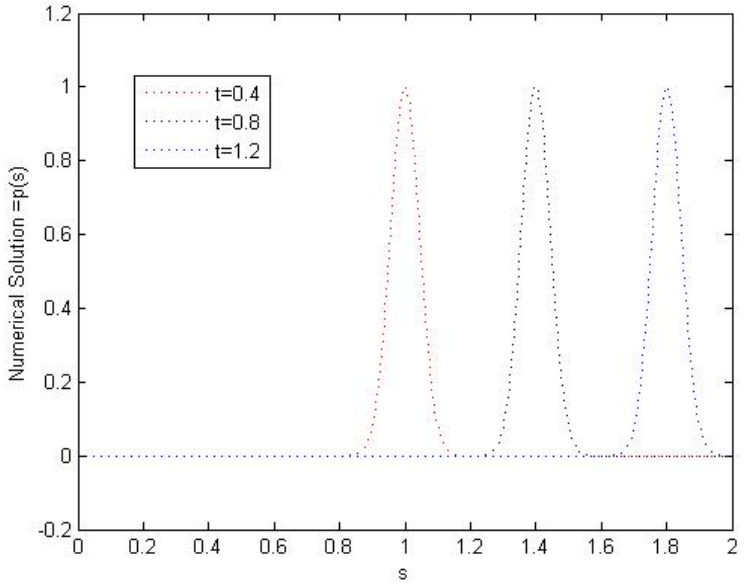

Figure 5.5: Numerical solution $p(s,t)$ of Example 2 at different times determined by Lax-Wendroff Scheme.

The Maximum Absolute Error					
$\Delta t \downarrow$	$\Delta s \rightarrow$	1/200	1/400	1/800	1/1600
$\Delta s/2$		0.097694	0.046788	0.022880	0.011313
$\Delta s/4$		0.053130	0.026899	0.013533	0.006787
$\Delta s/8$		0.026753	0.013416	0.006718	0.003361
$\Delta s/16$		0.013714	0.006889	0.003453	0.001728

Table 5.4: Error table of Example 2 determined by Lax-Wendroff scheme.

The Maximum Absolute Error					
$\Delta t \downarrow$	$\Delta s \rightarrow$	1/200	1/400	1/800	1/1600
$\Delta s/2$		0.107050	0.053525	0.026763	0.013381
$\Delta s/4$		0.046732	0.023366	0.011683	0.005841
$\Delta s/8$		0.027477	0.013738	0.006869	0.003435
$\Delta s/16$		0.014262	0.007131	0.003565	0.001783

Table 5.5: Error table for Example 3 based on the upwind finite volume approximation.

The Maximum Absolute Error					
$\Delta t \downarrow$	$\Delta s \rightarrow$	1/200	1/400	1/800	1/1600
$\Delta s/2$		0.099030	0.051522	0.026263	0.013257
$\Delta s/4$		0.047903	0.023434	0.011700	0.005846
$\Delta s/8$		0.027410	0.013722	0.006865	0.003434
$\Delta s/16$		0.014122	0.007096	0.003557	0.001781

Table 5.6: Error table of Example 3 based on the Lax-Wendroff finite volume approximation.

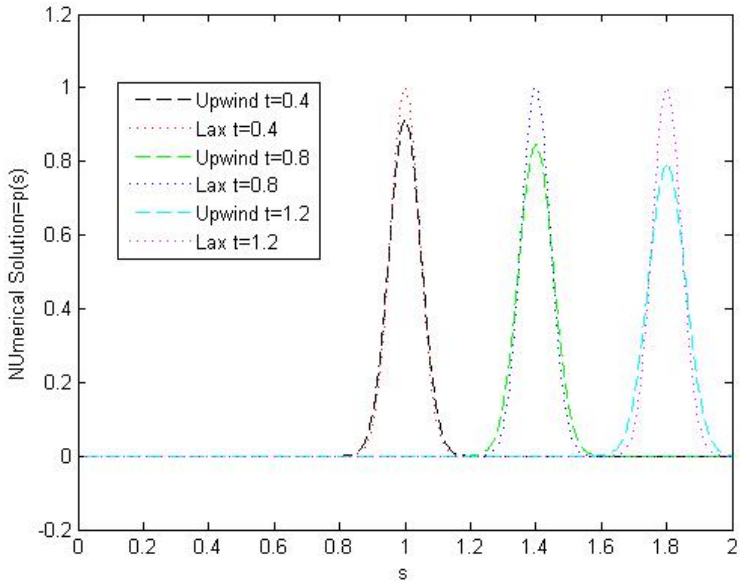

Figure 5.6: Comparison of numerical results $p(s,t)$ obtained by upwind and Lax-Wendroff finite volume approximations of Example 2 at different time levels.

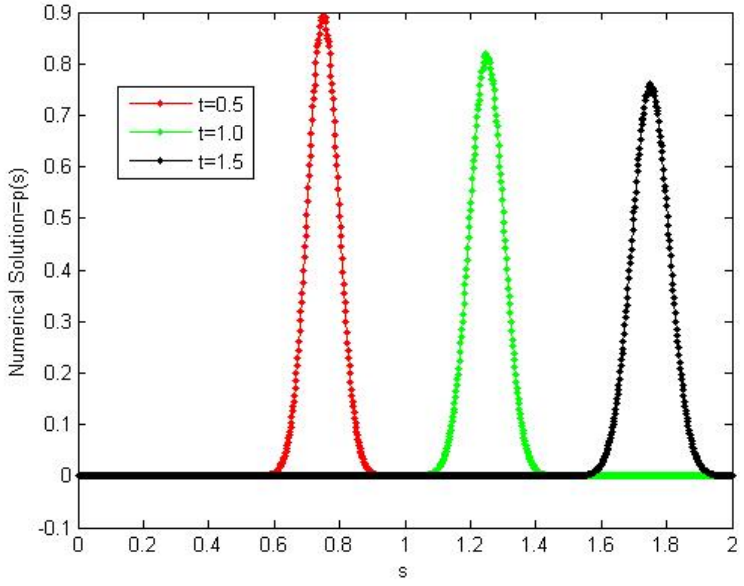

Figure 5.7: Numerical solution $p(s,t)$ of Example 3 at different times by the upwind scheme.

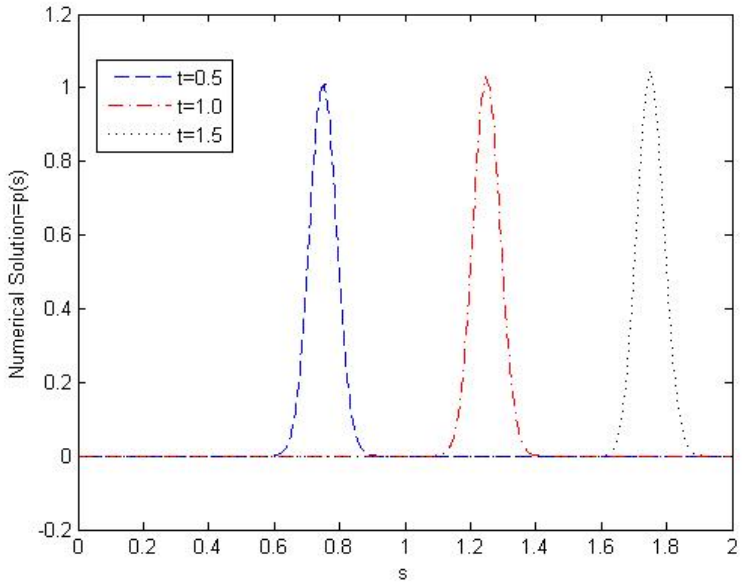

Figure 5.8: Numerical solution $p(s,t)$ of Example 3 at different times determined by Lax-Wendroff.

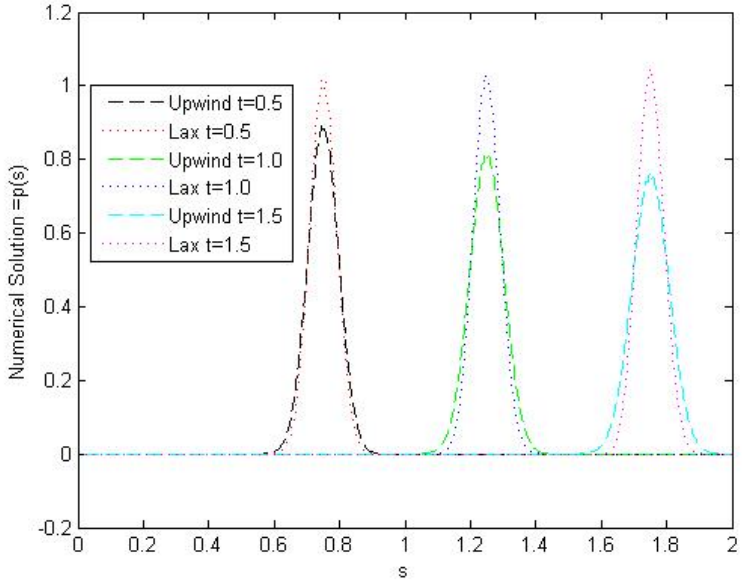

Figure 5.9: Comparison of numerical solution $p(s,t)$ between upwind and Lax-Wendroff approximations of Example 3 at different time steps.

Chapter 6

IMEX-WENO Finite Volume Approximation for Nonlinear Age-Structured Population Model

5

1 Introduction

The mathematical study of age-structured populations play a major role in population dynamics. The population of human, plant, and animal are all age-structured. Age is an intrinsic and main argument of structuring a population. Many of the internal variables depend on the age because the difference in ages means the difference in reproduction, the difference in survival capacities, and different behaviours. Earlier these studies were restricted to the demography, but nowadays its mathematical theory is very useful for modelling of cancer, neuron, ecological system, epidemiology and many other fields, see [84, 95, 98, 117, 120, 177].

Lotka and McKendrick introduced the first linear age-structured population model that supports exponential solution [79, 178] which was later extended for non-linear models by Gurtin and MacCamy [84]. The authors formed the nonlinear form by using the fertility and mortality factors which are dependent on total population size. During the last two decades, a number of authors [91, 96, 98, 177, 179, 180] produced different algorithms to solve such type of population model equations. For the simplification of mathematical analysis, many models presumed that the mortality rate and other parameters are bounded which lead to the possibility of immortality. There are some models which impose a maximum age factor that cannot be reached, and must require that the mortality rate becomes unbounded at that age [90, 181, 182].

It is known that, when the maximum age is infinite, the solution is smooth and its derivatives are bounded if certain compatibility conditions are satisfied [84]. On the other hand, when the maximum age is finite, the solution may be stiff, depending on the mortality function, even if all compatibility conditions are satisfied. In that situation, most of the

[5]Santosh Kumar and Paramjeet Singh *"High-order IMEX-WENO finite volume approximation for nonlinear age-structured population model"*, International Journal of Computer Mathematics, 95 (01),Taylor & Francis, 82-97, (2018).

numerical methods existing in the literature does not work well near the maximum age. A linear model with finite maximum age can produce quantitatively good results of population dynamics for short period of advanced ages. However, a nonlinear model with finite maximum age provides qualitative as well as the quantitative study of population dynamics. Therefore, in the next section, we consider an age-structured population model in which all human beings have a finite maximum age. Further, we assume that the fertility and mortality factors depend on the age, seasonality and external resources in which intrinsic mortality is unbounded. The main objective of the numerical scheme for such type of population models is to form the projections of population growth for the future time. In order to see the long-term simulations in case of stiff type source term, the choice of appropriate higher-order methods would be desirable and, thus (implicit-explicit weighted essentially non-oscillatory) IMEX-WENO finite volume method is a good choice for such type of equations. Moreover, our scheme is suitable to the different types of mortality functions which are used in population modeling. There are other high-order schemes available in literature for solving the governing equation given in [116, 183–185]. These schemes become complicated to implement due to the stiff source terms and non-local functionality. Iannelli and Milner [98] concluded that the standard lower order numerical methods are not suitable for population model equation.

2 Model

We first consider the evolution of a population age density of classical model, given by

$$\begin{aligned}
&\frac{\partial \rho}{\partial t} + \frac{\partial \rho}{\partial a} = -\mu\left(a, \mathsf{P}(t)\right)\rho(a,t),\ a \geq 0,\ t \geq 0,\\
&B(t) = \rho(0,t) = \int_0^\infty \beta(a, \mathsf{P}(t))\rho(a,t), \qquad (6.1)\\
&\rho(a,0) = \rho_0(a),\\
&\mathsf{P}(t) = \int_0^\infty \rho(a,t)da,
\end{aligned}$$

where $\mathsf{P}(t)$ is the total population at time t and $\rho(a,t)$ is the population age density at time t. Here, $\mu(a)$ is age-specific mortality rate (i.e. death rate of a population whose age lies in the interval $[a, a+da]$ in one-time unit), therefore $\mu(a, \mathsf{P(t)})$ represents the total number of death rate at time t. Similarly, $\beta(a)$ is the age-specific fertility rate (i.e. number of new born produced by the single individual whose age lies in $[a, a+da]$).

Therefore $\beta(a, \mathsf{P}(\mathsf{t}))$ represent the total reproduction rate. Finally, $\rho_0(.)$ represents the initial size of the population.

In this chapter, we consider all aspects of mortality rate and write it in the separable form and thus mortality rate is

$$\mathsf{m}(a) + \xi(a, \mathsf{I}_\xi(a,t), t). \tag{6.2}$$

Here, the function $\mathsf{m}(a)$ denotes the unbounded intrinsic mortality and $\xi(a, \mathsf{I}_\xi(a,t), t)$ represents the external mortality that includes seasonality t and external resources, and depend on the non-local functionality

$$\mathsf{I}_\xi(a,t) = \tau \int_0^a \gamma_\xi(x)\rho(x,t)dx + \int_a^{a_{max}} \gamma_\xi(x)\rho(x,t)dx, \tag{6.3}$$

for some given function $\gamma_\xi(.)$ and $0 \leq \tau < 1$.

Similarly, we also consider all factors of fertility rate that depend on the external resources, i.e., $\eta(a, \mathsf{I}_\eta(a,t), t)$. The non-local function $\mathsf{I}_\eta(a,t)$ is defined in the same way as given in Eq. (6.3).

Further, from Eq.(6.1), we see that the maximum age was infinite, but in real situation this is not possible, because the population cannot be immortal. Thus, we consider a finite maximum age.

Finally, we have a complete model equation

$$\begin{cases} \dfrac{\partial \rho}{\partial t} + \dfrac{\partial \rho}{\partial a} = -\left(\mathsf{m}(a) + \xi(a, \mathsf{I}_\xi(a,t), t)\right)\rho(a,t), \ 0 < a < a_{\max}, \ 0 < t < T_{\max}, \\ B(t) = \rho(0,t) = \displaystyle\int_0^{a_{\max}} \eta(a, \mathsf{I}_\eta(a,t), t)\rho(a,t)da, \\ \rho(a,0) = \rho_0(a), 0 \leq a \leq a_{\max} \\ \mathsf{I}_s(a,t) = \tau \displaystyle\int_0^a \gamma_s(x)\rho(x,t)dx + \int_a^{a_{max}} \gamma_s(x)\rho(x,t)dx, \quad s = \xi, \eta. \end{cases} \tag{6.4}$$

The non-local function $\mathsf{I}_s(a,t)$ depends on population age density ρ in a global way which complicates the construction of higher-order WENO approximation. We point out that the external mortality ξ and fertility rate η depend globally on the population age density ρ, therefore, the modeling equation is highly nonlinear. Another difficulty is the presence of the stiff type of mortality rate $m(a)$ in the model equation. Due to this, the model equation may have discontinuous solution. Therefore, we design a numerical scheme in such a way which maintains high order accuracy in smooth regions and have sharp monotone discontinuity transition. Next, we present some hypothesis on the coefficients of model equation

- $\gamma_s \in C^2([0, a_{\max}])$.
- $\mathsf{m} \in C^2\left([0, a_{\max})\right) > 0$ and $\displaystyle\int_0^{a_{\max}} \mathsf{m}(y)dy = \infty$.

- ξ and η are non-negative, twice continuously differentiable functions and bounded by some constant.
- $\rho_0(.) \in C^2([0, a_{\max}])$ is non-negative and satisfy the zero-order compatibility condition $\rho_0(0) = \int_0^{a_{\max}} \eta(a, \mathsf{l}_\eta(0), 0)\rho_0(a)da$.

3 Numerical Approximation

We design a numerical scheme based on the method of lines in which the spatial discretization is done using WENO5 approximation and temporal discretization is done by IMEX Runge-Kutta method.

Consider Eq. (6.4) and write it in standard form as

$$\partial_t \rho(a,t) = -\partial_a \mathsf{f}(\rho(a,t)) + \hat{\mathsf{S}}(\rho, a, t), \tag{6.5}$$

where

- $\mathsf{f}(\rho(a,t)) = \rho(a,t)$ is flux function,
- $\hat{\mathsf{S}}(\rho, a, t) = -\left(\mathsf{m}(a) + \xi(a, \mathsf{l}_\xi(a,t), t)\right)\rho(a,t)$ is source term.

Since the natural mortality is unbounded which creates difficulty for a numerical approximation. Therefore, we consider an intermediate value $a^* \in (0, a_{\max})$ such that natural mortality $m(a)$ is bounded in the interval $[0, a^*]$ and for the later age $a* \le a \le a_{\max}$, we define the mortality by the following function $g(a) = \exp(\int_{a*}^{a} \mathsf{m}(y)dy),\ a* \le a \le a_{\max}$, $g(a_{\max}) = \infty$. We discretize the domain $[0, a_{\max}]$ into $N+1$ grid cells $I_0 = [0, a_{1/2}], I_j = [a_{j-1/2}, a_{j+1/2}], j = 1, \ldots, N-1, I_N = [a_{N-1/2}, a_{\max}]$ in such a way that the point a^* become the center point of the intermediate grid cell, say M-th grid cell, with uniform step size $\Delta a = a_{M+1/2} - a_{M-1/2}$. Note that, $a_j = \frac{1}{2}(a_{j+1/2} + a_{j-1/2})$ is the middle point of the jth cell.

The cell average of the unknown function is given by

$$\bar{\rho}(.,t) = \frac{1}{\Delta a} \int_{a_{j-1/2}}^{a_{j+1/2}} \rho(a,t)da.$$

Integrating Eq.(6.5) over the jth grid cell, one obtains

$$\frac{d}{dt}\bar{\rho}_j(.,t) = -\frac{1}{\Delta a}\left[\hat{\mathsf{f}}_{j+1/2} - \hat{\mathsf{f}}_{j-1/2}\right] + \frac{1}{\Delta a}\hat{\mathsf{S}}_j^*,\ j = 1, 2, \ldots, N, \tag{6.6}$$

where $\hat{\mathsf{f}}_{j\pm1/2} = \mathsf{f}(\rho(a_{j-1/2}, t)$ is the numerical flux, and $\hat{\mathsf{S}}_j^*$ is the approximation of cell average of source term.

In order to carry out upwinding for stability, we replace $\hat{\mathsf{f}}_{j+1/2} = \hat{\mathsf{F}}(\rho^-_{j+1/2}, \rho^+_{j+1/2})$, where

$\hat{\mathsf{F}}(\rho^-, \rho^+)$ is a monotone numerical flux. The modified version of Eq.(6.6) is

$$\frac{d}{dt}\bar{\rho}_j(.,t) \equiv -\frac{1}{\Delta a}\left[\hat{\mathsf{F}}(\rho^-_{j+1/2}, \rho^+_{j+1/2}) - \hat{\mathsf{F}}(\rho^-_{j-1/2}, \rho^+_{j-1/2})\right] + \hat{\mathsf{S}}^*_j.$$

We now choose the numerical flux in such a way so that it must be consistent with the original flux term $\mathsf{f}(\rho(a,t))$. There are many choices for such type of fluxes. Here, we choose the simplest and inexpensive, Lax-Friedrichs formulation. The flux expression we use is:

$$\hat{\mathsf{F}}(\rho^-_{j+1/2}, \rho^+_{j+1/2}) = \frac{1}{2}\left[\mathsf{F}(\rho^-_{j+1/2}) + \mathsf{F}(\rho^+_{j+1/2}) - \zeta\left(\rho^+_{j+1/2} - \rho^-_{j+1/2}\right)\right],$$

$\zeta = \max|\mathsf{f}'(\rho(a,t))|$. Here, the values $\rho^{\pm}_{j+1/2}$ and $\rho^{\pm}_{j-1/2}$ are high order point-wise approximation determined by WENO reconstruction procedure. We here provide a review of WENO reconstruction procedure for the sake of completeness.

Firstly, we calculate the smoothness indicators $\beta_i, i = 0, 1, 2$, corresponding to the ith stencil as given in [147, 150].

$$\beta^+_i = \sum_{k=1}^{r} \int_{a_{j-1/2}}^{a_{j+1/2}} \left(\frac{\partial^k \mathsf{l}_i(a)}{\partial a^k}\right) da\ \Delta a^{2m-1},\ i = 0, 1, 2,$$

where $\mathsf{l}_i(a)$ is 3rd-order interpolating polynomial corresponding to the cells $I_{j+i-2}, I_{j+i-1}, I_{j+i}$. A simple calculation reveals for $2 \le j \le N-2$,

$$\begin{aligned}
\beta^+_0 &= \frac{13}{12}\left(\bar{\rho}_{j-2} - 2\bar{\rho}_{j-1} + \bar{\rho}_j\right)^2 + \frac{1}{4}(\bar{\rho}_{j-2} - 4\bar{\rho}_{j-1} + 3\bar{\rho}_j)^2,\\
\beta^+_1 &= \frac{13}{12}\left(\bar{\rho}_{j-1} - 2\bar{\rho}_j + \bar{\rho}_{j+1}\right)^2 + \frac{1}{4}(\bar{\rho}_{j-1} - \bar{\rho}_{j+1})^2,\\
\beta^+_2 &= \frac{13}{12}\left(\bar{\rho}_j - 2\bar{\rho}_{j+1} + \bar{\rho}_{j+2}\right)^2 + \frac{1}{4}(3\bar{\rho}_j - 4\bar{\rho}_{j+1} + \bar{\rho}_{j+2})^2.
\end{aligned}$$

The corresponding linear weights are

$$\gamma_0 = \frac{1}{10}, \gamma_1 = \frac{6}{10}, \gamma_2 = \frac{3}{10}.$$

We now define the non-linear ENO stencil weights

$$\alpha^+_r = \frac{\gamma_r}{(\epsilon + \beta^+_r)^2},\ r = 0, 1, 2,$$

where ϵ is a small positive number to avoid the denominator to become zero. For numerical simulation we take $\epsilon = 10^{-6}$. To obtain the WENO stencil weights, we take a convex combination of ENO stencil weights

$$\omega^+_r = \frac{\alpha^+_r}{\sum_{m=0}^{2} \alpha^+_m}, \quad \sum_{r=0}^{2} \omega^+_r = 1.$$

Therefore, the corresponding numerical flux for WENO5 is defined as

$$\rho^{-}_{j+1/2} = \omega_0^+ \left(\frac{1}{3}\bar{\rho}_{j-2} - \frac{7}{6}\bar{\rho}_{j-1} + \frac{11}{6}\bar{\rho}_j\right) + \omega_1^+ \left(-\frac{1}{6}\bar{\rho}_{j-1} + \frac{5}{6}\bar{\rho}_j + \frac{1}{3}\bar{\rho}_{j+1}\right) + \omega_2^+ \left(\frac{1}{3}\bar{\rho}_j + \frac{5}{6}\bar{\rho}_{j+1} - \frac{1}{6}\bar{\rho}_{j+2}\right), \quad 2 \le j \le N-2.$$

We can compute the value of $\rho^{+}_{j-1/2}$ in symmetric way. For $j = 0, 1$, we can use smoothness indicators and WENO stencil weights for the fluxes. Our computational experience shows that the use of linear weights for these two cells give better results which are shown in numerical experiments. Thus

$$\hat{\mathsf{f}}^{+}_{1/2} = \gamma_0 \left(\frac{1}{3}\bar{\rho}_0 + \frac{5}{6}\bar{\rho}_1 - \frac{1}{6}\bar{\rho}_2\right) + \gamma_1 \left(\frac{11}{6}\bar{\rho}_1 - \frac{7}{6}\bar{\rho}_2 + \frac{1}{3}\bar{\rho}_3\right) + \gamma_2 \left(\frac{13}{3}\bar{\rho}_2 - \frac{31}{6}\bar{\rho}_3 + \frac{11}{6}\bar{\rho}_4\right)$$
$$\hat{\mathsf{f}}^{+}_{3/2} = \gamma_0 \left(\frac{-1}{6}\bar{\rho}_0 + \frac{5}{6}\bar{\rho}_1 + \frac{1}{3}\bar{\rho}_2\right) + \gamma_1 \left(\frac{1}{3}\bar{\rho}_1 + \frac{5}{6}\bar{\rho}_2 - \frac{1}{6}\bar{\rho}_3\right) + \gamma_2 \left(\frac{11}{6}\bar{\rho}_2 - \frac{7}{6}\bar{\rho}_3 + \frac{1}{3}\bar{\rho}_4\right).$$

For the two cells of right boundary, we need the smoothness indicator and WENO stencil weights. Thus for $j = N-1$, smoothness indicator functions are given by

$$\beta_0^+ = \frac{10}{3}\bar{\rho}^2_{N-4} + \frac{61}{3}\bar{\rho}^2_{N-3} + \frac{22}{3}\bar{\rho}^2_{N-2} - \frac{49}{3}\bar{\rho}_{N-4}\bar{\rho}_{N-3} + \frac{29}{3}\bar{\rho}_{N-4}\bar{\rho}_{N-2} - \frac{73}{3}\bar{\rho}_{N-3}\bar{\rho}_{N-2},$$
$$\beta_1^+ = \frac{4}{3}\bar{\rho}^2_{N-3} + \frac{25}{3}\bar{\rho}^2_{N-2} + \frac{10}{3}\bar{\rho}^2_{N-1} - \frac{19}{3}\bar{\rho}_{N-3}\bar{\rho}_{N-2} + \frac{11}{3}\bar{\rho}_{N-3}\bar{\rho}_{N-1} - \frac{31}{3}\bar{\rho}_{N-2}\bar{\rho}_{N-1},$$
$$\beta_2^+ = \frac{4}{3}\bar{\rho}^2_{N-2} + \frac{13}{3}\bar{\rho}^2_{N-1} + \frac{4}{3}\bar{\rho}^2_{N} - \frac{13}{3}\bar{\rho}_{N-2}\bar{\rho}_{N-1} + \frac{5}{3}\bar{\rho}_{N-2}\bar{\rho}_{N} - \frac{13}{3}\bar{\rho}_{N-1}\bar{\rho}_{N}.$$

The corresponding linear weights are

$$\gamma_0 = \frac{-3}{110}, \gamma_1 = \frac{47}{110}, \gamma_2 = \frac{3}{15}.$$

The smoothness indicator functions for $j = N$,

$$\beta_0^+ = \frac{22}{3}\bar{\rho}^2_{N-4} + \frac{121}{3}\bar{\rho}^2_{N-3} + \frac{40}{3}\bar{\rho}^2_{N-2} - \frac{103}{3}\bar{\rho}_{N-4}\bar{\rho}_{N-3} + \frac{59}{3}\bar{\rho}_{N-4}\bar{\rho}_{N-2} - \frac{139}{3}\bar{\rho}_{N-3}\bar{\rho}_{N-2},$$
$$\beta_1^+ = \frac{10}{3}\bar{\rho}^2_{N-3} + \frac{61}{3}\bar{\rho}^2_{N-2} + \frac{22}{3}\bar{\rho}^2_{N-1} - \frac{49}{3}\bar{\rho}_{N-3}\bar{\rho}_{N-2} + \frac{29}{3}\bar{\rho}_{N-3}\bar{\rho}_{N-1} - \frac{73}{3}\bar{\rho}_{N-2}\bar{\rho}_{N-1},$$
$$\beta_2^+ = \frac{4}{3}\bar{\rho}^2_{N-2} + \frac{25}{3}\bar{\rho}^2_{N-1} + \frac{10}{3}\bar{\rho}^2_{N} - \frac{19}{3}\bar{\rho}_{N-2}\bar{\rho}_{N-1} + \frac{11}{3}\bar{\rho}_{N-2}\bar{\rho}_{N} - \frac{31}{3}\bar{\rho}_{N-1}\bar{\rho}_{N}.$$

The corresponding linear weights are

$$\gamma_0 = \frac{3}{65}, \gamma_1 = \frac{-417}{1430}, \gamma_2 = \frac{137}{110}.$$

We notice that the linear weights corresponding to $(N-1)$th and Nth cells are negative. We avoid these negative linear weights by splitting into two linear weights. To do so, we

follow a procedure as defined in [186]. For $(N-1)$th cell

$$\tilde{\gamma}_i^+ = \frac{1}{2}(\gamma_i + \theta|\gamma_i|), \text{ where } \theta = 3, \ \tilde{\gamma}_i^- = \tilde{\gamma}_i^+ - \gamma_i, \quad i = 0, 1, 2.$$
$$\tilde{\gamma}_0^+ = \frac{3}{110}, \ \tilde{\gamma}_1^+ = \frac{94}{110}, \ \tilde{\gamma}_2^+ = \frac{6}{5},$$
$$\tilde{\gamma}_0^- = \frac{6}{110}, \ \tilde{\gamma}_1^- = \frac{47}{110}, \ \tilde{\gamma}_2^- = \frac{3}{5}.$$

We now scale these factors as

$$\gamma_i^\pm = \frac{\tilde{\gamma}_i^\pm}{z_1^\pm}, \text{ where } z_1^+ = \sum \tilde{\gamma}_i^+ = \frac{229}{110}, \quad z_1^- = \sum \tilde{\gamma}_i^- = \frac{119}{110},$$
$$\implies \gamma_0^+ = \frac{3}{229}, \ \gamma_1^+ = \frac{94}{229}, \ \gamma_3^+ = \frac{132}{229},$$
$$\text{and } \gamma_0^- = \frac{6}{119}, \ \gamma_1^- = \frac{47}{119}, \ \gamma_2^- = \frac{66}{119}.$$

The corresponding non-linear weights are

$$\tilde{\omega}_r^\pm = \frac{\tilde{\alpha}_r^\pm}{\sum_{m=0}^{2} \tilde{\alpha}_r^\pm}, \quad \tilde{\alpha}_r^\pm = \frac{\gamma_r^\pm}{(\epsilon + \beta_r^+)^2}, \ r = 0, 1, 2. \tag{6.7}$$

Now, we have two polynomials corresponding to $J = N-1$

$$\begin{aligned}
\tilde{\mathsf{f}}_{N-1/2}^+ =& \tilde{\omega}_0^+ \left(\frac{11}{6}\bar{\rho}_{N-4} - \frac{31}{6}\bar{\rho}_{N-3} + \frac{13}{3}\bar{\rho}_{N-2} \right) + \tilde{\omega}_1^+ \left(\frac{1}{3}\bar{\rho}_{N-3} - \frac{7}{6}\bar{\rho}_{N-2} + \frac{11}{6}\bar{\rho}_{N-1} \right) \\
&+ \tilde{\omega}_2^+ \left(-\frac{1}{6}\bar{\rho}_{N-2} + \frac{5}{6}\bar{\rho}_{N-1} + \frac{1}{3}\bar{\rho}_N \right). \\
\tilde{\mathsf{f}}_{N-1/2}^- =& \tilde{\omega}_0^- \left(\frac{11}{6}\bar{\rho}_{N-4} - \frac{31}{6}\bar{\rho}_{N-3} + \frac{13}{3}\bar{\rho}_{N-2} \right) + \tilde{\omega}_1^- \left(\frac{1}{3}\bar{\rho}_{N-3} - \frac{7}{6}\bar{\rho}_{N-2} + \frac{11}{6}\bar{\rho}_{N-1} \right) \\
&+ \tilde{\omega}_2^- \left(-\frac{1}{6}\bar{\rho}_{N-2} + \frac{5}{6}\bar{\rho}_{N-1} + \frac{1}{3}\bar{\rho}_N \right).
\end{aligned}$$

Therefore, the corresponding numerical flux is defined as

$$\hat{\mathsf{f}}_{N-1/2}^+ = z_1^+ \tilde{\mathsf{f}}_{N-1/2}^+ - z_1^- \tilde{\mathsf{f}}_{N-1/2}^-.$$

Similarly, we can find the new linear weights corresponding to the last cell for $j = N$,

$$\tilde{\gamma}_0^+ = \frac{132}{4111}, \ \tilde{\gamma}_1^+ = \frac{417}{4111}, \ \tilde{\gamma}_2^+ = \frac{3562}{4111}, \ z_1^+ = \frac{4111}{1430},$$
$$\tilde{\gamma}_0^- = \frac{66}{2681}, \ \tilde{\gamma}_1^- = \frac{834}{2681}, \ \tilde{\gamma}_2^- = \frac{1781}{2681}, \ z_1^- = \frac{2681}{1430}.$$

$$\begin{aligned}
\tilde{\mathsf{f}}^{+}_{N+1/2} =&\tilde{\omega}^{+}_{0}\left(\frac{13}{3}\bar{\rho}_{N-4}-\frac{67}{6}\bar{\rho}_{N-3}+\frac{47}{6}\bar{\rho}_{N-2}\right)+\tilde{\omega}^{+}_{1}\left(\frac{11}{6}\bar{\rho}_{N-3}-\frac{31}{6}\bar{\rho}_{N-2}+\frac{13}{3}\bar{\rho}_{N-1}\right)\\
&+\tilde{\omega}^{+}_{2}\left(\frac{1}{3}\bar{\rho}_{N-2}-\frac{7}{6}\bar{\rho}_{N-1}+\frac{11}{6}\bar{\rho}_{N}\right),\\
\tilde{\mathsf{f}}^{-}_{N+1/2} =&\tilde{\omega}^{-}_{0}\left(\frac{13}{3}\bar{\rho}_{N-4}-\frac{67}{6}\bar{\rho}_{N-3}+\frac{47}{6}\bar{\rho}_{N-2}\right)+\tilde{\omega}^{-}_{1}\left(\frac{11}{6}\bar{\rho}_{N-3}-\frac{31}{6}\bar{\rho}_{N-2}+\frac{13}{3}\bar{\rho}_{N-1}\right)\\
&+\tilde{\omega}^{-}_{2}\left(\frac{1}{3}\bar{\rho}_{N-2}-\frac{7}{6}\bar{\rho}_{N-1}+\frac{11}{6}\bar{\rho}_{N}\right),
\end{aligned}$$

where $\tilde{\omega}^{\pm}_{r}$ are WENO stencil weights and defined in the same way as given in Eq.(6.7). Thus

$$\hat{\mathsf{f}}^{+}_{N+1/2}=z^{+}_{1}\tilde{\mathsf{f}}^{+}_{N+1/2}-z^{-}_{1}\tilde{\mathsf{f}}^{-}_{N+1/2}.$$

We now evaluate the left boundary condition by a fifth-order approximation

$$\bar{\rho}_0=\Delta a\hat{\sum}_{i=j}^{N}\eta_j\bar{\rho}_j,\quad \eta_j=\eta(a_j,\mathsf{I}_{\eta_j},.),\ \mathsf{I}_{\eta_j}=\mathsf{I}_{\eta}(a_j,.) \tag{6.8}$$

Here, the summation $\hat{\sum}$ is defined as

$$\begin{aligned}
\hat{\sum}_{i=k}^{l}V_j=&\frac{251}{720}V_k+\frac{299}{240}V_{k+1}+\frac{211}{240}V_{k+2}+\frac{739}{720}V_{k+3}+\frac{739}{720}V_{l-3}\\
&+\frac{211}{240}V_{l-2}+\frac{299}{240}V_{l-1}+\frac{251}{720}V_l+\sum_{i=k+4}^{l-4}V_i,\quad \text{for } l-k\geq 7.
\end{aligned}\tag{6.9}$$

Further, we calculate the non-local function I_{s_j} in the following way

$$\mathsf{I}_{s_j}=I_1+\tau\Delta a\hat{\sum}_{i=1}^{j}\gamma_{s_i}\bar{\rho}_i+\Delta a\hat{\sum}_{i=j}^{N}\gamma_{s_i}\bar{\rho}_i,\quad s=\eta,\xi,\quad 8\leq j\leq N-7,$$

where $I_1=\Delta a\left(\frac{55}{24}\gamma_{s_1}\bar{\rho}_1-\frac{59}{24}\gamma_{s_2}\bar{\rho}_2+\frac{37}{24}\gamma_{s_3}\bar{\rho}_3-\frac{9}{24}\gamma_{s_4}\bar{\rho}_4\right)$ is the integral approximation over first interval which avoids the use of ρ_0. The remaining values of non-local functions are given by

$$\begin{aligned}
&\mathsf{I}_{s_0}=I_1+\Delta a\hat{\sum}_{i=1}^{N}\gamma_{s_i}\bar{\rho}_i,\quad \mathsf{I}_{s_1}=\tau I_1+\Delta a\hat{\sum}_{i=1}^{N}\gamma_{s_i}\bar{\rho}_i,\quad \mathsf{I}_{s_N}=\tau\mathsf{I}_{s_0},\\
&\mathsf{I}_{s_2}=\tau\Delta a\left(\frac{8}{3}\gamma s_1\bar{\rho}_1-\frac{5}{3}\gamma s_2\bar{\rho}_2+\frac{4}{3}\gamma s_3\bar{\rho}_3-\frac{1}{3}\gamma s_4\bar{\rho}_4\right)+\Delta a\hat{\sum}_{i=2}^{N}\gamma_{s_i}\bar{\rho}_i,\\
&\mathsf{I}_{s_3}=\tau\Delta a\left(\frac{21}{8}\gamma s_1\bar{\rho}_1-\frac{9}{8}\gamma s_2\bar{\rho}_2+\frac{15}{8}\gamma s_3\bar{\rho}_3-\frac{3}{8}\gamma s_4\bar{\rho}_4\right)+\Delta a\hat{\sum}_{i=3}^{N}\gamma_{s_i}\bar{\rho}_i,\\
&\mathsf{I}_{s_4}=\tau\Delta a\left(\frac{21}{8}\gamma s_1\bar{\rho}_1-\frac{7}{6}\gamma s_2\bar{\rho}_2+\frac{29}{12}\gamma s_3\bar{\rho}_3+\frac{1}{6}\gamma s_4\bar{\rho}_4-\frac{1}{24}\gamma s_5\bar{\rho}_5\right)+\Delta a\hat{\sum}_{i=4}^{N}\gamma_{s_i}\bar{\rho}_i
\end{aligned}$$

$$
\begin{aligned}
\mathsf{I}_{s_5} &= \tau\Delta a\Big(\frac{21}{8}\gamma s_1\bar{\rho}_1 - \frac{7}{6}\gamma s_2\bar{\rho}_2 + \frac{19}{8}\gamma s_3\bar{\rho}_3 + \frac{17}{24}\gamma s_4\bar{\rho}_4 + \frac{1}{2}\gamma_{s_5}\bar{\rho}_5 - \frac{1}{24}\gamma_{s_6}\bar{\rho}_6\Big)\\
&\quad +\Delta a\hat{\sum}_{i=5}^{N}\gamma_{s_i}\bar{\rho}_i,\\
\mathsf{I}_{s_6} &= \tau\Delta a\Big(\frac{21}{8}\gamma s_1\bar{\rho}_1 - \frac{7}{6}\gamma s_2\bar{\rho}_2 + \frac{19}{8}\gamma s_3\bar{\rho}_3 + \frac{2}{3}\gamma s_4\bar{\rho}_4 + \frac{25}{24}\gamma_{s_5}\bar{\rho}_5 + \frac{1}{2}\gamma_{s_6}\bar{\rho}_6\\
&\quad -\frac{1}{24}\gamma_{s_7}\bar{\rho}_7\Big) + \Delta a\hat{\sum}_{i=6}^{N}\gamma_{s_i}\bar{\rho}_i,\\
\mathsf{I}_{s_7} &= \tau\Delta a\Big(\frac{21}{8}\gamma s_1\bar{\rho}_1 - \frac{7}{6}\gamma s_2\bar{\rho}_2 + \frac{19}{8}\gamma s_3\bar{\rho}_3 + \frac{2}{3}\gamma s_4\bar{\rho}_4 + \gamma_{s_5}\bar{\rho}_5 + \frac{25}{24}\gamma_{s_6}\bar{\rho}_6\\
&\quad +\frac{1}{2}\gamma_{s_7}\bar{\rho}_7 - \frac{1}{24}\gamma_{s_8}\bar{\rho}_8\Big) + \Delta a\hat{\sum}_{i=7}^{N}\gamma_{s_i}\bar{\rho}_i,\\
\mathsf{I}_{s_{N-1}} &= \Delta a\Big(\frac{9}{24}\gamma_{s_N}\bar{\rho}_N + \frac{19}{24}\gamma_{s_{N-1}}\bar{\rho}_{N-1} - \frac{5}{24}\gamma_{s_{N-2}}\bar{\rho}_{N-2} + \frac{1}{24}\gamma_{s_{N-3}}\bar{\rho}_{N-3}\Big)\\
&\quad +\tau\left(I_1 + \Delta a\hat{\sum}_{i=1}^{N-1}\gamma_{s_i}\bar{\rho}_i\right),\\
\mathsf{I}_{s_{N-2}} &= \Delta a\Big(\frac{1}{3}\gamma_{s_N}\bar{\rho}_N + \frac{4}{3}\gamma_{s_{N-1}}\bar{\rho}_{N-1} + \frac{1}{3}\gamma_{s_{N-2}}\bar{\rho}_{N-2}\Big) + \tau\left(I_1 + \Delta a\hat{\sum}_{i=1}^{N-2}\gamma_{s_i}\bar{\rho}_i\right),\\
\mathsf{I}_{s_{N-3}} &= \Delta a\Big(\frac{1}{3}\gamma_{s_N}\bar{\rho}_N + \frac{31}{24}\gamma_{s_{N-1}}\bar{\rho}_{N-1} + \frac{7}{8}\gamma_{s_{N-2}}\bar{\rho}_{N-2} + \frac{13}{24}\gamma_{s_{N-3}}\bar{\rho}_{N-3}\\
&\quad -\frac{1}{24}\gamma_{s_{N-4}}\rho_{N-4}\Big) + \tau\left(I_1 + \Delta a\hat{\sum}_{i=1}^{N-3}\gamma_{s_i}\bar{\rho}_i\right),\\
\mathsf{I}_{s_{N-4}} &= \Delta a\Big(\frac{1}{3}\gamma_{s_N}\bar{\rho}_N + \frac{31}{24}\gamma_{s_{N-1}}\bar{\rho}_{N-1} + \frac{5}{6}\gamma_{s_{N-2}}\bar{\rho}_{N-2} + \frac{13}{12}\gamma_{s_{N-3}}\bar{\rho}_{N-3}\\
&\quad +\frac{1}{2}\gamma_{s_{N-4}}\rho_{N-4} - \frac{1}{24}\gamma_{s_{N-5}}\bar{\rho}_{N-5}\Big) + \tau\left(I_1 + \Delta a\hat{\sum}_{i=1}^{N-4}\gamma_{s_i}\bar{\rho}_i\right),\\
\mathsf{I}_{s_{N-5}} &= \Delta a\Big(\frac{1}{3}\gamma_{s_N}\bar{\rho}_N + \frac{31}{24}\gamma_{s_{N-1}}\bar{\rho}_{N-1} + \frac{5}{6}\gamma_{s_{N-2}}\bar{\rho}_{N-2} + \frac{25}{24}\gamma_{s_{N-3}}\bar{\rho}_{N-3}\\
&\quad +\frac{25}{24}\gamma_{s_{N-4}}\rho_{N-4} + \frac{1}{2}\gamma_{s_{N-5}}\bar{\rho}_{N-5} - \frac{1}{24}\gamma_{s_{N-6}}\bar{\rho}_{N-6}\Big) + \tau\left(I_1 + \Delta a\hat{\sum}_{i=1}^{N-5}\gamma_{s_i}\bar{\rho}_i\right),\\
\mathsf{I}_{s_{N-6}} &= \Delta a\Big(\frac{1}{3}\gamma_{s_N}\bar{\rho}_N + \frac{31}{24}\gamma_{s_{N-1}}\bar{\rho}_{N-1} + \frac{5}{6}\gamma_{s_{N-2}}\bar{\rho}_{N-2} + \frac{25}{24}\gamma_{s_{N-3}}\bar{\rho}_{N-3} + \gamma_{s_{N-4}}\rho_{N-4},\\
&\quad +\frac{25}{24}\gamma_{s_{N-5}}\bar{\rho}_{N-5} + \frac{1}{2}\gamma_{s_{N-6}}\bar{\rho}_{N-6} - \frac{1}{24}\gamma_{s_{N-7}}\bar{\rho}_{N-7}\Big) + \tau\left(I_1 + \Delta a\hat{\sum}_{i=1}^{N-6}\gamma_{s_i}\bar{\rho}_i\right).
\end{aligned}
$$

Next step is to find the approximation of the source term which is given by

$$
\hat{\mathsf{S}}_j^* = \begin{cases} -\left(\mathsf{m}(a_j) + \xi\left(a_j, \mathsf{I}_{\xi_j}, .\right)\right)\bar{\rho}_j, & 0 \le j \le M\\ -\left(\mathsf{g}(a_j) + \xi\left(a_j, \mathsf{I}_{\xi_j}, .\right)\right)\bar{\rho}_j, & M+1 \le j \le N, \end{cases}
$$

where $g(a)$ is a known function. Hence, the final form is

$$
\frac{d\bar{\rho}_j(t)}{dt} = -\frac{1}{\Delta a}\left[\left(\hat{\mathsf{f}}_{j+1/2}^{+} - \hat{\mathsf{f}}_{j-1/2}^{+}\right)\right] + \frac{1}{\Delta a}\hat{\mathsf{S}}_j^*,\ j = 1, 2, \ldots, N. \tag{6.10}
$$

3.1 Temporal Discretization

Consider the semi-discrete scheme for the model equation at n-th time level

$$\frac{d\bar{\rho}_j^n}{dt} = \mathsf{L}(\bar{\rho}_j^n) + \mathsf{S}^*(\bar{\rho}_j^n), \tag{6.11}$$

where $\mathsf{L}(\bar{\rho}_j) = -\frac{1}{\Delta a}\left[\bar{\rho}_{j+1/2} - \bar{\rho}_{j-1/2}\right]$ and

$$\hat{\mathsf{S}}_j^* = \begin{cases} -\left(\mathsf{m}(a_j) + \xi\left(a_j, \mathsf{I}_{\xi_j}, .\right)\right)\bar{\rho}_j, & 0 \le j \le M \\ -\left(\mathsf{g}(a_j) + \xi\left(a_j, \mathsf{I}_{\xi_j}, .\right)\right)\bar{\rho}_j, & M+1 \le j \le N, \end{cases}$$

are the spatial discretization of the flux and the source terms, respectively. Here the spatial discretization is determined by WENO5 reconstruction procedure.
Further, we shall use IMEX-RK(implicit-explicit Runge-Kutta) scheme for the temporal discretization. An IMEX-RK scheme is designed by Perschi and Russo for the balance laws with stiff source term, see in [187]. An IMEX Runge-Kutta scheme consists implicit discretization for the source term and explicit discretization for the non-stiff term. When it is applied to the above Eq.(6.11) it takes the following form

$$\begin{aligned} \bar{\rho}_j^{(l)} &= \bar{\rho}_j^n + \Delta t \sum_{i=1}^{l-1} \tilde{a}_{li} \mathsf{L}(\bar{\rho}_j^{(i)}) + \Delta t \sum_{i=1}^{N} a_{li} \mathsf{S}^*(\bar{\rho}_j^i), \\ \bar{\rho}_j^{n+1} &= \bar{\rho}_j^n + \Delta t \sum_{l=1}^{N} \tilde{\omega}_l \mathsf{L}(\bar{\rho}_j^{(l)}) + \Delta t \sum_{l=1}^{N} \omega_l \mathsf{S}^*(\bar{\rho}_j^l). \end{aligned} \tag{6.12}$$

The above scheme can be written with double tableau in Butchar form

$$\begin{array}{c|c} \tilde{c} & \tilde{A} \\ \hline & \tilde{\omega}^T \end{array} \qquad \begin{array}{c|c} c & \mathrm{A} \\ \hline & \omega^T \end{array}$$

where $\tilde{\omega} = (\tilde{\omega}_1, \tilde{\omega}_2, \ldots, \tilde{\omega}_N)^T$, $\tilde{c} = (\tilde{c}_1, \tilde{c}_2, \ldots, \tilde{c}_N)^T$, $c = (c_1, c_2, \ldots, c_N)^T, \omega = (\omega_1, \omega_2, \ldots, \omega_N)^T$ all are coefficient vectors and $\tilde{A} = (\tilde{a}_{li})$, $\tilde{a}_{li} = 0$ for $i \ge l$ and $A = (a_{li})$ are $N \times N$ matrices. These matrices are designed in the manner so that the above scheme become explicitly in L and implicitly in S^*. We further consider diagonally implicit Runge-Kutta (DIRK) method for the source term i.e. $a_{li} = 0$ for $i > l$ and assume that the first column and first row of the matrix A are zero. This is the sufficient condition which ensure that L is always evaluated in explicit manner. By using the above procedure, we present the algorithm that updates the numerical solution in following manner.

- Explicit flux function $\bar{\rho}_{j*}^{(l)} = \bar{\rho}_j^n + \Delta t \sum_{i=1}^{l-2} \tilde{a}_{li} \mathsf{L}(\bar{\rho}_{\mathrm{j}}^{(\mathrm{i})}) + \Delta t \tilde{a}_{l,l-1} \mathsf{L}(\bar{\rho}_j^{(l-1)})$.

- Implicit source function $\bar{\rho}_j^{(l)} = \bar{\rho}_{j*}^{(l)} + \Delta t \sum_{i=1}^{l-1} a_{li} \mathsf{S}^*(\bar{\rho}_j^{(i)}) + \Delta t a_{ll} \mathsf{S}^*(\bar{\rho}_j^{(l)})$.

- Final solution at next time level $\bar{\rho}_j^{n+1} = \bar{\rho}_j^n + \Delta t \sum_{l=1}^{N} \tilde{\omega}_l \mathsf{L}(\bar{\rho}_j^{(l)}) + \Delta t \sum_{l=1}^{N} \omega_l \mathsf{S}^*(\bar{\rho}_j^l)$.

In this work, we use 3rd order explicit SSP method and 3rd order DIRK method that matches the order condition with L-stabilities as given in [187]. In Butcher form it can be written as following,

SSP IMEX-RK

0	0	0	0
1	1	0	0
1/2	1/4	1/4	0
	1/6	1/6	2/3

γ	γ	0	0
1-γ	$1-2\gamma$	γ	0
1/2	$1/2-\gamma$	0	γ
	1/6	1/6	2/3

Hence we have,

$$
\begin{aligned}
\bar{\rho}_j^{(1)} &= \bar{\rho}_j^n + \gamma \Delta t \mathsf{S}^*(\bar{\rho}_j^{(1)}), \\
\bar{\rho}_j^{(2)} &= \bar{\rho}_j^n + \Delta t \mathsf{L}(\bar{\rho}_j^n) + (1-2\gamma)\Delta t \mathsf{S}^*(\bar{\rho}_j^{(1)}) + \gamma \Delta t S^*(\bar{\rho}_j^{(2)}), \\
\bar{\rho}_j^{(3)} &= \bar{\rho}_j^n + \frac{1}{4}\Delta t \left[\mathsf{L}(\bar{\rho}_j^n) + \mathsf{L}(\bar{\rho}_j^{(1)})\right] + (1/2-\gamma)\Delta t \mathsf{S}^*(\bar{\rho}_j^{(1)}) + \gamma \Delta t \mathsf{S}^*(\bar{\rho}_j^{(3)}), \\
\bar{\rho}_j^{n+1} &= \bar{\rho}_j^n + \frac{1}{6}\Delta t \left[\mathsf{L}(\bar{\rho}_j^n) + \mathsf{L}(\bar{\rho}_j^{(1)}) + 4\mathsf{L}(\bar{\rho}_j^{(2)})\right] + \frac{1}{6}\Delta t \left[\mathsf{S}^*(\bar{\rho}_j^{(1)}) + \mathsf{S}^*(\bar{\rho}_j^{(2)}) + 4\mathsf{S}^*(\bar{\rho}_j^{(3)})\right], \\
& \qquad \gamma = (1-\sqrt{2})/2.
\end{aligned}
$$

4 Numerical Experiments

The performance of designed scheme is tested through applying on some test problems. In all experiments, the ratio of convergence is calculated by the following formula

$$r = \frac{\log\left(\frac{e_h}{e_{h/2}}\right)}{\log 2}.$$

where e_h is the error approximation with step size h in the L^1 and L^∞ norm.

$$\|e_h\|_\infty = \max_{0 \le j \le N} |\rho_j^n - \rho(a_j, t^n)| \text{ and } \|e_h\|_1 = h \sum_{j=0}^{N} |\rho_j^n - \rho(a_j, t^n)|.$$

In all the experiments $a_{\max} = 1$, $a^* = 0.9$ and time interval $[0, 0.5]$.

Example 1. Consider the model Eqs.(6.4) with parameters and functions as defined in [96]

$\mathsf{m}(a) = \dfrac{1}{a_{\max} - a},\ \xi(a, y, t) = y,\ \eta(a, y, t) = 4,$

and the weight function $\gamma_s = 1, s = \xi, \eta,$

with initial condition $\rho(a, 0) = 4(1 - a)e^{-\mu a}, \tau = 0.5, \mu = 2.55.$

The exact solution of the given problem is $\rho(a, t) = 4(1 - a)e^{-\mu a}\dfrac{\mu}{((\mu - 1)e^{-\mu t} + 1)}.$

Example 2. Consider stiff type of mortality rate and take different arguments

$\mathsf{m}(a) = \dfrac{1}{2(a_{\max} - a)},\ \xi(a, y, t) = y^2,\ \eta(a, y, t) = 4,\ \gamma_s = 1, s = \xi,$

with initial condition $\rho(a, 0) = 4\sqrt{(1 - a)}e^{-\mu a}, \tau = 0.5, \mu = 2.55.$

The corresponding exact solution is

$\rho(a, t) = 4\sqrt{(1 - a)}e^{-\mu a}\sqrt{\dfrac{\mu}{((\mu - 1)e^{-\mu t} + 1)}}.$

Example 3. In this test experiment non-stiff mortality rate with different data is taken as

$\mathsf{m}(a) = 10e^{-100(1-a)},\ \xi(a, y, t) = 0,\ \eta(a, y, t) = 20a(1 - a),$

with corresponding weights as $\gamma_s = 1, s = \xi, \eta$

and initial condition $\rho(a, 0) = Ce^{(-\frac{e^{(-100(1-a))}}{10} - \mu a)}, \tau = 0.5, \mu = 2.78, C = 2.96.$

The modeling Eq. (6.4) has the following solution $\rho(a, t) = Ce^{(-\frac{e^{(-100(1-a))}}{10} - \mu a)}e^{\mu t}.$

Example 4. Another stiff type of mortality rate is

$\mathsf{m}(a) = -\dfrac{1}{\alpha(1 - a)\ln(1 - a)},\ \xi(a, y, t) = y^2,\ \eta(a, y, t) = 4,$

and the weight function is $\gamma_s = 1, s = \xi, \eta,$

with initial condition $\rho(a, 0) = C\ln(1 - a)^{1/16}e^{-\mu a}, \alpha = 16, \tau = 0.5, \mu = 4.19, C = 2.37,$

and true solution is $\rho(a, t) = C\ln(1 - a)^{1/16}e^{-\mu a}\sqrt{\dfrac{\mu}{((\mu - 1)e^{-\mu t} + 1)}}.$

The numerical results of Examples 1-4 are shown in Figs. (6.1)-(6.7), respectively. The numerical results, when compared with exact solutions available in literature, are found to be in good agreement, see in Fig. 6.1(A), Fig. 6.3(A), Fig. 6.5(A), and Fig. 6.7(A) respectively. The advantage of designed scheme is that they work efficiently for stiff as well as non-stiff terms and maintain higher order accuracy. The order of accuracy and error norms are listed in Tables (6.1)-(6.4). These tables show the effective order of accuracy of the designed scheme. From the above order of convergence, we can't ensure

that it efficiently works for the long time simulation, but it seems like a good compromise between efficiency for long time simulation and regularity constraint on the coefficient functions. Further, when the compatibility condition between initial age and the birth rate is not satisfied, a jump discontinuity may arise in the first derivative or in the density function itself. In both cases, the designed scheme works very well, because the method gives non-oscillatory results and sharp discontinuity transitions. We point out that the order of accuracy determined by the L^1 norm is 1 more than as compared to the L^∞ norm which can be seen in Fig.1B, Fig.3B, Fig.5B, and Fig.7A. The reason behind this is the cancellation of neighboring fluxes near the boundary which gives an extra order of accuracy which is no longer valid. A Pictorial representation of exact and numerical solution of problems 1-3 at different time levels in 3D can be seen in Fig.2, Fig.4 and Fig.6, respectively.

The novel work of the designed scheme is shown in the numerical results of Examples 2 and 4, because, the schemes that are already present in literature do not converge [96] for the mortality rates of the type $\mathsf{m}(a) = \frac{c}{(1-a)}, 0 < c < 1,$ and $m(a) = \frac{1}{c_1(1-a)\ln(1-a)}, 0 < c_1 \leq 1$. The designed scheme efficiently works for these type of source terms which can be seen in Figure 3 and in Figure 7.

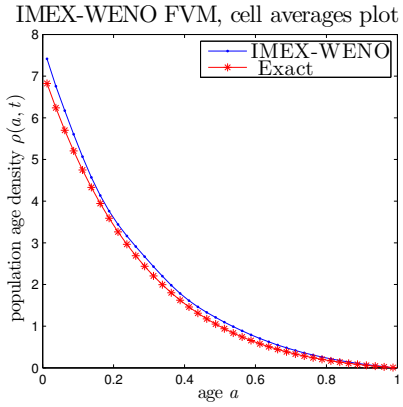

(a) The dotted line represent the numerical solution and the star line for the the exact solution at time t=0.5

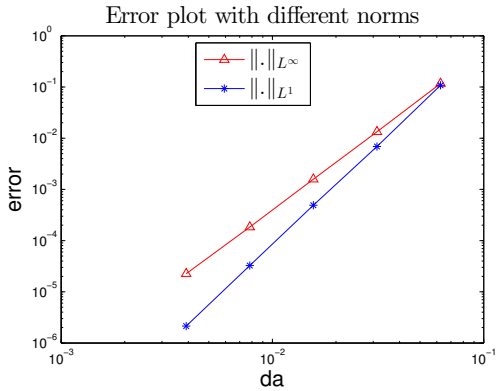

(b) A graphically representation of L^1 and L^∞ error at time t=0.5

Figure 6.1: Simulation of Example 1

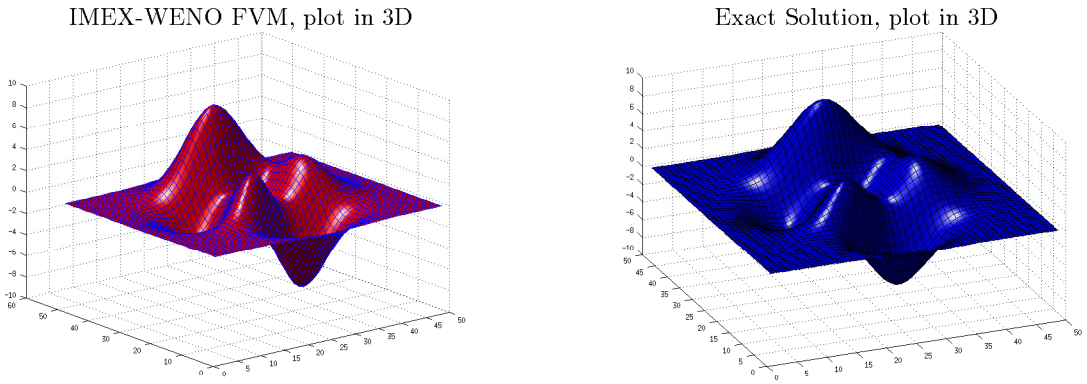

(a) Numerical Solution (b) Exact Solution

Figure 6.2: A Pictorial representation of exact and numerical solution of Example 1 at different time levels in 3D by using uniform grid cells N=40.

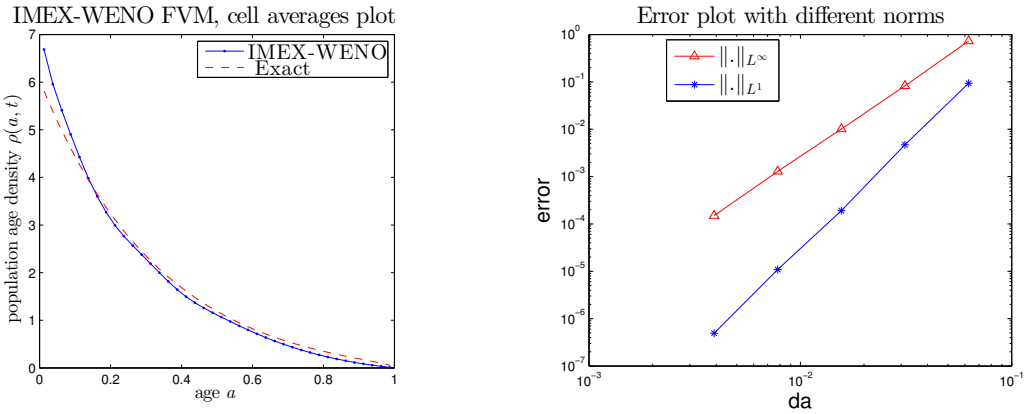

(a) dotted line depict the numerical solution and star line stand for the the exact solution at time t=0.5

(b) A graphical representation for error norms of Example 2

Figure 6.3: Simulation of Example 2

N	$\|\cdot\|_{L^1}$	r	$\|\cdot\|_{L^\infty}$	r
16	1.08e-1		1.17e-1	
32	6.89e-3	3.93	1.33e-2	3.13
64	4.91e-4	3.81	1.58e-3	3.07
128	3.26e-5	3.91	1.84e-4	3.10
256	2.14e-6	3.93	2.26e-5	3.02

Table 6.1: Comparison between L^1 and L^∞ errors for Example 1.

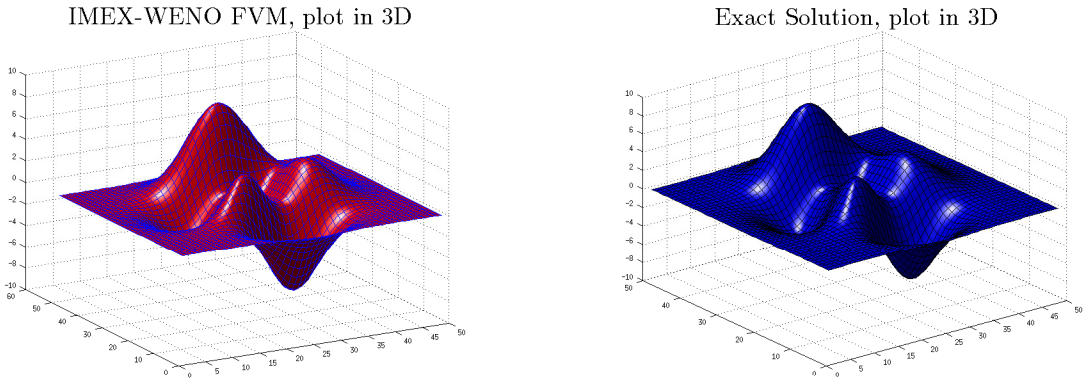

(a) Numerical Solution (b) Exact Solution

Figure 6.4: A graphical representation of exact and numerical solution of Example 2 in 3D at different time level with uniform grid cells N=40.

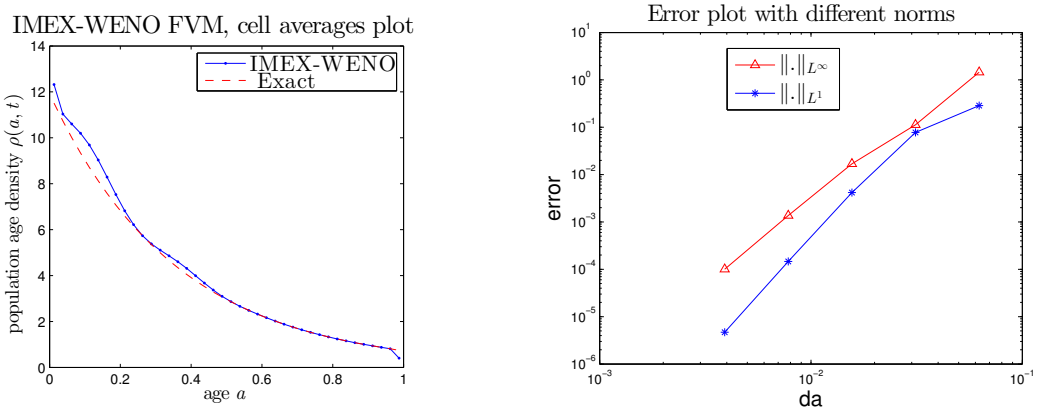

(a) dotted line represent the numerical solution and the star line for the the exact solution at time t=0.5

(b) A graphical representation of L^1 and L^∞ error of Example 3.

Figure 6.5: Simulation of Example 3.

N	$\|\cdot\|_{L^1}$	r	$\|\cdot\|_{L^\infty}$	r
16	9.33e-2		7.29e-1	
32	4.70e-3	4.31	8.27e-2	3.13
64	1.91e-4	4.62	1.01e-2	3.00
128	1.09e-5	4.12	1.29e-3	2.96
256	4.92e-7	4.47	1.50e-4	3.10

Table 6.2: Comparison between L^1 and L^∞ errors for Example 2.

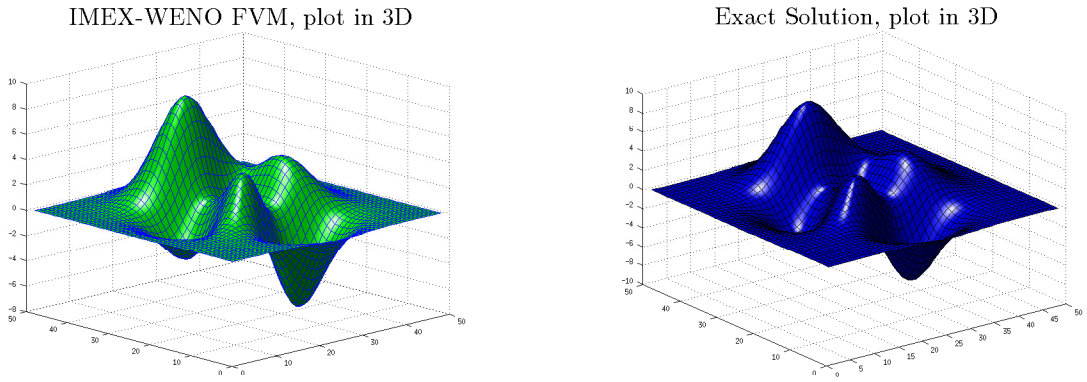

(a) Numerical Solution (b) True Solution

Figure 6.6: An illustration of approximate solutions and exact solution of Example 3 in 3D uniform grid cells N=40.

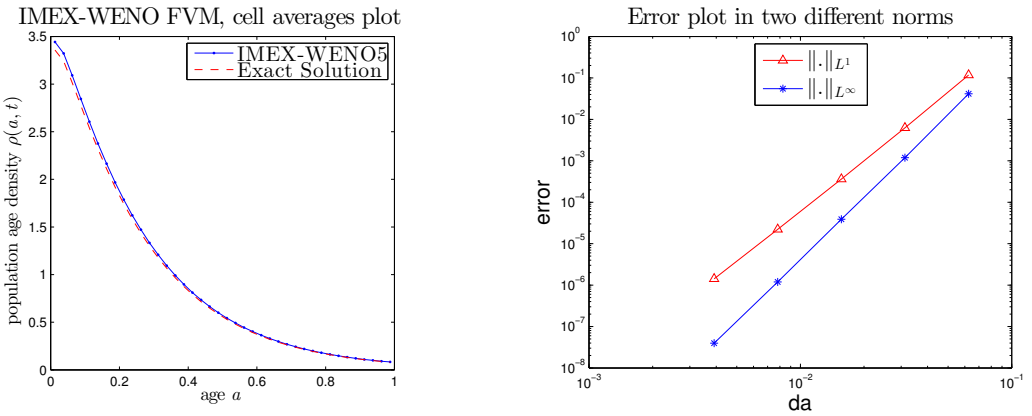

(a) Numerical solution is plotted by dotted line while one line depict the exact solution

(b) A graphical representation of L^1 and L^∞ errors of Example 4

Figure 6.7: Simulation of Example 4.

N	$\|\cdot\|_{L^1}$	r	$\|\cdot\|_{L^\infty}$	r
16	2.86e-1		1.54e-0	
32	7.83e-2	5.20	1.12e-1	3.69
64	4.17e-3	4.22	1.69e-2	3.73
128	1.46e-4	4.83	1.37e-3	3.63
256	4.68e-5	4.97	1.00e-4	3.77

Table 6.3: Comparison error table for Example 3

N	$\|\cdot\|_{L^1}$	r	$\|\cdot\|_{L^\infty}$	r
16	4.13e-2		1.17e-1	
32	1.19e-3	5.12	6.23e-3	4.23
64	3.89e-5	4.93	3061e-4	4.11
128	1.19e-6	5.03	2.21e-5	4.03
256	3.97e-8	4.91	1.42e-6	3.96

Table 6.4: Error table for Example 4

5 Summary

In this chapter, a new population age density model has been derived, which is based on the classical model [84]. This model includes nonlinear population growth, death rate and birth rate, which contains the global terms in the coefficients and in the boundary condition. The presence of global terms and stiff type of mortality rate leads complication in the approximate solution of the problem. The design of the higher order accurate scheme is based on a method of lines in which the spatial discretization is done through WENO5 reconstruction procedure. Moreover, to maintain the high order accuracy in the global boundary condition and non-local term, the fifth order composite rule in a specific manner has been used. Semi-discretization of the problem leads to a system of first order initial value problems. For total discretization, the particular type of scheme has been used in which implicit discretization is utilized for natural mortality rate (stiff) and explicit discretization is employed for non-stiff terms. Numerical examples are presented to verify the performance of the design scheme. The numerical solution is compared with the exact solution. We observe that the designed scheme gives high order accuracy which indicates that it is useful for long term simulation.

Chapter 7

Conclusions and Future Scope

This chapter summarizes the thesis findings and conclusions. The chapter also provides recommendations and suggestions about future work.

1 Conclusions

The aim of this study is to design, analyze, and implement finite volume schemes for partial differential equations originating from neuroscience and population dynamics. This thesis naturally falls in the category of applied and computational mathematics. The thesis finds the numerical solutions of problems in the form of partial differential equations. This area of research become fascinating field in the present time and remained relatively unexplored until the discovery of high speed computers. We have studied biological models in the form of hyperbolic conservation law and designed suitable numerical schemes, discussed the stability and convergence, and simulated, it on a computer to obtain the required results in practice. The work has been published in the research articles [116–118]. The objectives set out for this research work are completed in chapters. The brief summary of each chapter is as follows.

1. The first chapter is devoted to the review and analysis of existing literature that has been carried out to identify the gaps existing in the area of computational neuroscience and population dynamics. The resulting equations are hyperbolic conservation laws, thus the overview of numerical schemes for the solution of conservation laws are comprised in this chapter. Some preliminaries of neurons and their structures are also discussed.

2. To address the issue of synaptic input current and neuronal behavior beyond the threshold level, a parameter and boundary conditions are included in the Stein's model and discussed in Chapter 2. Due to the existence of delay as well as advance arguments and variable coefficients in the governing equation, the analytical solution is not possible. Therefore, high-order numerical scheme is introduced in this chapter. The performance of proposed scheme over existing schemes have been

shown in the chapter.

3. The Stein's model is based on leaky-integrate-and-fire neuron that has been carried out for different applications by many researchers. In Chapter 3, a quadratic-integrate-and-fire neuron has been introduced in the Stein's model to discuss the neuronal behaviour in more realistic manner. A suitable numerical approach has been used to find the approximate solution of governing equation which is also suitable for the discontinuous initial data. Relevant numerical examples were provided to validate the theoretical results.

4. The probability density approach in computational neuroscience has already a long history and it is used in various contexts. However, this approach is not suitable for the simulation of large neural network. In Chapter 4, we used population density approach based on probability density function for the derivation of excitatory and inhibitory population density model with jumps. The jumps represent the feedback of postsynaptic neurons which originate from the receiving of incoming currents. An appropriate and high-order finite volume scheme has been designed for the simulation of model equation and discussed in Chapter 4. The comparative results shows that the proposed scheme is better than the existence schemes for the resulting model equation.

5. The Age-Structured models play a vital role in population dynamics. Thus age-structured model has been studied in Chapters 5 & 6. Age structured model is a non-linear hyperbolic conservation law which contains non-local terms. A new type of finite volume approximation has been constructed to find the approximate solution of model equation. Moreover, this scheme is also suitable for long time behaviour of governing model equation.

2 Scope of Future Work

Research is a continuous process. The work presented in this thesis is related to the numerical study of biological models. The aim is to understand the realistic biological phenomena in terms of nonlinear mathematical models, which are very difficult to solve them analytically. Hence, we need the numerical methods to find the approximate solutions. Further research directions in this area are listed below:

1. Neurons are always noisy, even they cannot respond in the same way under repeated input signal processes. It is very difficult to apply the correct analytical approach

for the expression of this variability. Therefore, suitable numerical methods are required to study the neuronal variability.

2. Some models of noisy leaky-integrate-and-fire are highly nonlinear and resulting partial differential equations are difficult to study. We anticipate that the experience in dealing with conservation laws from neuroscience and population dynamics would be helpful to deal these complex phenomena.

3. A neuron network model with adaptation and fatigue can be studied. Due to the high nonlinearities, it would be a challenge to provide the numerical study of the impact of the fragmentation term which appears due to synchronization of neurons in the neural network.

4. The stochastic features of neuron deals through noisy leaky-integrate-and-fire-model as well as escape rate model. The difference between classical and stochastic approach is to tackle the noise term. Due to the variability, the exact solution of these model equations are not available.

3 Recommendations about Future Work

It would be interesting to consider nonlinear models from related area. A further study would be to investigate conservation laws arising in material science and related areas. Further, applications of finite volume techniques can be explored for these problems. Possible extension of theses models for higher space dimensions can be considered. Further, applications of the discontinuous Galerkin methods could be explored to study the nonlinear age-structured and neuronal models.

References

[1] K. Pakdaman, B. Perthame, and D. Salort. Dynamics of a structured neuron population. *Nonlinearity*, **23**(1):55, 2009.

[2] B. Perthame. *Transport Equations in Biology*. Frontiers in Mathematics. Birkhäuser Verlag, Basel, 2007.

[3] Wikipedia. Neuron — Wikipedia, the free encyclopedia. `http://en.wikipedia.org/w/index.php?title=Neuron&oldid=778367135`, 2017. [Online; accessed 05-May-2017].

[4] L. F. Abbott. Lapicque's introduction of the integrate-and-fire model neuron (1907). *Brain Research Bulletin*, **50**(5-6):303–304, 1999.

[5] A. L. Hodgkin and A. F. Huxley. A quantitative description of membrane current and its application to conduction and excitation in nerve. *The Journal of Physiology*, **117**(4):500–544, 1952.

[6] E. R. Kandel, J. H. Schwartz, and T. M. Jessell. *Principles of Neural Science*. McGraw-Hill, New York, fourth edition, 2000.

[7] S. R. y Cajal. The structure and connexions of neurons (Lecture delievered December 12, 1996). In:(eds) Nobel Lectures, Physiology or Medicine 1901-1921. Elsevier Publishing Company, Amsterdam-London-New York, 1967.

[8] S. R. y Cajal. A new concept of the histology of the central nervous system. In: Rottenberg, Hochberg, editors, Neurological Classics in Modern Translation. New York: Hafner, 1977.

[9] W. Gerstner and W. M. Kistler. *Spiking Neuron Models: Single Neurons, Populations, Plasticity*. Cambridge University Press, Cambridge, 2002.

[10] E. M. Izhikevich. *Dynamical Systems in Neuroscience: The Geometry of Excitability and Bursting*. MIT Press, Cambridge, Massachusetts, 2007.

[11] G. B. Ermentrout and D. H. Terman. *Mathematical Foundations of Neuroscience*, volume **35**. Springer Science & Business Media, Berlin; Heidelberg; New York, 2010.

[12] R. Q. Quiroga and S. Panzeri. *Principles of Neural Coding*. CRC Press, London, 2013.

[13] W. Gerstner, W. M. Kistler, R. Naud, and L. Paninski. *Neuronal Dynamics: From Single Neurons to Networks and Models of Cognition*. Cambridge University Press, Cambridge, 2014.

[14] L. Lapicque. Recherches quantitatives sur l'excitation électrique des nerfs traitée comme une polarization. *Journal de Physiologie et de Pathologie Générale*, **9**:620–635, 1907.

[15] A. V. Hill. Excitation and accommodation in nerve. *Proceedings of the Royal Society of London B: Biological Sciences*, **119**(814):305–355, 1936.

[16] G. Gerstein and B. Mandelbrot. Random walk models for the spike activity of a single neuron. *Biophysical Journal*, **4**(1):41–68, 1964.

[17] R. B. Stein. A theoretical analysis of neuronal variability. *Biophysical Journal*, **5**(2):173–194, 1965.

[18] R. B. Stein. Some models of neuronal variability. *Biophysical Journal*, **7**(1):37–68, 1967.

[19] B. W. Knight. Dynamics of encoding in a population of neurons. *The Journal of General Physiology*, **59**(6):734–766, 1972.

[20] V. I. Kryukov. Wald's identity and random walk models for neuron firing. *Advances in Applied Probability*, **8**(2):257–277, 1976.

[21] H. C. Tuckwell. On stochastic models of the activity of single neurons. *Journal of Theoretical Biology*, **65**(4):783–785, 1977.

[22] W. J. Wilbur and J. Rinzel. An analysis of Stein's model for stochastic neuronal excitation. *Biological Cybernetics*, **45**(2):107–114, 1982.

[23] P. Lánskỳ. On approximations of Stein's neuronal model. *Journal of Theoretical Biology*, **107**(4):631–647, 1984.

[24] H. C. Tuckwell. Neuronal interspike time histograms for a random input model. *Biophysical Journal*, **21**(3):289, 1978.

[25] D. K. Cope and H. C. Tuckwell. Firing rates of neurons with random excitation and inhibition. *Journal of Theoretical Biology*, **80**(1):1–14, 1979.

[26] H. C. Tuckwell and D. K. Cope. Accuracy of neuronal interspike times calculated from a diffusion approximation. *Journal of Theoretical Biology*, **83**(3):377–387, 1980.

[27] H. C. Tuckwell. Synaptic transmission in a model for stochastic neural acttivity. *Journal of Theoretical Biology*, **77**:65–81, 1979.

[28] W. J. Wilbur and J. Rinzel. A theoretical basis for large coefficient of variation and bimodality in neuronal interspike interval distributions. *Journal of Theoretical Biology*, **105**(2):345–368, 1983.

[29] F. B. Hanson and H. C. Tuckwell. Diffusion approximations for neuronal activity including synaptic reversal potentials. *Journal of Theoretical Neurobiology*, **2**:127–153, 1983.

[30] M. Musila and P. Lánskỳ. On the interspike intervals calculated from diffusion

approximations of Stein's neuronal model with reversal potentials. *Journal of Theoretical Biology*, **171**(2):225–232, 1994.

[31] W. Gerstner. Time structure of the activity in neural network models. *Physical Review E*, **51**(1):738, 1995.

[32] W. Gerstner. A framework for spiking neuron models: The spike response model. *Handbook of Biological Physics*, **4**:469–516, 2001.

[33] S. Fusi and M. Mattia. Collective behavior of networks with linear (VLSI) integrate-and-fire neurons. *Neural Computation*, **11**(3):633–652, 1998.

[34] G. B. Ermentrout and N. Kopell. Parabolic bursting in an excitable system coupled with a slow oscillation. *SIAM Journal on Applied Mathematics*, **46**(2):233–253, 1986.

[35] E. M. Izhikevich. Class 1 neural excitability, conventional synapses, weakly connected networks, and mathematical foundations of pulse-coupled models. *IEEE Transactions on Neural Networks*, **10**(3):499–507, 1999.

[36] G. B. Ermentrout. Type I membranes, phase resetting curves, and synchrony. *Neural Computation*, **8**(5):979–1001, 1996.

[37] B. S. Gutkin and G. B. Ermentrout. Dynamics of membrane excitability determine interspike interval variability: a link between spike generation mechanisms and cortical spike train statistics. *Neural Computation*, **10**(5):1047–1065, 1998.

[38] P. E. Latham, B. J. Richmond, P. G. Nelson, and S. Nirenberg. Intrinsic dynamics in neuronal networks. I. theory. *Journal of Neurophysiology*, **83**(2):808–827, 2000.

[39] N. Brunel and P. E. Latham. Firing rate of the noisy quadratic integrate-and-fire neuron. *Neural Computation*, **15**(10):2281–2306, 2003.

[40] B. Lindner, A. Longtin, and A. Bulsara. Analytic expressions for rate and CV of a type I neuron driven by white gaussian noise. *Neural Computation*, **15**(8):1761–1788, 2003.

[41] N. Fourcaud-Trocmé, D. Hansel, C. v. Vreeswijk, and N. Brunel. How spike generation mechanisms determine the neuronal response to fluctuating inputs. *Journal of Neuroscience*, **23**(37):11628–11640, 2003.

[42] N. Fourcaud-Trocmé and N. Brunel. Dynamics of the instantaneous firing rate in response to changes in input statistics. *Journal of Computational Neuroscience*, **18**(3):311–321, 2005.

[43] R. Brette and W. Gerstner. Adaptive exponential integrate-and-fire model as an effective description of neuronal activity. *Journal of Neurophysiology*, **94**(5):3637–3642, 2005.

[44] G. C. Quarton, T. Melnechuk, and F. O. Schmitt. *The Neurosciences. A Study Program.* Rockefeller University Press, New York, 1967.

[45] L. J. DeFelice. *Introduction to Membrane Noise*. Plenum, New York, 1981.

[46] A. V. Holden. Models of the stochastic activities of neurons, lecture notes in Biomathematics, vol. 12, 1976.

[47] L. F. Abbott and C. v. Vreeswijk. Asynchronous states in networks of pulse-coupled oscillators. *Physical Review E*, **48**(2):1483–1490, 1993.

[48] N. Brunel and V. Hakim. Fast global oscillations in networks of integrate-and-fire neurons with low firing rates. *Neural Computation*, **11**(7):1621–1671, 1999.

[49] N. Brunel. Dynamics of sparsely connected networks of excitatory and inhibitory spiking neurons. *Journal of Computational Neuroscience*, **8**(3):183–208, 2000.

[50] A. Renart, N. Brunel, and X. Wang. Mean-field theory of irregularly spiking neuronal populations and working memory in recurrent cortical networks. *Computational Neuroscience: A comprehensive Approach*, pages 431–490, 2004.

[51] A. Faisal, L. Selen, and L. Wolpert. Noise in the nervous system. *Nature Reviews Neuroscience*, **9**(4):292–303, 2008.

[52] A. Faisal, L. Selen, and L. Wolpert. Neuronal noise. *Scholarpedia*, **8**(9):1618, 2013.

[53] A. N. Burkitt. A review of the integrate-and-fire neuron model: I. homogeneous synaptic input. *Biological Cybernetics*, **95**(1):1–19, 2006.

[54] J. Arcede. Fundamental theorem of calculus for backwards Itô integral. *Matimyas Matematika, Proceedings of the 9th Philippines-Taiwan Symposium on Analysis*, **34**(01):1–9, 2011.

[55] J. Arcede. On integration-by-parts and Itô formula for backwards Itô integral. *The Mindanawan Journal of Mathematics*, **3**(02):112–131, 2012.

[56] D. Q. Nykamp and D. Tranchina. A population density approach that facilitates large-scale modeling of neural networks: Analysis and an application to orientation tuning. *Journal of Computational Neuroscience*, **8**(1):19–50, 2000.

[57] D. Q. Nykamp and D. Tranchina. A population density approach that facilitates large-scale modeling of neural networks: extension to slow inhibitory synapses. *Neural Computation*, 13(3):511–546, 2001.

[58] F. Apfaltrer, C. Ly, and D. Tranchina. Population density methods for stochastic neurons with realistic synaptic kinetics: firing rate dynamics and fast computational methods. *Network: Computation in Neural Systems*, **17**(4):373–418, 2006.

[59] C. Ly and D. Tranchina. Critical analysis of dimension reduction by a moment closure method in a population density approach to neural network modeling. *Neural Computation*, **19**(8):2032–2092, 2007.

[60] G. Dumont and J. Henry. Population density models of integrate-and-fire neurons with jumps: well-posedness. *Journal of Mathematical Biology*, **67**(3):453–481, 2012.

[61] C. Ly. A principled dimension-reduction method for the population density ap-

proach to modeling networks of neurons with synaptic dynamics. *Neural Computation*, **25**(10):2682–2708, 2013.

[62] G. Dumont and J. Henry. A density model for a population of theta neurons. *The Journal of Mathematical Neuroscience*, **4**(1):1–22, 2014.

[63] W. Nicola, C. Ly, and S. A. Campbell. One-dimensional population density approaches to recurrently coupled networks of neurons with noise. *SIAM Journal on Applied Mathematics*, **75**(5):2333–2360, 2015.

[64] J. Touboul. Bifurcation analysis of a general class of nonlinear integrate-and-fire neurons. *SIAM Journal on Applied Mathematics*, **68**(4):1045–1079, 2008.

[65] J. Touboul and R. Brette. Spiking dynamics of bidimensional integrate-and-fire neurons. *SIAM Journal on Applied Dynamical Systems*, **8**(4):1462–1506, 2009.

[66] K. A. Newhall, G. Kovačič, P. R. Kramer, and D. Cai. Cascade-induced synchrony in stochastically driven neuronal networks. *Physical Review E*, **82**(4):041903, 2010.

[67] M. J. Cáceres, , and B. Perthame. Beyond blow-up in excitatory integrate and fire neuronal networks: refractory period and spontaneous activity. *Journal of Theoretical Biology*, **350**:81–89, 2014.

[68] Y. Kuramoto. A collective synchronization of pulse-coupled oscillators and excitable units. *Physica D: Nonlinear Phenomena*, **50**(1):15–30, 1991.

[69] Y. Kuramoto. A simple and stable numerical solution for the population density equation. *Neural Computation*, 15(9):2129–2146, 2003.

[70] B. W. Knight, D. Manin, and L. Sirovich. Dynamical models of interacting neuron populations in visual cortex. *Proc IEEE Symposium on Robotics and Cybernetics Lille-France*, **54**:4–8, 1996.

[71] A. Omurtag, B. W. Knight, and L. Sirovich. On the simulation of large populations of neurons. *Journal of Computational Neuroscience*, **8**(1):51–63, 2000.

[72] A. Omurtag, B. W. Knight, and L. Sirovich. Dynamics of neuronal populations: the equilibrium solution. *SIAM Journal on Applied Mathematics*, **60**(6):2009–2028, 2000.

[73] B. W. Knight. Dynamics of encoding in neuron populations: some general mathematical features. *Neural Computation*, **12**(3):473–518, 2000.

[74] A. Ashyralyev, M. E. Koksal, and R. P. Agarwal. A difference scheme for Cauchy problem for the hyperbolic equation with self-adjoint operator. *Mathematical and Computer Modelling*, **52**(1):409–424, 2010.

[75] A. Ashyralyev, M. E. Koksal, and R. P. Agarwal. An operator-difference scheme for abstract Cauchy problems. *Computers and Mathematics with Applications*, **61**(1):1855–1872, 2011.

[76] F. G. Awad, P. Sibandaa, and S. S. Motsa. On the linear stability analysis of a

maxwell fluid with double-diffusive convection. *Applied Mathematical Modelling*, **34**(11):3509–3517, 2010.

[77] S. S. Motsa, P. Sibanda, and S.Shateyi. A new spectral-homotopy analysis method for solving a nonlinear second order BVP. *Communications in Nonlinear Science and Numerical Simulation*, **15**(09):2293–2302, 2010.

[78] F. Sharpe and A. J. Lotka. A problem in age-distribution. *Philosophical Magazine*, **6**:435–438, 1911.

[79] A. G. McKendrick. Applications of mathematics to medical problems. *Proceedings of the Edinburgh Mathematical Society*, **44**:98–130, 1926.

[80] A. J. Lotka. The stability of the normal age-distribution. *Proceedings of the National Academy of Science USA*, **8**:339–345, 1922.

[81] A. J. Lotka. On an integral equation in population analysis. *The Annals of Mathematical Statistics*, **10**:435–438, 1939.

[82] W. Feller. On the integral equation of renewal theory. *The Annals of Mathematical Statistics*, **12**:243–267, 1941.

[83] R. Bellman and K. Cooke. *Differential Difference Equations*. CA: RAND Corporation, Santa Monica, 1963.

[84] M. E. Gurtin and R. C. MacCamy. Non-linear age-dependent population dynamics. *Archive for Rational Mechanics and Analysis*, **54**(3):281–300, 1974.

[85] M. Iannelli. Mathematical theory of age-structured population dynamics. *Applied Mathematics Monographs, Vol. 7, comitato nazionale per le scienze matematiche, Consiglio Nazionale delleRicerche(C.N.R),Giardini,Pisa*, 1995.

[86] M. K. Kadalbajoo and R. K. Bawa. Variable-mesh difference scheme for singularly-perturbed boundary-value problems using splines. *Journal of Optimization Theory and Applications*, **90**(2):405–416, 1996.

[87] M. K. Kadalbajoo and R. K. Bawa. Third-order variable-mesh cubic spline methods for singularly-perturbed boundary-value problems. *Applied Mathematics and Computation*, **59**(2-3):117–129, 1993.

[88] S. C. S. Rao and S. Kumar. Robust high order convergence of an overlapping Schwarz method for singularly perturbed semilinear reaction-diffusion problems. *Journal of Computational Mathematics*, **31**(1):509–521, 2013.

[89] S. C. S. Rao and M. Kumar. Exponential B-spline collocation method for self-adjoint singularly perturbed boundary value problems. *Applied Numerical Mathematics*, **58**(1):1572–1581, 2008.

[90] L. M. Abia, O. Angulo, and J. C. López-Marcos. Age-structured population dynamics models and their numerical solutions. *Ecological Modelling*, **188**(1):112–136, 2005.

[91] L. M. Abia, O. Angulo, and J. C. López-Marcos. Numerical schemes for a size-structured cell population model with equal fission. *Mathematical and Computer Modelling*, **50**(5):653–664, 2009.

[92] V. Kanwar. A family of third-order multipoint methods for solving nonlinear equations. *Applied Mathematics and Computation*, **176**(2):409–413, 2006.

[93] M.-Y. Kim and T. Selenge. Discontinuous-continuous Galerkin methods for population diffusion with finite life span. *Mathematical Population Studies*, **23**(1):17–36, 2016.

[94] R. Higinio, G. Singh, V. Kanwar, and S. Bhatia. An efficient variable step-size rational Falkner-type method for solving the special second-order IVP. *Applied Mathematics and Computation*, **291**(1):39–51, 2016.

[95] G. F. Webb. *Theory of Nonlinear Age-Dependent Population*. Marcel Dekker, Inc., New York, 1985.

[96] M. Y. Kim and Y. Kwon. A collocation method for the Gurtin-macCamy equation with finite life-span. *SIAM Journal on Numerical Analysis*, **39**(6):1914–1937, 2002.

[97] S. A. Yousefi, M. Behroozifar, and M. Dehghan. Numerical solution of the nonlinear age-structured population models by using the operational matrices of Bernstein polynomials. *Applied Mathematical Modelling*, **36**(1):945–963, 2012.

[98] M. Iannelli and F. Milner. On the approximation of the Lotka–Mckendrick equation with finite life-span. *Journal of Computational and Applied Mathematics*, **136**(1):245–254, 2001.

[99] B. Perthame and P. Laurencot. Exponential decay for the growth-fragmentation/cell-division equations. *Communications in Mathematical Sciences.*, **7(2)**:503–510, 2009.

[100] J. C. Strikwerda. *Finite Difference Schemes and Partial Differential Equations*. SIAM, Philadelphia, second edition, 2004.

[101] K. W. Morton and D. F. Mayers. *Numerical Solution of Partial Differential Equations*. Cambridge University Press, Cambridge, second edition, 2005.

[102] G. D. Smith. *Numerical Solution of Partial Differential Equations (Finite Difference Methods)*. Oxford University Press, Oxford, third edition, 1985.

[103] D. Gottlieb and S. A. Orszag. *Numerical Analysis of Spectral Methods: Theory and Applications*. SIAM, Philadelphia, PA, 1977.

[104] C. Canuto, M. Y. Hussaini, A. Quarteroni, and T.A. Zang. *Spectral Methods in Fluid Dynamics*. Springer-Verlag, Berlin, 1998.

[105] B. Fornberg. *A Practical Guide to Pseudospectral Methods*. Cambridge University Press, Cambridge UK, 1996.

[106] L. N. Trefethen. *Spectral Methods in MATLAB*. SIAM, Philadelphia, PA, 2000.

[107] J. Shen and T. Tang. *Spectral and High-Order Methods with Applications*. Science Press, Beijing, 2007.

[108] J. S. Hesthaven, S. Gottlieb, and D. Gottlieb. *Spectral Methods for Time-Dependent Problems*. Cambridge University Press, Cambridge, 2007.

[109] J. E. Akin. *Application and Implementation of Finite Element Methods*. Academic Press, London, 1982.

[110] P. G. Ciarlet. *The Finite Element Method for Elliptic Problems*. North-Holland, Amsterdam, 1978.

[111] J. N. Reddy. *An Introduction to the Finite Element Method*. McGraw-Hill, Boston, 1993.

[112] G. Chen and J. Zhou. *Boundary Element Methods*. Academic Press, New York, 1992.

[113] D. Colton and R. Kress. *Integral Equation Methods in Scattering Theory*. John Wiley and Sons, New York, 1983.

[114] E. Godlewski and P.-A. Raviart. *Numerical Approximation of Hyperbolic Systems of Conservation Laws*. Springer-Verlag, New York, 1996.

[115] O. Oleinik. Discontinuous solutions of nonlinear differential equations. *American Mathematical Society Translations: Series 2*, **26**:95–172, 1963.

[116] S. Kumar and P. Singh. Higher-order MUSCL scheme for transport equation originating in a neuronal model. *Computers & Mathematics with Applications*, **70**(12):2838–2853, 2015.

[117] S. Kumar and P. Singh. Finite volume approximations for size structured neuron model. *Differential Equations and Dynamical Systems*, **25**(2):251–265, 2017.

[118] S. Kumar and P. Singh. High-order IMEX-WENO finite volume approximation for nonlinear age-structured population model. *International Journal of Computer Mathematics*, **95**(1):82–97, 2018.

[119] H. C. Tuckwell. *Introduction to Theoretical Neurobiology*. Cambridge University Press, Cambridge, 1988.

[120] M. K. Kadalbajoo and K. K. Sharma. Numerical treatment of a mathematical model arising from a model of neuronal variability. *Journal of Mathematical Analysis and Applications*, **307**(2):606–627, 2005.

[121] K. K. Sharma and Paramjeet Singh. Hyperbolic partial differential-difference equation in the mathematical modeling of neuronal firing and its numerical solution. *Applied Mathematics Computation.*, **201**(1-2):229–238, 2008.

[122] Q. Wang and Z. Zhang. High-order upwind finite volume element schemes for modelling of neuronal firing. *International Journal of Computer Mathematics*, **91**(3):625–640, 2014.

[123] B. Perthame, P. Markowich, and J. P. Zubelli. Mathematical methods and modeling of biophysical phenomena. *Mathematical and Computer Modelling*, **47**(7-8):663–665, 2008.

[124] R. J. LeVeque. A study of numerical methods for hyperbolic conservation laws with stiff source terms. *Journal of Computational Physics*, **86**:187–210, 1990.

[125] R. J. LeVeque. *Numerical Methods for Conservation Laws, Lectures in Mathematics, ETH Zürich*. Birkhäuser, Basel, 1999.

[126] R. J. LeVeque. *Finite Volume Methods for Hyperbolic Problems*. Cambridge University Press, Cambridge, 2002.

[127] A. Chalabi. Stable upwind schemes for hyperbolic conservation laws with source terms. *IMA Journal of Numerical Analysis*, **12**:217–241, 1992.

[128] H. J. Schroll and R. Winther. Finite difference schemes for conservation laws with source terms. *IMA Journal of Numerical Analysis*, **16**:201–215, 1996.

[129] S. N. Kruzkov. First order quasi-linear equations in several independent variables. *USSR Math. Sbornik*, **10**(2):217–243, 1970.

[130] R. J. LeVeque and J. Oliger. Numerical methods based on additive splittings for hyperbolic partial differential equations. *Mathematics of Computation*, **40**:467–497, 1983.

[131] J. B. Perot. An analysis of the fractional step method. *Journal of Computational Physics*, **108**:51–58, 1993.

[132] L. A. Monthe. A study of splitting scheme for hyperbolic conservation laws with source terms. *Journal of Computational and Applied Mathematics*, **137**:1–12, 2001.

[133] E. Tadmor. Numerical viscosity and the entropy condition for the conservative difference schemes. *Mathematics of Computation*, **43**:369–382, 1984.

[134] Z. Li. *The immersed interface method-a numerical approach for partial differential equations with interfaces, Ph.D. thesis*. University of Washington, 1994.

[135] P. Singh and K. K. Sharma. Numerical approximations to the transport equation arising in neuronal variability. *International Journal of Pure and Applied Mathematics*, **69**(3):341–356, 2011.

[136] H. R. Wilson. *Spikes, Decisions, and Actions: The Dynamical Foundations of Neuroscience*. Oxford University Press, New York, 1999.

[137] C. Christodoulou and G. Bugmann. Near poisson-type firing produced by concurrent excitation and inhibition. *BioSystems*, **58**(1-3):41–48, 2000.

[138] P. Dayan and L. F. Abbott. *Theoretical Neuroscience: Computational and Mathematical Modeling of Neural Systems*. MIT Press, Cambridge, Massachusetts, 2001.

[139] A. Kuhn, A. Aertsen, and S. Rotter. Neuronal integration of synaptic input in the fluctuation-driven regime. *Journal of Neuroscience*, **24**(10):2345–2356, 2004.

[140] M. W. Levine and Michael W. The distribution of the intervals between neural impulses in the maintained discharges of retinal ganglion cells. *Biological Cybernetics*, **65**(6):459–467, 1991.

[141] P. Tiesinga, J. V. José, and T. J. Sejnowski. Comparison of current-driven and conductance-driven neocortical model neurons with Hodgkin-Huxley voltage-gated channels. *Physical Review E*, **62**(6):8413, 2000.

[142] S. K. Bhowmik. Error estimates for discontinuous Galerkin finite element methods for a neuron network model. *Applicable Analysis*, **94**(10):2011–2022, 2015.

[143] R. Eftimie, G. D. Vries, and M. A. Lewis. Weakly nonlinear analysis of a hyperbolic model for animal group formation. *Journal of Mathematical Biology*, **59**(1):37–74, 2009.

[144] M. J. Richardson. Firing-rate response of linear and nonlinear integrate-and-fire neurons to modulated current-based and conductance-based synaptic drive. *Physical Review E*, **76**(2):021919, 2007.

[145] R. Jolivet, T. J. Lewis, and W. Gerstner. Generalized integrate-and-fire models of neuronal activity approximate spike trains of a detailed model to a high degree of accuracy. *Journal of Neurophysiology*, **92**(2):959–976, 2004.

[146] R.C. Mittal and R. Jiwari. A higher order numerical scheme for some nonlinear differential equations: models in biology. *International Journal for Computational Methods in Engineering Science and Mechanics*, **12**:134–140, 2011.

[147] C.-W. Shu. Essentially non-oscillatory and weighted essentially non-oscillatory schemes for hyperbolic conservation laws, in advanced numerical approximation of nonlinear hyperbolic equations, B. Cockburn, C. Johnson, C.-W. Shu and E. Tadmor (Editor: A. Quarteroni), Lecture Notes in Mathematics. **1697**:325–432, 1998.

[148] Y. Xing and C.-W. Shu. High order well-balanced finite volume WENO schemes and discontinuous Galerkin methods for a class of hyperbolic systems with source terms. *Journal of Computational Physics*, **214**(2):567–598, 2006.

[149] X.-D. Liu, S. Osher, and T. Chan. Weighted essentially non-oscillatory schemes. *Journal of Computational Physics*, **115**(1):200–212, 1994.

[150] G. S. Jiang and C.-W. Shu. Efficient implementation of weighted ENO schemes. *Journal of Computational Physics*, **126**(1):202–228, 1996.

[151] C.-W. Shu and S. Osher. Efficient implementation of essentially non-oscillatory shock-capturing schemes. *Journal of Computational Physics*, **77**(2):439–471, 1988.

[152] S. Gottlieb and C.-W. Shu. Total variation diminishing Runge-Kutta schemes. *Mathematics of Computation*, **67**(221):73–85, 1998.

[153] S. Gottlieb, C.-W. Shu, and E. Tadmor. Strong stability preserving time discretiza-

tion. *SIAM Review*, **43** (1):89–112, 2001.

[154] L. Sirovich, A. Omurtag, and K. Lubliner. Dynamics of neural populations: Stability synchrony. *Network: Computation in Neural Systems*, **17**:3–29, 2006.

[155] G. Dumont and J. Henry. Synchronization of an excitatory integrate-and-fire neural network. *Bulletin of Mathematical Biology*, **75**(4):629–648, 2013.

[156] D. Cai, L. Tao, A. V. Rangan, and D. W. McLaughlin. Kinetic theory for neuronal network dynamics. *Communications in Mathematical Sciences*, **4**:97–127, 2006.

[157] M. J. Cáceres, J. A. Carrillo, and B. Perthame. Analysis of nonlinear noisy integrate & fire neuron models: blow-up and steady states. *The Journal of Mathematical Neuroscience*, **1**(1):7, 2011.

[158] J. A. Carrillo, B. Perthame, D. Salort, and D. Smets. Qualitative properties of solutions for the noisy integrate and fire model in computational neuroscience. *Nonlinearity*, **28**(9):3365–3388, 2015.

[159] F. Delarue, J. Inglis, S. Rubenthaler, and E. Tanré. Particle systems with a singular mean-field self-excitation. application to neuronal networks. *Stochastic Processes and their Applications*, **125**(6):2451–2492, 2015.

[160] M. J. Cáceres and R. Schneider. Blow-up, steady states and long time behaviour of excitatory-inhibitory nonlinear neuron models. *Kinetic and Related Models*, **10**:587–612, 2017.

[161] M. J. Cáceres and R. Schneider. Towards a realistic NNLIF model: Analysis and numerical solver for excitatory-inhibitory networks with delay and refractory periods. *arXiv:1705.02205*, 2017.

[162] L. Sirovich. Dynamics of neuronal populations: eigenfunction theory; some solvable cases. *Network: Computation in Neural Systems*, **14**:249–272, 2003.

[163] M. J. Cáceres, J. A. Carrillo, and L. Tao. A numerical solver for a nonlinear Fokker–Planck equation representation of neuronal network dynamics. *Journal of Computational Physics*, **230**(4):1084–1099, 2011.

[164] C.-H. Huang, C.-C. K. Lin, and M.-S. Ju. Finite element method for population density approach for large-scale neuronal networks. *Journal of Medical and Biological Engineering*, **33**:552–563, 2013.

[165] J. Touboul. Importance of the cutoff value in the quadratic adaptive integrate-and-fire model. *Neural Computation*, **21**(8):2114–2122, 2009.

[166] A. Renart and M. K. Machens. Variability in neural activity and behaviour. *Current Opinion in Neurobiology*, **25**:211–220, 2014.

[167] H. C. Tuckwell. *Stochastic Processes in the Neurosciences*. SIAM, Philadelphia, 1989.

[168] G. Strang. On the construction and comparison of difference schemes. *SIAM*

Journal on Numerical Analysis, **5**(3):506–517, 1968.

[169] J. A. J. Metz and O. Diekmann. *The Dynamics of Physiologically Structured Populations, Lecture Notes Biomathematics*, volume **68**. Springer, Berlin, 1986.

[170] E. D. McGrady and R. M. Ziff. Shattering transition in fragmentation. *Physics Review Letter*, **58**(9):892–895, 1987.

[171] L. Arlotti and J. Banasiak. Strictly substochastic semigroups with application to conservative and shattering solutions to fragmentation equations with mass loss. *Journal of Mathematical Analysis and Applications*, **293**(2):693–720, 2004.

[172] F. Baccelli, D. R. McDonald, and J. Reynier. A mean field model for multiple TCP connections through a buffer implementing RED. *Performance Evaluation*, **49**(1-4):77–97, 2002.

[173] B. Basse, B. C. Baguley, E. S. Marshall, W. R. Joseph, B. van Brunt, G. Wake, and D. J. N. Wall. A mathematical model for analysis of the cell cycle in cell lines derived from human tumors. *Journel of Mathematical Biology*, **47**(4):295–312, 2003.

[174] J. Bertoin and A. V. Gnedin. Asymptotic laws for nonconservative self-similar fragmentations. *Electronic Journal of Probability*, **9**(19):575–593, 2004.

[175] M. Escobedo, P. Laurencot, S. Mischler, and B. Perthame. Gelation and mass conservation in coagulation-fragmentation models. *Journal of Differential Equations*, **195**(1):143–174, 2003.

[176] S. Mischler, B. Perthame, and L. Ryzhik. Stability in a nonlinear population maturation model. *Mathematical Models and Methods in Applied Sciences*, **12**(12):1751–1772, 2002.

[177] M. Iannelli, M. Martcheva, and F. Milner. *Gender-structured Population Modeling: Mathematical Methods, Numerics, and Simulations*. SIAM, Philadelphia, 2005.

[178] A. J. Lotka. *Elements of Physical Biology*. Williams and Wilkins Company, Baltimore, 1925.

[179] S. K. Bhowmik. Numerical approximation of a convolution model of $\dot{\theta}$-neuron networks. *Applied Numerical Mathematics*, **61** (4):581–592, 2011.

[180] V. K. Baranwal, R. K. Pandey, M. P. Tripathi, and O. P. Singh. Analytic algorithms for some models of nonlinear age-structured population dynamics and epidemiology. *Journal of Modern Physics*, **2**:236–247, 2011.

[181] F. A. Milner and T. Arbogast. A finite difference for a two sex model of population dynamics. *SIAM Journal on Numerical Analysis*, **26**(6):1474–1486, 1989.

[182] M. Iannelli, M.-Y. Kim, and E.-J. Park. Splitting methods for the numerical approximation of some models of age-structured population dynamics and epidemiology. *Applied Mathematics and Computation*, **87**(1):69–93, 1997.

[183] J. Zhu, X. Zhong, C.-W. Shu, and J. Qiu. Runge-Kutta discontinuous Galerkin

method with a simple and compact Hermite WENO limiter on unstructured meshes. *Communications in Computational Physics*, **21**(3):623–649, 2017.

[184] J. Zhu, X. Zhong, C.-W. Shu, and J. Qiu. Runge-Kutta discontinuous Galerkin method with a simple and compact Hermite WENO limiter. *Communications in Computational Physics*, **19**(4):944–969, 2016.

[185] T. Cui, W. Leng, D. Lin, S. Ma, and L. Zhang. High order mass-lumping finite elements on simplexes. *Numerical Mathematics: Theory, Methods and Applications*, **10**(2):331–350, 2017.

[186] J. Shi, C. Hu, and C.-W. Shu. A technique of treating negative weights in WENO schemes. *Journal of Computational Physics*, **175**:108–127, 2002.

[187] L. Pareschi and G. Russo. Implicit-explicit Runge-Kutta methods and applications to hyperbolic systems with relaxation. *Journal of Scientific Computing*, **25**(1-2):129–155, 2005.

List of Publications

International Journal

1. Santosh Kumar, Paramjeet Singh, *"Higher-order MUSCL scheme for transport equation originating in a neuronal model"*, Computers & Mathematics With Applications, **70 (12)**, 2838-2853, 2015. SCI (Elsevier).

2. Santosh Kumar, Paramjeet Singh, *"High-order finite volume approximation for population density model based on quadratic integrate-and-fire neuron"*, under Review.

3. Santosh Kumar, Paramjeet Singh, Mehmet Emir Koksal *"High order WENO finite volume approximation for population density neuron model"*, under Review.

4. Santosh Kumar, Paramjeet Singh. *"Finite volume approximation for age size structured neuron model"*, "Differential Equations and Dynamical Systems", **25 (02)**, 251-265, 2017. Scopus (Springer).

5. Santosh Kumar, Paramjeet Singh *"High-order IMEX-WENO finite volume approximation for nonlinear age-structured population model"*, International Journal of Computer Mathematics, **95 (01)**, 82-97, 2018. SCI (Taylor & Francis).